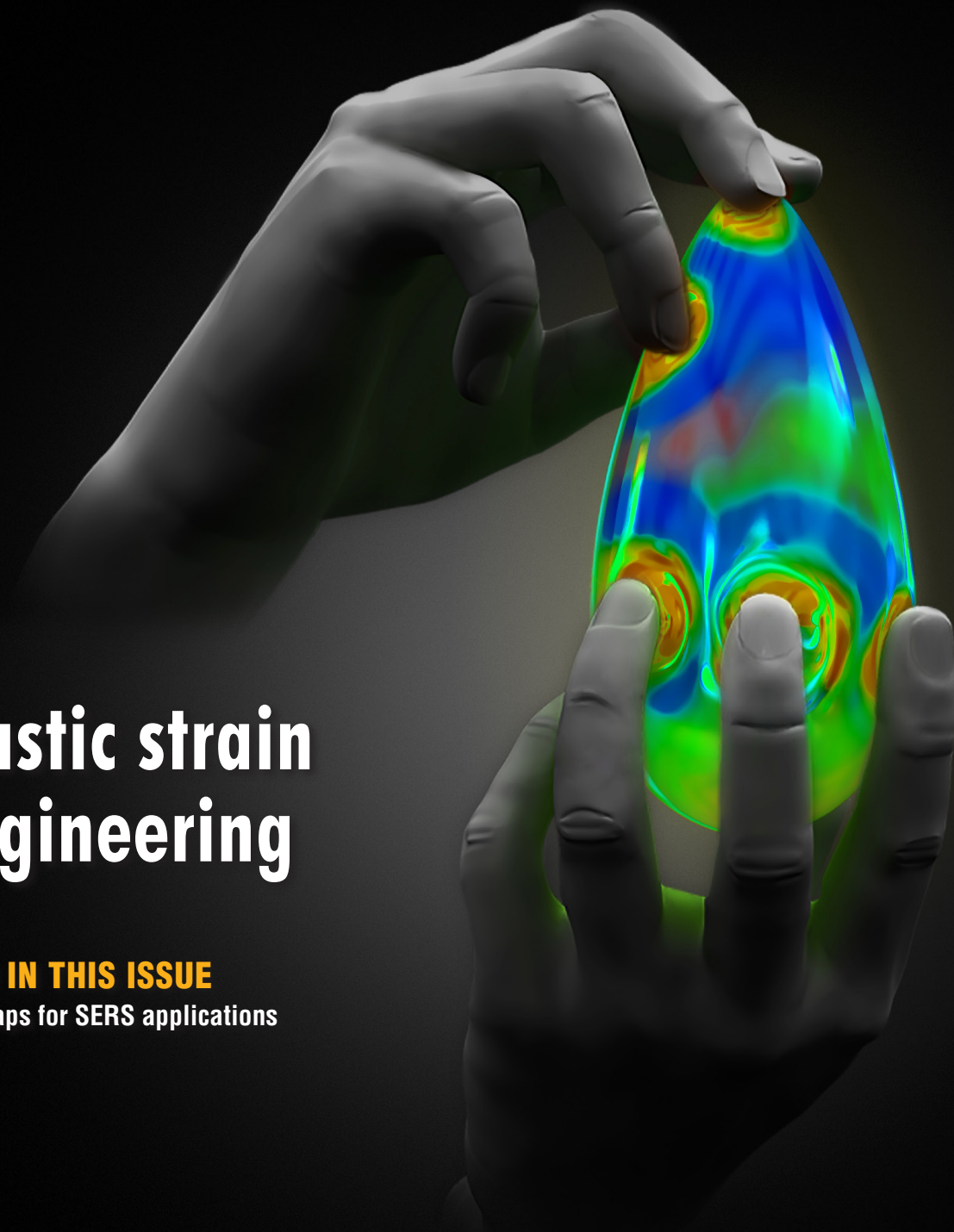


MRS Bulletin

February 2014 Vol. 39 No. 2
www.mrs.org/bulletin

MRS MATERIALS RESEARCH SOCIETY®
Advancing materials. Improving the quality of life.

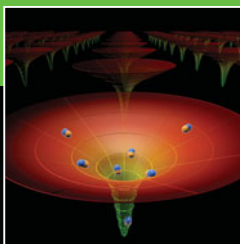


Elastic strain engineering

ALSO IN THIS ISSUE

Nanogaps for SERS applications

CAMBRIDGE
UNIVERSITY PRESS



Elastic strain engineering for unprecedented materials properties

Ju Li, Zhiwei Shan, and Evan Ma, Guest Editors

“Smaller is stronger.” Nanostructured materials such as thin films, nanowires, nanoparticles, bulk nanocomposites, and atomic sheets can withstand non-hydrostatic (e.g., tensile or shear) stresses up to a significant fraction of their ideal strength without inelastic relaxation by plasticity or fracture. Large elastic strains, up to ~10%, can be generated by epitaxy or by external loading on small-volume or bulk-scale nanomaterials and can be spatially homogeneous or inhomogeneous. This leads to new possibilities for tuning the physical and chemical properties of a material, such as electronic, optical, magnetic, phononic, and catalytic properties, by varying the six-dimensional elastic strain as continuous variables. By controlling the elastic strain field statically or dynamically, a much larger parameter space opens up for optimizing the functional properties of materials, which gives new meaning to Richard Feynman’s 1959 statement, “there’s plenty of room at the bottom.”

A vision of nano

At an American Physical Society meeting banquet on Dec. 29, 1959, Richard Feynman gave a talk entitled, “There’s Plenty of Room at the Bottom.”¹ He envisioned a strange future in which the entire 24 volumes of the *Encyclopedia Britannica* are written and read on the head of a pin using an electron microscope, where one makes a billion little lathes and “hands” to make still smaller lathes. Five decades later, we are well on our way to the prescient predictions of Feynman, a field now known as nanoscience and nanotechnology. Beyond mundane geometric scaling, Feynman envisioned fundamental physical and mechanical challenges and discoveries arising with miniaturization, such as problems with lubrication (“let the bearings run dry”), actuation (“internal combustion engine is impossible”), and “new kinds of effects.”

In this issue of *MRS Bulletin*, we focus on one such “new kind of effects” that has already given us better lasers, faster transistors, better catalysts, and is poised to offer much more in the foreseeable future. At its root, this effect arises out of a mantra in the mechanics of materials, “smaller is stronger,”² the science of which started in the 1950s³ and is vigorously developing today, and which Feynman could not have known about in 1959. He would be interested in its consequence: as nanomaterials are mechanically much stronger, at low temperatures at least,⁴ we can apply far greater shear or tensile stresses to tune their physicochemical properties than is

possible with traditional materials before the onset of plasticity or fracture, which relaxes the stress, elastic strain, and strain-tunable functional properties. Thus with so-called “ultra-strength materials,”² such as nanostructured silicon, pseudomorphic platinum film, and MoS₂ atomic sheet,^{5,6} we can rationally engineer the six-dimensional (6D) elastic strain ϵ_e , a continuously tunable set of variables, just like we can tune the chemical composition of a septenary alloy. The strain game would be to tune the electronic, magnetic, optical or plasmonic, ionic, phononic, thermoelectric, or catalytic properties, which is denoted as A for “any” physicochemical property or figure-of-merit, such as bandgap, carrier mobility, superconducting transition temperature, or electrocatalytic activity of a given material.

A window of opportunity has thus opened and has gotten wider over the last two decades, to a vast unexplored space for materials and device development, the size of which is probably unprecedented ever since chemical alloying was discovered. To paraphrase Feynman, there is not only room at the bottom, there is plenty of room at the bottom—by elastic strain engineering. The “room” we have in mind is the parametric space of ϵ_e , the volume of which scales as a generic deviatoric (non-hydrostatic) elastic limit ϵ_{ec} to the fifth power. ϵ_{ec} , in accordance with “smaller is stronger,”¹ scales up as $\epsilon_{ec} \propto L^{-\alpha}$, where L is a dominant characteristic length scale of the material that can be the grain size in a bulk nanocrystalline

Ju Li, Massachusetts Institute of Technology, USA; liju@mit.edu
Zhiwei Shan, Xi’an Jiaotong University, China; zwshan@mail.xjtu.edu.cn
Evan Ma, Johns Hopkins University, USA; ema@jhu.edu
DOI: 10.1557/mrs.2014.3

material as in the Hall-Petch relation,⁷ the thin-film thickness, or the sample size⁸, and α is an exponent,² usually between 0.5 and 1. This space of opportunity is much larger than that of high-pressure physics, which scales linearly with the pressure limit. Indeed, strain engineering (SE)—which consists of both elastic strain engineering (ESE) and inelastic strain engineering (ISE), is by definition a superset of high-pressure physics.

Material under strain

High-pressure physics has demonstrated that amazing physical properties can be achieved by stress; for example, solid sodium can be turned into an electronic insulator and become transparent to visible light⁹ by applying a large compressive stress ($\sigma_{11} = \sigma_{22} = \sigma_{33} = -P < 0$) conveyed by a pressure-transmitting fluid in a diamond anvil cell. It is well known that all properties of a crystalline material depend on its lattice parameters and the shape of the unit cell. However, it is only in the last two decades that the possibility of applying a large non-hydrostatic stress, for example a shear stress τ ($\sigma_{11} = \tau, \sigma_{22} = -\tau$), or a uniaxial tensile stress ($\sigma_{11} > 0, \sigma_{22} = \sigma_{33} = 0$), can be used experimentally to significantly alter the functional properties of a material. The main difficulty is that unlike hydrostatic pressure, both shear stress and tensile stress in materials can be relaxed by plasticity or fracture (see **Figure 1**, top right panel). Traditional materials usually cannot sustain elastic shear strain or tensile strain exceeding 0.2–0.3% before such inelastic relaxations set in. In recent years, however, a new class of materials called ultra-strength materials² has arisen, which can sustain shear or tensile strain exceeding 1% over the entire sample and for time periods sufficiently long for functional applications.

Some basic notions of mechanics of materials would be helpful for non-specialists. Strain $\boldsymbol{\varepsilon}$ is a 3×3 symmetric tensor, with six independent components. In this article, we focus on the non-hydrostatic (deviatoric) part of $\boldsymbol{\varepsilon}$, with $6 - 1 = 5$ independent components (the single hydrostatic degree of freedom is the domain of high-pressure physics). The total strain $\boldsymbol{\varepsilon}$ at a given point \mathbf{x} in the material can be decomposed into the sum of elastic strain and inelastic strain: $\boldsymbol{\varepsilon}(\mathbf{x}) \equiv \boldsymbol{\varepsilon}_e(\mathbf{x}) + \boldsymbol{\varepsilon}_i(\mathbf{x})$. $\boldsymbol{\varepsilon}_e(\mathbf{x})$ describes distortion of the Bravais lattice vectors of “good crystals” away from defect cores and can be directly measured by selected-area electron or x-ray diffractions. $\boldsymbol{\varepsilon}_i(\mathbf{x})$ corresponds to bonding topology or phase transformation changes and can be harder to experimentally quantify locally. To a good approximation, the local stress $\boldsymbol{\sigma}(\mathbf{x})$ is a function of only the local elastic strain: $\boldsymbol{\sigma}(\mathbf{x}) \approx \boldsymbol{\sigma}(\boldsymbol{\varepsilon}_e(\mathbf{x}))$. The analogy between strain field $\boldsymbol{\varepsilon}(\mathbf{x})$ and

chemical concentration field $\mathbf{c}(\mathbf{x})$ in alloys is apt, since both quantities are internally conserved and have volume integrals set by external boundary conditions (displacement and mass action, respectively). The elastic limit $\boldsymbol{\varepsilon}_{ec}$ is like the solubility limit of a single phase in chemical free energy: dumping $\boldsymbol{\varepsilon}(\mathbf{x})$ into a volume beyond $\boldsymbol{\varepsilon}_{ec}$ would cause “precipitation” of the total strain into inelastic strain $\boldsymbol{\varepsilon}_i(\mathbf{x})$, which is very large in amplitude but spatially localized^{10,11} (such as in between two adjacent atomic planes in dislocation-swept areas, where $\boldsymbol{\varepsilon}_i(\mathbf{x}) \sim 1$), plus a residual elastic strain field, which is delocalized spatially but is smaller in amplitude. In ESE, one aims to achieve an unconventionally large amplitude $\boldsymbol{\varepsilon}_e(\mathbf{x})$, which can be slowly varied in a pristine interior region to affect $A(\mathbf{x})$ of the “good crystal.”

Besides ESE, one can also engineer the inelastic strain pattern $\boldsymbol{\varepsilon}_i(\mathbf{x})$ to control properties, for example, by controlling slip or deformation twinning, martensitic phase transformation, or multiferroic domain patterns.¹² As inelastic strains are localized in microstructures such as dislocation-swept areas, new grains, or domain variants (or new martensitic phases), ISE is philosophically direct kin of “microstructure control properties,” probably the best known mantra in materials science. In certain applications, where the property of interest is phase

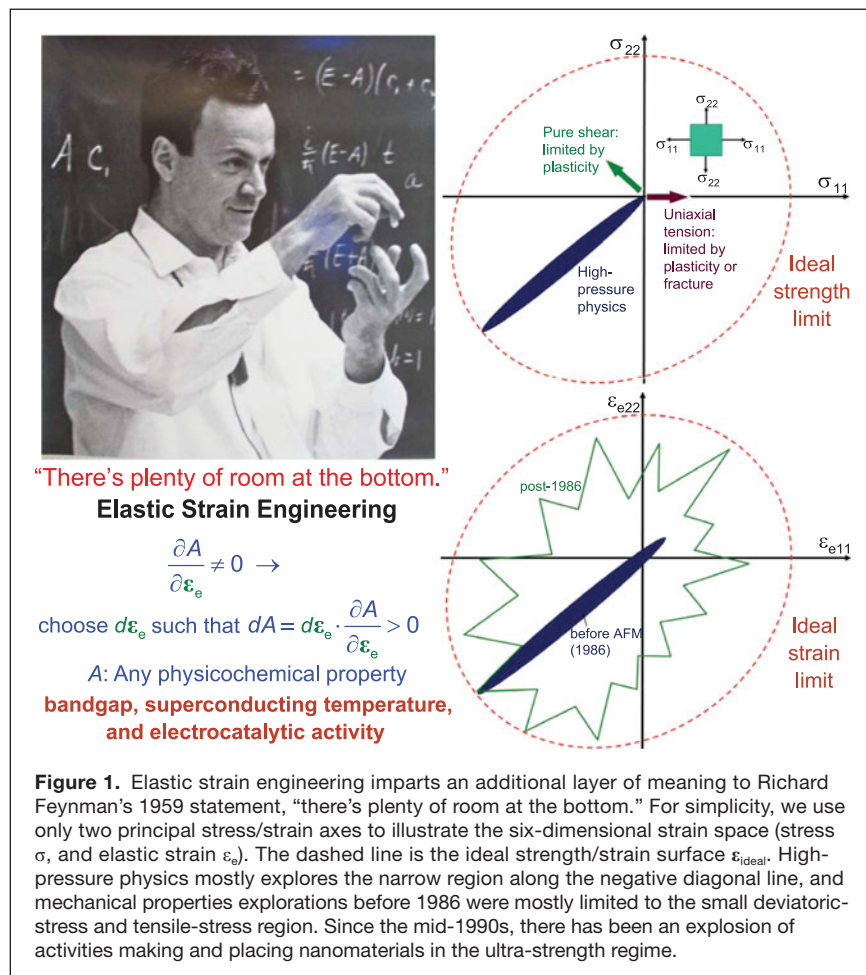


Figure 1. Elastic strain engineering imparts an additional layer of meaning to Richard Feynman’s 1959 statement, “there’s plenty of room at the bottom.” For simplicity, we use only two principal stress/strain axes to illustrate the six-dimensional strain space (stress σ , and elastic strain ε_e). The dashed line is the ideal strength/strain surface $\boldsymbol{\varepsilon}_{ideal}$. High-pressure physics mostly explores the narrow region along the negative diagonal line, and mechanical properties explorations before 1986 were mostly limited to the small deviatoric-stress and tensile-stress region. Since the mid-1990s, there has been an explosion of activities making and placing nanomaterials in the ultra-strength regime.

transformation, ESE and ISE are used in conjunction, and the entire approach is called SE. In this issue, Schlom et al. have a fascinating review on ESE and ISE of ferroic thin films. In this case, an approach is to first prepare the sample in pure ESE via epitaxial growth and elastic straining; and then for applications, to trigger multiferroic ISE transformations, whose key characteristics (such as Curie temperature) are changed by the ESE preparation in the first step. While the two effects, ESE and ISE, intimately couple in the second step, in the first step, one deals with pure ESE issues.

While microstructural/defect/domain engineering by ISE is very powerful, we focus more on the pure ESE aspects in this issue, wherein a large swath of the material is a “good crystal” and free of defects, with uniform or gradually varying $\epsilon_c(\mathbf{x})$ inside. In the context of pure ESE, microstructures (such as surfaces and grain boundaries), to the extent that they exist on the periphery, only assist in the buildup of $\sigma(\mathbf{x})$ and $\epsilon_c(\mathbf{x})$ in the defect-free interior. We study mechanisms of inelastic relaxations, but only for the purpose of defeating them. For example, one might wish to suppress dislocation nucleation and diffusional creep so one can inject and maintain a large $\epsilon_c(\mathbf{x})$, say 2% uniaxial tension along [111], in a piece of pristine silicon at 60°C for five years, which is the life expectancy of a personal computer. In the context of pure ESE, microstructural evolution is something to be avoided or suppressed, as it often leads to stress relaxation and storage of unpredictable defects in the interior, which may lead to degradation of functional properties such as carrier mobility. So the philosophy and objective of ESE are somewhat distinct from those of traditional materials processing. We note that historically, when metallurgists first described “microstructure control properties,” they had mostly mechanical properties in mind. They were not, by and large, thinking of fundamentally changing physical or chemical properties. ESE, on the other hand, aims to do exactly that. For example, through tensile straining, ESE aims to reduce the bandgap of germanium and change it from an indirect bandgap semiconductor to a direct bandgap semiconductor so it can become a better gain medium for lasers.¹³

The basic difference between “ultra-strength materials”² and conventional materials is the following. While a conventional piece of steel can easily stretch or bend by 30%, more than 99% of the injected total strain turns into plastic strain, and less than 1% of that remaining is elastic strain ϵ_c . Indeed, few conventional materials produced before 1970, whether steels or wafer-scale silicon, can withstand a sample-wide elastic strain level exceeding 1%, which is what one needs to achieve significant physical property changes. (From *ab initio* quantum mechanical calculations, we know for instance if the lattice constant of a semiconductor dilates by 1%, there can be ~100 meV change in the bandgap,⁵ which is significant).

The reason is simple. Steels have a Young’s modulus $E \sim 200$ GPa, so $\epsilon_c > 1\%$ means sustaining ~2 GPa stress sample-wide, which exceeds the yield strength of most steels. Thus, in a stress ramp-up experiment, dislocations would start to move

and multiply probably around $\epsilon_c = 0.3\%$ (if we assume a yield strength of 600 MPa), meaning we can no longer inject much more ϵ_c with further stretching or bending, while numerous dislocations start to evolve everywhere. The same is true for a bulk ingot of silicon or a silicon wafer ($E \sim 150$ GPa): $\epsilon_c > 1\%$ means sustaining 1.5 GPa tensile stress indefinitely. A 12-inch silicon wafer would fracture probably at one-tenth of that uniaxial tensile stress. Few materials produced before 1970 are therefore suitable for ESE.

ESE, as a theoretical concept, is not new, and many researchers likely have thought about it. But without real samples, ESE could not have become an experimental reality. Unbeknownst to most researchers, there were a few exceptions to this materials vacuum before 1970. Metallic whiskers grown at the General Electric Company with a smallest diameter of 1.2 μm were found to withstand several percent tensile elastic strain by Sidney S. Brenner in 1956.³ (These whiskers were the predecessors of nanowires that have been extensively studied since the late 1990s.)

Ultra-strength material is defined as being able to sustain sample-wide elastic strain levels exceeding 1% (for example, uniaxial tensile strain $\epsilon_{xx} > 1\%$ or engineering shear strain $\gamma_{xy} \equiv 2\epsilon_{xy} > 1\%$) at the service temperature of interest over anthropologically useful timescales such as months, years, or decades. The qualification of space-time volume is important: even with conventional materials, defect cores (such as at the crack tip) near the lattice can sustain very large stresses in a very local region. However, as stated earlier, in ESE, we try to avoid unintended defects and to use pristine material. Also, the qualification of service temperature is important. Ultra-strength materials are created by “going nano.” At lower temperatures, “smaller is stronger” is true for most nanomaterials due to size confinement of the dislocation population dynamics in ductile materials, or Weibull statistics of failure in brittle materials.² But when going to higher temperatures, smaller can be much weaker for nanomaterials due to the activation of diffusional creep.⁴ The transition temperature, T_{trans} , from “smaller is stronger” to “smaller is much weaker” scales with the melting point of the base material. Thus, ESE should be considered mostly for “hard nanomaterials” with relatively high melting points, for near-room-temperature applications, or below, such as superconducting cables.

The detailed reasons why nanostructured materials tend to have ultra-strength at lower temperatures, as well as the various mechanisms of stress relaxation, can be found in a comprehensive review.² A key reason is that free surfaces and grain boundaries influence the population dynamics of inelastic strain carrying defects such as glissile dislocations and cracks, driving the “smaller is stronger” trend. Size-dependent sample preparation and sample quality (initial defect densities) are also critically important.¹⁴

An ESE wonderland

Generally speaking, take any physical or chemical property A such as the thermoelectric figure of merit, ZT , the gradient

$\mathbf{g} \equiv \delta A / \delta \boldsymbol{\varepsilon}_e|_{a_0}$ is non-zero at the equilibrium lattice constant a_0 (unless A is the bulk Helmholtz free energy, per the definition of a_0). This means if we want to optimize A , the stress-free state a_0 is generally not the optimum, and by altering $\boldsymbol{\varepsilon}_e$ along $\pm \mathbf{g}$, we can achieve desired changes in A . If we want to increase A , we tweak $\boldsymbol{\varepsilon}_e$ along $+\mathbf{g}$; if we want to decrease A , we take $\boldsymbol{\varepsilon}_e$ along $-\mathbf{g}$. This amenability to tweaking, though trivial-sounding, is what historically chemical alloying gave us. In an alloy melt, the chemical composition $\mathbf{X} \equiv [X_{\text{Cu}}, X_{\text{Sn}}, X_{\text{Pb}}, \dots]$ is continuously tunable. Historically, the composition of a Chinese bronze “88.3 wt% Cu, 9.9 wt% Sn, 0.64 wt% Pb, . . .” was likely the outcome of a gradient-aided trial-and-error search, where A is a thermomechanical figure of merit, and \mathbf{X} was tweaked to see how much A changes until diminishing returns were produced (local optimum). The recipe “88.3 wt% Cu, 9.9 wt% Sn, 0.64 wt% Pb, . . .” was definitely not the outcome of *ab initio* quantum mechanical calculations or even a physical metallurgy understanding; for that we would have to wait until the end of the 20th century.

Of course, A may also “jump” sharply (instead of changing smoothly) if a first-order phase transformation is encountered upon changing \mathbf{X} , when one hits the solubility limit. So what is the maximum $\boldsymbol{\varepsilon}_e$ one can ever hope to inject into a lattice while maintaining a single-phase homogeneous (defect-free) state? The answer is $\boldsymbol{\varepsilon}_{\text{ideal}}$, the ideal strain, defined as the upper bound to how much elastic strain a perfect crystal (without defects or even surfaces) can withstand at $T = 0$ K without losing homogeneity. This can be calculated by forbidding imaginary phonon frequencies in the entire Brillouin zone,^{2,15} similar to the definition of local spinodal stability in single-phase solution (a positive-definite curvature in the free energy versus composition). Since $\boldsymbol{\varepsilon}_e$ lives in 6D space, $\boldsymbol{\varepsilon}_{\text{ideal}}$ is a 5D hypersurface, the crossing of which causes spontaneous strain localization.¹⁰ The magnitude of $\boldsymbol{\varepsilon}_{\text{ideal}}$ is generally on the order of 0.1 (Frenkel sinusoid argument),¹⁶ before the lattice spontaneously nucleates dislocations, cracks, or phase transforms, even at zero temperature.^{10,12} Thus, ultra-strength materials, defined as taking up more than 1% elastic strain, would be carrying more than one-tenth the theoretical ideal strength.

Note that $\boldsymbol{\varepsilon}_{\text{ideal}}$ is a concept, computable for an imagined perfect lattice under a periodic boundary condition at 0 K, whereas ultra-strength refers to an experimental reality about a real material at a finite temperature and with a significant space-time volume. Since “smaller is stronger,” the low-temperature strength champion, not surprisingly, is graphene, which has zero thickness in the z direction in the nuclei positions. A graphene monolayer experimentally demonstrated about a ~20% equal biaxial tensile elastic strain limit,¹⁷ in agreement with predictions of soft phonons by *ab initio* density functional perturbation theory (DFPT) calculations.¹⁵ Thus, the fact that ideal strain $\boldsymbol{\varepsilon}_{\text{ideal}}$ can be closely approached experimentally has been demonstrated.¹⁸

The late John J. Gilman, a giant in the field of mechanics of materials, wrote a book, *Electronic Basis of the Strength of Materials* (Cambridge University Press, 2008), in which he

explained the innate connection between ideal strength—the point where bond breaking or bond switching has to happen spontaneously—and dramatic electronic-structure changes, such as closure of the bandgap in semiconductors. Since nearly all physical and chemical properties of a material depend on the electronic structure, and since the electronic structure must be altered in a drastic way near the point of spontaneous bond breaking, a material near the ideal-strain surface $\boldsymbol{\varepsilon}_{\text{ideal}}$ will have unusual or even singular physical and chemical properties that are dramatically different from those of the stress-free state.

This has been demonstrated in the DFPT calculations for graphene:¹⁵ In the stress-free state, graphene has an $\omega \propto k^2$ bending phonon branch in the phonon dispersion curve (for angular frequency ω and wave number k); with tensile strain, the $\omega \propto k^2$ branch disappeared. When strain is increased further, a wide phononic bandgap opens up, which never existed in stress-free graphene. The 15%-stretched graphene is therefore a very different material from 1%-stretched graphene, phononically. Because the thermoelectric effect depends on phonon transport, and the Bardeen–Cooper–Schrieffer theory of superconductivity depends on electron-phonon coupling, dramatic changes in phonon dispersion may lead to dramatic changes in ZT , or the superconducting temperature T_c . In the same sense, 3%-strained germanium is unlike normal germanium,¹³ and 5%-strained germanium would also be different from 3%-strained germanium. Five percent stretched germanium is also different from 5%-sheared germanium.

In crystals, not only do the elementary-excitation (e.g., electron, phonon, magnon) bands shift in value with strain, they also change from $\omega \propto k^2$ dispersion to $\omega \propto |k|$ dispersion, or in the topology of which band branch is higher and which band branch is lower (band inversions). It is thus not surprising that even the “fragility” or robustness of topological insulators is proposed to be classified by how much elastic strain they can sustain before their topological non-trivialness (genus of band topology) changes.¹⁹ ESE not only has the ability to change values of properties, it can also push chemical and physical behavior toward singularities and induce topological changes, creating an ESE wonderland. This wonderland has been in the heads of theorists for a long time. But now, it is well poised to become an experimental reality in many materials subfields.

For monolayers such as graphene and MoS₂, as well as van der Waals heterostructures,⁶ the three in-plane strain components ε_{xx} , ε_{yy} , and ε_{xy} should be treated differently from the out-of-plane deformation characteristics. One may say that a true monolayer like graphene does not have out-of-plane strain, but in that case, due to the ease of bending, one must also consider the influence of elastic bending (3 degrees of freedom, the two principal bending curvature values plus the angle of one principal axis) on local physicochemical properties, which is a limiting case of the more general “flexoelectric” (“strain gradient $\nabla \boldsymbol{\varepsilon}_e$ ”) effect.²⁰ Furthermore, there are atomic coordinates’ “internal shuffling” degrees of freedom that may be exploited in MoS₂ and van der Waals heterostructures,⁶ so

the ESE wonderland of 2D materials is no less rich and exotic than that of 3D materials.

Recently, meticulously designed artificial “metamaterials” and origami materials have attracted much interest, with intended applications as photonic crystals, plasmonics, etc. When these materials are made of elastomers, or have bending/folding based architecture, they tend to be highly deformable in a reconfigurable manner (e.g., “mechanical metamaterials”) and therefore also provide a playground for ESE and ISE²¹ of photonic and phononic properties, for example.

Four pillars of ESE

ESE has one gigantic commercial success already that can serve as its poster child: strained silicon technology, where biaxial or uniaxial tensile strain up to a few percent is applied to a 10¹–10² nm wide silicon channel (by epitaxial strain to Si_{1-x}Ge_x substrate for example) to achieve dramatic acceleration in carrier mobility by up to a few hundred percent. The physics behind mobility enhancement is attributed mainly to the reduction of the effective mass of electron or hole carriers and band degeneracy lifting, which can be modeled by *ab initio* band structure calculations. This piezoresistance effect²² has been demonstrated for a long time. The physics is relatively straightforward. But achieving and sustaining $\epsilon_c > 1\%$ reliably in silicon in hundreds of millions of transistors for five years in real life, which is what is needed for computers and smartphones, is a great achievement of materials science and engineering. Note that the main reason silicon can take up a few percent tensile strain, without fracturing, is because it is in the form of a nanochannel (“small-volume material”) and not as a whole wafer.

The concept of strained silicon technology was revived at the Massachusetts Institute of Technology and Stanford University in the early 1990s, and IBM and Intel achieved major commercial successes in the mid-2000s, creating billions of dollars of added value every year. For the last decade, strained silicon technology has been one of the main contributors to so-called “non-classical scaling,” delaying the eventual breakdown of Moore’s law. In the article by Bedell et al. in this issue, this industrial technology is reviewed in detail. Strained semiconductors have also found commercial applications in quantum well lasers, light-emitting diodes, and many other optoelectronic applications.

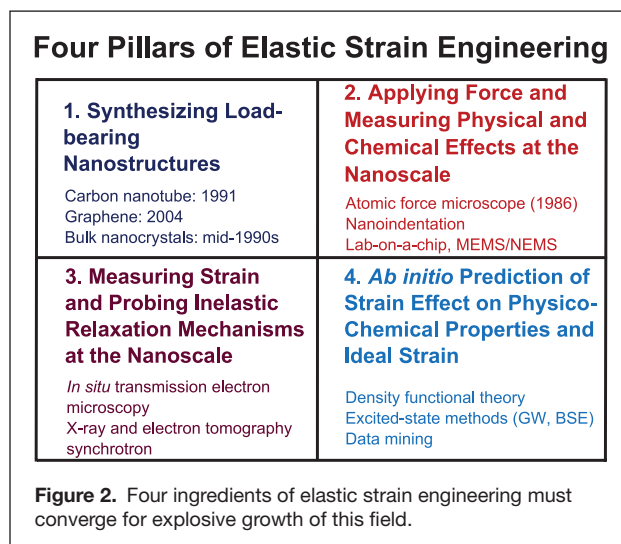
Still, ESE is relatively obscure today, if compared with what high school students know about what chemical metallurgy has done for human civilization (Bronze Age, Iron Age). Why is this the case? As shown in **Figure 2**, ESE requires four general ingredients or pillars: (1) synthesizing nanomaterials, (2) applying force at the nanoscale and measuring physical and chemical effects, by lab-on-a-chip for instance, (3) characterizing elastic strain distribution and deformation mechanisms, and (4) accurate *ab initio* modeling of strain effects on physicochemical properties and ideal strain. Some of these four ingredients did not exist before 1980, and their grand confluence started only in the late 1990s.

First, ESE requires nanomaterials that can take a large dynamic range of elastic strain. Carbon nanotubes were identified in 1991. Bulk nanocrystals were popularized in the mid-1990s. Without these advances in synthesis, and the explosive proliferation of nanomaterials today, ESE could not have taken off.

Second, for discovery-style exploration of the large parametric space of strain, one needs “hands” to apply forces at the nanoscale. Binnig and Rohrer received their Nobel Prize in Physics in 1986 for invention of the scanning tunneling microscope, which led Binnig, Quate, and Gerber to invent the atomic force microscope (AFM) also in 1986. We can use 1986 as a landmark in nanoscience and nanotechnology. After 1986, with subsequent development of instrumented nanoindentation²³ and MEMS/NEMS, the ability of humans to impose force and strain on materials at will at the nanoscale was greatly enhanced. To directly measure physical and chemical property changes at small scales, we also need to greatly advance lab-on-a-chip and MEMS/NEMS technologies. In the future, we probably need “a hundred tiny hands” (actuators) that Feynman envisioned and an equal number of sensors for local ESE measurements *in situ*.

Third, to experimentally measure the actual elastic strain distribution inside a functional material requires high-resolution microscopy and spectroscopy,²⁴ which have been continuously developing at stunning speed (see article by Hytch and Minor in this issue). If the intended elastic strain relaxes prematurely, one would also want to probe the mechanisms of stress relaxation (dislocation slip, diffusion, fracture, etc.) and methods to defeat them. These involve the development of both long-timescale modeling^{25,26} and *in situ* microscopy^{4,12,27,28} techniques for deformation mechanism studies.

Fourth, we are no longer in the Stone Age and need to go beyond trial-and-error approaches used by our ancestors for developing chemical metallurgy. The strain space is large and easy to get lost in, so we need theory and calculations to guide us toward the upper bound to elastic strain¹⁵ and



how much change in properties^{5,29} can be induced by strain. High-powered *ab initio* calculations, including both electronic ground-state and excited-state calculations,⁵ are crucially needed. This closely matches the philosophy behind the Materials Genome Initiative, which proposes accelerating materials discovery and development by computation and data mining.

Explosive growth of ESE requires careful and meticulous experiments, from synthesis to applying load, to characterizing strain distribution, to local property measurements and diagnostics. The agreement between theoretical predictions and measurements also builds confidence. The grand confluence of trends in the four pillars only started in the last two decades or so, and is accelerating rapidly today. In view of the long timescale our ancestors took to figure out chemical metallurgy, two decades is a just a blip on the time axis, and there is already a billion-dollar strained semiconductor industry to show for it. In view of the extraordinary number of properties elastic strain could affect, we are just getting started in our exploitations of ESE.

Recent progress

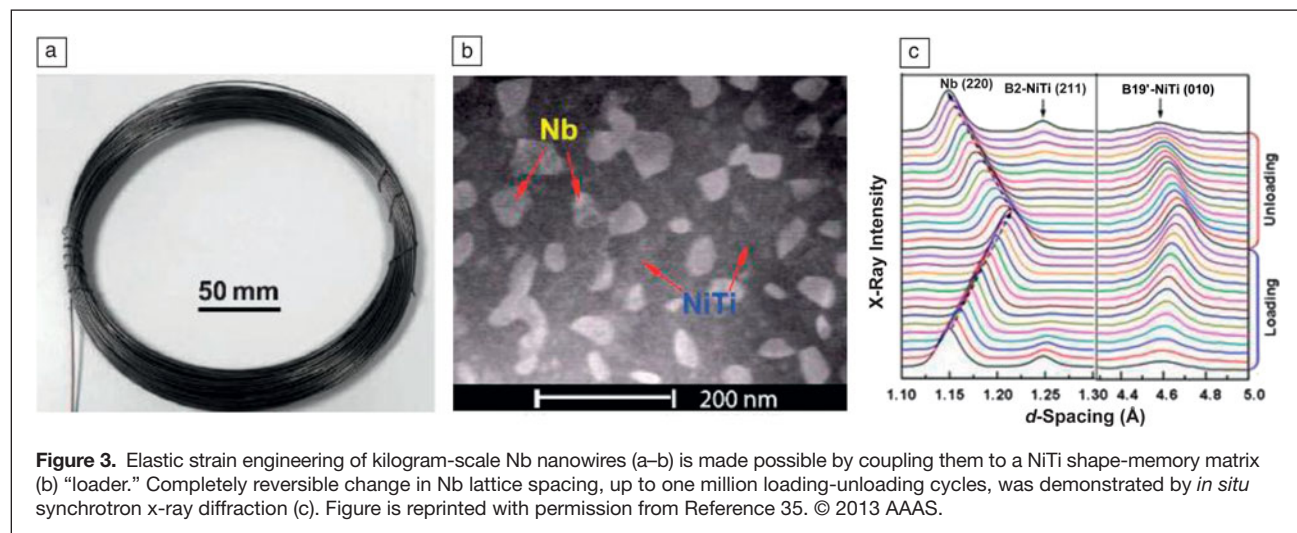
The first general symposium on ESE was held as part of the 2013 MRS Fall Meeting. The main purpose of this symposium was to (a) cross-link different materials communities: strained oxides, strained atomic sheets, strained catalysts, strained silicon technology, and nanomechanics, and (b) to delineate common toolkits (such as theory and modeling, lab-on-a-chip, and nanoelectromechanical systems) and roadmaps for rational ESE. The interdisciplinary and cross-materials-classes natures of the symposium were evident.

This issue of *MRS Bulletin* contains contributions from five invited speakers of the symposium, bringing together different communities that use elastic strain to control functional properties, from strained silicon technology (see article by Bedell et al.) that is already at the industrial scale, to strain effects on chemical kinetics, including ionic conductors and catalysts (see article by Yildiz), strained ferroic films for tuning phase

transformations (see article by Schlom et al.), and strained atomic sheets and nanowires for novel optoelectronic effects (see article by Yu et al.). The experimental and theoretical toolkits for ESE are highlighted, such as precisely measuring large elastic strain fields by microscopy (see article by Hÿtch and Minor) and spectroscopy, generating strain and measuring properties *in situ* by lab-on-a-chip and MEMS/NEMS, predicting what strain will do to physical and chemical properties (*ab initio* to continuum scale modeling), and monitoring as well as understanding how large an elastic strain can be sustained and for how long (deformation mechanisms, defect evolution, and failure in ultra-strength materials).

New applications of ESE are constantly emerging. While most of the ESE applications thus far use static, uniform elastic strain, one example of non-uniform ESE is to make strain-engineered atomic sheets as a broad-spectrum solar energy funnel. An atomic monolayer of MoS₂ can be stretched to 11% experimentally.³⁰ First-principles calculations show that monolayer MoS₂ has a tunable bandgap from 1.9 to 1.1 eV when the tensile biaxial elastic strain increases from 0% to 9%. A novel design for photovoltaic devices was proposed,⁵ where inhomogeneous elastic strain is imposed on a mechanically clamped 2D membrane. Force balance requires the local strain to scale like $1/r$ (where r is distance to the indenter) for circular geometry. Since the bandgap changes approximately linearly with the local strain, this imposes a $1/r$ like deformation potential on electron and hole carriers, creating an “artificial atom,” but in 2D.

The $1/r$ field leads to novel effects for both photon absorption and exciton transport. First, the spatially varying bandgap enables it to absorb a broad spectrum of solar photons. Second, like a funnel, the $1/r$ deformation potential induces ballistic motion of neutral excitons toward the center and thus reduces recombination probability. Third, at the “nucleus” of the artificial atom, two nano-electrodes with different work functions are envisioned to separate the exciton, thus the charge-separation region will be distinct and can be much smaller



than the photon-absorption region of the device. Calculations of the exciton lifetime and mobility indicate the photon-absorption “umbrella” can be up to microns in diameter. This strain-induced exciton funneling effect has been recently verified experimentally,^{31,32} and the same effect in elastically deformed nanowires was also demonstrated.^{33,34} (see article in this issue by Yu et al.).

While functional applications such as logic, sensing, and computing may require only a small total mass of active materials, applications such as ionic conduction and superconducting cables may require bulk-scale ultra-strength materials. Freestanding nanotubes and nanowires have ultrahigh elastic strain limits (4 to 7%) and yield strengths, but exploiting their intrinsic mechanical properties in bulk nanocomposites has historically proven to be challenging. Recently, the superior elastic limits of nanowires were shown³⁵ to be preserved in a phase-transforming matrix (**Figure 3**) based on the concept of elastic and transformation strain matching (ESE+ISE). By engineering the microstructure and residual stress to couple the true elasticity of Nb nanowires with the pseudoelasticity of a NiTi shape-memory alloy, a nanocomposite that possesses a large quasi-linear elastic strain of over 6%, a low Young’s modulus of ~28 GPa, and a high yield strength of ~1.65 GPa has been developed.³⁵ As verified by *in situ* synchrotron diffraction (see **Figure 3c**), one is able to, for the first time, stretch kilogram-scale nanowires to 6% elastic strain reversibly.³⁵ This strain-matching approach opens new avenues for developing bulk functional nanocomposites by coupling a shape-memory alloy “loader” with 0D, 1D, and 2D nanoscale components for ESE of kilogram-scale active materials, based on the observation that the true elastic strain range of many nanoscale objects (e.g., nanotubes, nanowires, quantum dots, graphene) happens to match the pseudoelasticity strain range of many shape-memory alloys. This may find applications in enhancing ion transport and catalysis (see article by Yildiz), thermoelectric energy harvesting, and superconductivity by ESE.

Conclusion

Considering what chemical alloying has accomplished for human civilization, the long-term possibilities for elastic strain engineering (ESE) are mind boggling. The much larger dynamic range of deviatoric elastic strains that nanomaterials can sustain over months and years, which can be tensile in character, leads to the “new kinds of effects” that Feynman envisioned. The explosive growth and timely confluence of the four ingredients needed for ESE—(1) synthesizing nanomaterials, (2) applying force at nanoscale and measuring physical and chemical effects, (3) characterizing elastic strain distribution and strain relaxation mechanisms, and (4) accurate *ab initio* modeling of strain effects on physicochemical properties—in

the past two decades and the significant commercial success of strained semiconductors technology suggest that we are just getting started in reaping tremendous benefits from ESE.

Acknowledgments

J.L. acknowledges support by NSF DMR-1240933 and DMR-1120901. The work at XJTU was supported by grants from NSFC (50925104, 51231005, and 51321003) and the 973 Programs of China (2010CB631003, 2012CB619402). We also acknowledge generous support of the 2013 MRS Fall symposium by Honda R&D Co. Ltd and Hysitron, Inc.

References

1. R.P. Feynman, *Caltech Engineering and Science* **23** (5), 22 (1960).
2. T. Zhu, J. Li, *Prog. Mater. Sci.* **55** (7), 710 (2010).
3. S.S. Brenner, *J. Appl. Phys.* **27** (12), 1484 (1956).
4. L. Tian, J. Li, J. Sun, E. Ma, Z.W. Shan, *Sci. Rep.* **3**, 2113 (2013).
5. J. Feng, X.F. Qian, C.W. Huang, J. Li, *Nat. Photonics* **6** (12), 865 (2012).
6. A.K. Geim, I.V. Grigorieva, *Nature* **499** (7459), 419 (2013).
7. S. Yip, *Nature* **391** (6667), 532 (1998).
8. M.D. Uchic, D.M. Dimiduk, J.N. Florando, W.D. Nix, *Science* **305** (5686), 986 (2004).
9. Y.M. Ma, M. Eremets, A.R. Oganov, Y. Xie, I. Trojan, S. Medvedev, A.O. Lyakhov, M. Valle, V. Prakapenka, *Nature* **458** (7235), 182 (2009).
10. J. Li, A.H.W. Ngan, P. Gumbsch, *Acta Mater.* **51** (19), 5711 (2003).
11. Y.Z. Wang, J. Li, *Acta Mater.* **58** (4), 1212 (2010).
12. L. Wang, P. Liu, P. Guan, M. Yang, J. Sun, Y. Cheng, A. Hirata, Z. Zhang, E. Ma, M. Chen, X. Han, *Nat. Commun.* **4**, 2413 (2013).
13. M.J. Suess, R. Geiger, R.A. Minamisawa, G. Schiefler, J. Frigerio, D. Christina, G. Isella, R. Spolenak, J. Faist, H. Sigg, *Nat. Photonics* **7** (6), 466 (2013).
14. Z.J. Wang, Z.W. Shan, J. Li, J. Sun, E. Ma, *Acta Mater.* **60** (3), 1368 (2012).
15. F. Liu, P.M. Ming, J. Li, *Phys. Rev. B* **76** (6), 064120 (2007).
16. J. Frenkel, *Z. Phys.* **37**, 572 (1926).
17. C. Lee, X.D. Wei, J.W. Kysar, J. Hone, *Science* **321** (5887), 385 (2008).
18. T. Zhu, J. Li, S. Ogata, S. Yip, *MRS Bull.* **34** (3), 167 (2009).
19. K.S. Yang, W. Setyawan, S.D. Wang, M.B. Nardelli, S. Curtarolo, *Nat. Mater.* **11** (7), 614 (2012).
20. M. S. Majdoub, P. Sharma, T. Cagin, *Phys. Rev. B* **77**, 125424 (2008).
21. Y. Cho, T.H. Ahn, H.H. Cho, J.H. Shin, J.H. Moon, S. Yang, I.S. Choi, H.N. Han, J. Li, *Model. Simul. Mater. Sci. Eng.* **21**, 065018 (2013).
22. C.S. Smith, *Phys. Rev.* **94** (1), 42 (1954).
23. A. Gouldstone, N. Chollacoop, M. Dao, J. Li, A.M. Minor, Y.L. Shen, *Acta Mater.* **55** (12), 4015 (2007).
24. I. De Wolf, *Semicond. Sci. Tech.* **11** (2), 139 (1996).
25. S. Hara, J. Li, *Phys. Rev. B* **82** (18), 184114 (2010).
26. J. Li, S. Sarkar, W.T. Cox, T.J. Lenosky, E. Bitzek, Y.Z. Wang, *Phys. Rev. B* **84** (5), 054103 (2011).
27. Q. Yu, Z.W. Shan, J. Li, X.X. Huang, L. Xiao, J. Sun, E. Ma, *Nature* **463** (7279), 335 (2010).
28. L. Tian, Y.Q. Cheng, Z.W. Shan, J. Li, C.C. Wang, X.D. Han, J. Sun, E. Ma, *Nat. Commun.* **3**, 609 (2012).
29. J.S. Qi, X.F. Qian, L. Qi, J. Feng, D.N. Shi, J. Li, *Nano Lett.* **12** (3), 1224 (2012).
30. S. Bertolazzi, J. Brivio, A. Kis, *ACS Nano* **5** (12), 9703 (2011).
31. K. He, C. Poole, K.F. Mak, J. Shan, *Nano Lett.* **13** (6), 2931 (2013).
32. A. Castellanos-Gomez, R. Roldán, E. Cappelluti, M. Buscema, F. Guinea, H.S.J. van der Zant, G.A. Steele, *Nano Lett.* **13** (11), 5361 (2013).
33. D. Nam, D.S. Sukhdeo, J.-H. Kang, J. Petykiewicz, J.H. Lee, W.S. Jung, J. Vučković, M.L. Brongersma, K.C. Saraswat, *Nano Lett.* **13** (7), 3118 (2013).
34. X. Fu, C. Su, Q. Fu, X. Zhu, R. Zhu, C. Liu, J. Xu, J. Feng, J. Li, D. Yu, *Adv. Mater.* (2014), accepted.
35. S.J. Hao, L.S. Cui, D.Q. Jiang, X.D. Han, Y. Ren, J. Jiang, Y.N. Liu, Z.Y. Liu, S.C. Mao, Y.D. Wang, Y. Li, X.B. Ren, X.D. Ding, S. Wang, C. Yu, X.B. Shi, M.S. Du, F. Yang, Y.J. Zheng, Z. Zhang, X.D. Li, D.E. Brown, J. Li, *Science* **339** (6124), 1191 (2013). □

**Ju Li**

Guest Editor for this issue of *MRS Bulletin*

Nuclear Science and Engineering, Massachusetts Institute of Technology, Cambridge, MA, USA; tel. 617-253-0166; and email liju@mit.edu.

Li is the BEA Professor of Nuclear Science and Engineering and a Professor of Materials Science and Engineering at MIT. Using atomistic modeling and *in situ* experimental observations, his group investigated mechanical, electrochemical, and transport behaviors of materials, often under extreme stress, temperatures, and radiation environments, as well as novel means of energy storage and conversion.

Ju was a winner of the 2005 Presidential Early Career Award for Scientists and Engineers, the 2006 MRS Outstanding Young Investigator Award, and the 2007 TR35 Award from *Technology Review*.

**Zhiwei Shan**

Guest Editor for this issue of *MRS Bulletin*

Xi'an Jiaotong University, China; tel. +86-13659185619; and email zhiweishan@gmail.com.

Shan is currently the Chang Jiang Professor at Xi'an Jiaotong University. He received his BS from Jilin University, MS from Institute of Metal Research, CAS and PhD degrees from the University of Pittsburgh. Following his postdoctoral research at Lawrence Berkeley National Laboratory, he joined Hysitron Inc. for four years. His research interests focus on applying and

developing unique quantitative *in situ* electron microscopy techniques and exploring and revealing the novel properties of micronanoscaled materials.

**Evan Ma**

Guest Editor for this issue of *MRS Bulletin*

Johns Hopkins University, Baltimore, MD, USA; tel. 410-516-8601; and email ema@jhu.edu.

Ma is currently a professor of materials science and engineering at Johns Hopkins University. He completed his undergraduate and graduate studies at Tsinghua University and Caltech and postdoctoral work at the Massachusetts Institute of Technology. He was an assistant and associate professor at Louisiana State University, and joined the Johns Hopkins faculty in 1998. His current research interests include metallic

glasses, chalcogenide alloys for memory applications, nanocrystalline metals, *in situ* TEM of small-volume materials, and elastic strain engineering of nanostructured metals and functional materials. Ma is a Fellow of ASM and APS.

**Stephen W. Bedell**

IBM T.J. Watson Research Center, New York, USA; tel. 914-945-2232; and email bedells@us.ibm.com.

Bedell received his BS and PhD degrees in physics from the State University of New York at Albany. He originally served as manager of research and development for Silicon Genesis Corporation in Campbell, Calif. He then joined IBM T.J. Watson Research Center in 2000 as a research staff member. His interests include strained-layer physics, crystal defects, ion-solid interactions, and advanced semiconductor materials.

Bedell has published over 80 articles and has over 150 issued or pending patents. He has received the IBM Outstanding Technical Achievement Award and was named IBM Master Inventor in 2012.

**Long-Qing Chen**

Millennium Science Complex, Materials Research Institute, University Park, PA, USA; tel. 814- 863-8101; and email lqc3@psu.edu.

Chen is a distinguished professor of materials science and engineering at Penn State University. He received his BS, MS, and PhD degrees from Zhejiang University, Stony Brook University, and the Massachusetts Institute of Technology, respectively, all in materials science and engineering. Chen has interests in computational materials science of phase transformations and microstructure evolution using the phase-field

method. He has received the TMS EMPMD Distinguished Scientist/Engineer Award (2011), and he is a Guggenheim Fellow and a Fellow of APS, ASM, and MRS.

**Ji Feng**

International Center for Quantum Materials, School of Physics, Peking University, and Collaborative Innovation Center of Quantum Matter, Beijing, China; email jfeng11@pku.edu.cn.

Feng earned his PhD degree in theoretical chemistry from Cornell University in 2007. He was a postdoctoral researcher at Harvard University and the University of Pennsylvania. He joined the faculty of the School of Physics at Peking University in 2011, where he is an associate professor in the International Center

for Quantum Materials. Feng is interested in electronic structure theory, and his research focuses on the effect of slowly varying fields and inhomogeneous order (such as strain) on the quantum behavior of electrons.

**Craig J. Fennie**

School of Applied and Engineering Physics, Cornell University, USA; email fennie@cornell.edu.

Fennie is currently an assistant professor in the School of Applied and Engineering Physics at Cornell University. He received his BEE and MSEE degrees from Villanova University, and his PhD in theoretical condensed-matter physics from Rutgers University in 2006. Upon graduation, he was awarded the Nicholas Metropolis Fellowship from Argonne National Laboratory. Since June 2008, he has been at

Cornell University, focusing on the application of first-principles methods to understand and discover new structurally and chemically complex oxides, with a particular interest in ferroelectric, multiferroic, and related multifunctional materials-by-design. He is the recipient of the 2010 Young Investigator Award from the ARO, the 2011 Faculty Early Career Development (CAREER) Award from the NSF, the 2012 Presidential Early Career Award for Scientists and Engineers (PECASE), and a 2013 MacArthur Fellowship.

**Venkatraman Gopalan**

Materials Science and Engineering, Penn State University, USA; email vgopalan@psu.edu.

Gopalan received his PhD degree in materials science and engineering from Cornell University in 1995. He became a full professor in materials science and engineering at Penn State in 2008. His interests are in symmetry, complex oxides, nonlinear optics, and devices. He has received the NSF Career Award, and the Robert R. Coble and Richard M. Fulrath Awards, both from the American Ceramics Society. He is a Fellow of the American Physical Society.



James Hone

Department of Electronic Engineering, Columbia University, New York, USA; email jh2228@columbia.edu.

Hone is currently a professor of mechanical engineering at Columbia University. He received his BS degree in physics from Yale University, and MS and PhD degrees in experimental condensed-matter physics from UC Berkeley. He completed postdoctoral work at the University of Pennsylvania and Caltech, where he was a Millikan Fellow. He joined the Columbia faculty in 2003. His current research interests include

mechanical properties, synthesis, and applications of graphene and other 2D materials; nanoelectromechanical devices; and nano-biology.



Martin Hÿtch

CEMES-CNRS, Toulouse, France; email martin.hytech@cemes.fr.

Hÿtch received his PhD degree from the University of Cambridge in 1991 before moving to France to work for the CNRS, first in Paris and then in Toulouse, where he heads the nanomaterials group. His research focuses on the development of quantitative electron microscopy techniques for materials science applications. He is the inventor of geometric phase analysis (GPA) and dark-field electron holography (DFEH). In 2008, he received the European Microscopy Award

(FEI-EMA), and he has published more than 100 papers and given over 30 invited talks at international conferences.



Ali Khakifirooz

IBM T.J. Watson Research Center, New York, USA; tel. 408-205-6338; and e-mail khaki@us.ibm.com.

Khakifirooz received BS and MS degrees from the University of Tehran, in 1997 and 1999, respectively, and his PhD degree from the Massachusetts Institute of Technology in 2007, all in electrical engineering. Since joining IBM Research in 2008, he has been involved in the development of 14-nm and 10-nm node technologies. He has authored or co-authored more than 75 technical papers and holds more than

70 issued US patents. Khakifirooz is a Senior Member of IEEE, an IBM Master Inventor, and a recipient of 71 IBM Invention Plateau Awards.



Andrew Minor

Department of Materials Science and Engineering, University of California, Berkeley, USA; tel. 510-495-2749; and email aminor@berkeley.edu.

Minor received a BA degree from Yale University and his MS and PhD degrees from U.C. Berkeley. Currently, he is an associate professor at U.C. Berkeley in the Department of Materials Science and Engineering. He also holds a joint appointment at the Lawrence Berkeley National Laboratory as the Deputy Director for Science in the Materials Science Division and Deputy Director

of the National Center for Electron Microscopy. He has co-authored over 100 peer-reviewed publications on topics such as nanomechanics, characterization of soft materials, and *in situ* TEM technique development. In 2012, he was awarded the Robert Lansing Hardy Award from TMS.



David A. Muller

School of Applied and Engineering Physics, Cornell University, USA; tel. 607-255-4065; and email dm24@cornell.edu.

Muller is a professor of Applied and Engineering Physics at Cornell University and co-director of the Kavli Institute at Cornell for Nanoscale Science. His current research interests include renewable energy materials, atomic resolution electron microscopy and spectroscopy, and the atomic-scale control of materials to create non-bulk phases. He is a graduate of the University of Sydney and received a PhD from Cornell

University and worked as a member of the technical staff at Bell Labs. He is a fellow of the American Physical Society and the Microscopy Society of America and a Burton Medalist.



Xiaoqing Pan

Department of Materials Science and Engineering, University of Michigan, USA; email panx@umich.edu.

Pan is the Richard F. and Eleanor A. Towner Professor of Engineering in the Department of Materials Science and Engineering at the University of Michigan. He received his BS and MS degrees in physics from Nanjing University in China and his PhD degree in physics from the University of Saarland in Germany. Pan's current research centers on understanding the atomic-scale structure-property relationships

of advanced functional materials, including oxide electronics, nanostructured ferroelectrics and multiferroics, battery materials, and catalysts. He received a CAREER Award from NSF and the Chinese NSFC's Outstanding Young Investigator Award. He was awarded and named Cheung-Kong Distinguished Visiting Chair Professorship and selected to China's 1000 Talent Program.



Ramamoorthy Ramesh

Oak Ridge National Laboratory, USA; email rameshr@ornl.gov.

Ramesh is the deputy director of Science and Technology at Oak Ridge National Laboratory. He received his PhD degree from the University of California, Berkeley in 1987. He returned to Berkeley in 2004 and is currently the Purnendu Chatterjee Chair Professor in Materials Science and Physics. Prior to that, he was a Distinguished University Professor at the University of Maryland College Park. He has received numerous awards, including the Materials Research

Society David Turnbull Lectureship Award (2007) and the 2010 APS McGroddy New Materials Prize. In 2009, he was elected Fellow of MRS, and in 2011, he was elected to the National Academy of Engineering.



Devendra Sadana

T.J. Watson Research Center, IBM, New York, USA; tel. 914-945-2423; and email dksadana@us.ibm.com.

Sadana obtained his PhD degree from IIT, New Delhi in 1975. He has worked at the University of Oxford, England, UC, Berkeley, MCNC Carolina, and Philips Research Labs, Sunnyvale, Calif. during 1975–1987 in various capacities. He joined IBM Research in 1987, where he is currently a senior staff/manager. His research work covers ion implantation, advanced epitaxial growth, SOI materials, main-

stream and flexible photovoltaics, and CMOS technology in Si and III–Vs. He has published over 200 papers in journals/conference proceedings. He is a co-inventor of over 300 issued/submitted patents. He is a Fellow of SPIE.



Darrell G. Schlom
Department of Materials Science and Engineering, Cornell University, USA; email schlom@cornell.edu.

Schlom is the Herbert Fisk Johnson Professor of Industrial Chemistry and Chair of the Department of Materials Science and Engineering at Cornell University. He received his BS degree from the California Institute of Technology, and his MS and PhD degrees from Stanford University. After working as a postdoctoral researcher at IBM's research lab in Zurich, Switzerland, Schlom was on the faculty at Penn State University for 16 years.

His research interests involve the growth and characterization of oxide thin films by MBE, including their integration with semiconductors. Schlom has published more than 400 papers and has eight patents. He has been awarded invention achievement awards by IBM and SRC; young investigator awards by ONR, NSF, and the American Association for Crystal Growth; an Alexander von Humboldt Research Fellowship; and the MRS Medal. In addition, Schlom is a Fellow of APS and MRS.



Reinhard Uecker
Leibniz Institute for Crystal Growth, Germany; tel. +49 30 63923021; and email reinhard.uecker@ikz-berlin.de.

Uecker is the leader of the oxides/fluorides group of the Leibniz Institute for Crystal Growth in Berlin, Germany. He received his Diploma from Humboldt University of Berlin and his PhD degree from the University of Hannover. He has worked in the field of crystal growth for over 30 years, specializing in the growth and characterization of oxide and fluoride single crystals from the melt. He spent 15 years growing

crystals at the Academy of Sciences in Berlin and continued at the Leibniz Institute for Crystal Growth since its foundation in 1992. Uecker is the author and co-author of more than 100 papers and holds five patents.



Bilge Yildiz
Massachusetts Institute of Technology, Nuclear Science and Engineering Department, Cambridge, MA 02139, USA; email byildiz@mit.edu.

Yildiz is an associate professor in the Nuclear Science and Engineering Department at the Massachusetts Institute of Technology (MIT), where she leads the Laboratory for Electrochemical Interfaces. She received her PhD degree at MIT in 2003 and her BSc degree from Hacettepe University in Turkey in 1999. Her research interests include molecular-level

studies of oxygen reduction kinetics on oxide surfaces at elevated temperatures, under stress and in reactive gases, by combining *in situ* surface sensitive experiments with first-principles calculations and novel atomistic simulations. She was the recipient of the Charles Tobias Young Investigator Award of the Electrochemical Society in 2012, and an NSF CAREER Award in 2011.



Dapeng Yu
State Key Laboratory for Mesoscopic Physics, School of Physics, Peking University, and Collaborative Innovation Center of Quantum Matter, Beijing China; email yudp@pku.edu.cn.

Yu is currently a professor of condensed-matter physics at the School of Physics at Peking University. He received his BS degree in materials science from East-China University, Shanghai, his MS degree at Shanghai Institute of Ceramics, Chinese Academy of Sciences, and his PhD degree in materials physics from Laboratoire de Physique des Solides, Université Paris-Sud,

Orsay, France. He joined the faculty in the physics department at Peking University in 1995. His current research interests include nanostructures and low-dimensional physics.

The MRS University Chapter Experience

The MRS University Chapter Program provides invaluable experiences and benefits for student members, but don't take our word for it. **Our Chapter Members Say It Best!**

- An International Community
- Interdisciplinary Collaboration
- Professional Growth
- Education Outreach
- Leadership Development

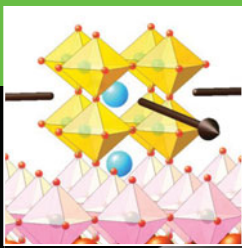
Leadership Development

The Materials Research Society, along with our local Binghamton University Chapter, has positively influenced my commitment to materials science and technology. We were inspired by our advisor, Professor M. Stanley Whittingham, to start this Chapter ... and motivated by his enthusiasm and our faith to bring science to the general public, we continue to hold numerous events taken from MRS, i.e. MAKING STUFF and NanoDays. As our organization grows, we keep growing our events, and have found a solid and welcoming place in our community. Apart from the target audience, our events also benefit the volunteers, who gained valuable experience both from preparation, interaction, and activities. We feel proud and grateful to be part of an MRS University Chapter.

Tianchan Jiang, Chapter President
Binghamton University
Binghamton, New York, USA

FOR MORE INFORMATION

on the MRS University Chapter Program, visit www.mrs.org/university-chapters



Elastic strain engineering of ferroic oxides

Darrell G. Schlom, Long-Qing Chen, Craig J. Fennie, Venkatraman Gopalan, David A. Muller, Xiaoqing Pan, Ramamoorthy Ramesh, and Reinhard Uecker

Using epitaxy and the misfit strain imposed by an underlying substrate, it is possible to elastically strain oxide thin films to percent levels—far beyond where they would crack in bulk. Under such strains, the properties of oxides can be dramatically altered. In this article, we review the use of elastic strain to enhance ferroics, materials containing domains that can be moved through the application of an electric field (ferroelectric), a magnetic field (ferromagnetic), or stress (ferroelastic). We describe examples of transmuting oxides that are neither ferroelectric nor ferromagnetic in their unstrained state into ferroelectrics, ferromagnets, or materials that are both at the same time (multiferroics). Elastic strain can also be used to enhance the properties of known ferroic oxides or to create new tunable microwave dielectrics with performance that rivals that of existing materials. Results show that for thin films of ferroic oxides, elastic strain is a viable alternative to the traditional method of chemical substitution to lower the energy of a desired ground state relative to that of competing ground states to create materials with superior properties.

The strain game

For at least 400 years, humans have studied the effects of pressure (hydrostatic strain) on the properties of materials.¹ In the 1950s, it was shown that biaxial strain, where a film is clamped to a substrate but free in the out-of-plane direction, can alter the transition temperatures of superconductors² (T_c) and ferroelectrics (T_C).³

What has changed in recent years is the magnitude of the biaxial strain that can be imparted. Bulk ferroic oxides are brittle and will crack under moderate strains, typically 0.1%. One way around this limitation is the approach of bulk crystal chemists, to apply “chemical pressure” through isovalent cation substitution. A disadvantage of such a bulk approach, however, is the introduction of disorder and potentially unwanted local distortions. Epitaxial strain, the trick of the thin-film alchemist, provides a potentially disorder-free route to large biaxial strain and has been used to greatly enhance the mobility of transistors^{4,5} (see the article by Bedell et al. in this issue), increase catalytic activity (see the article by Yildiz et

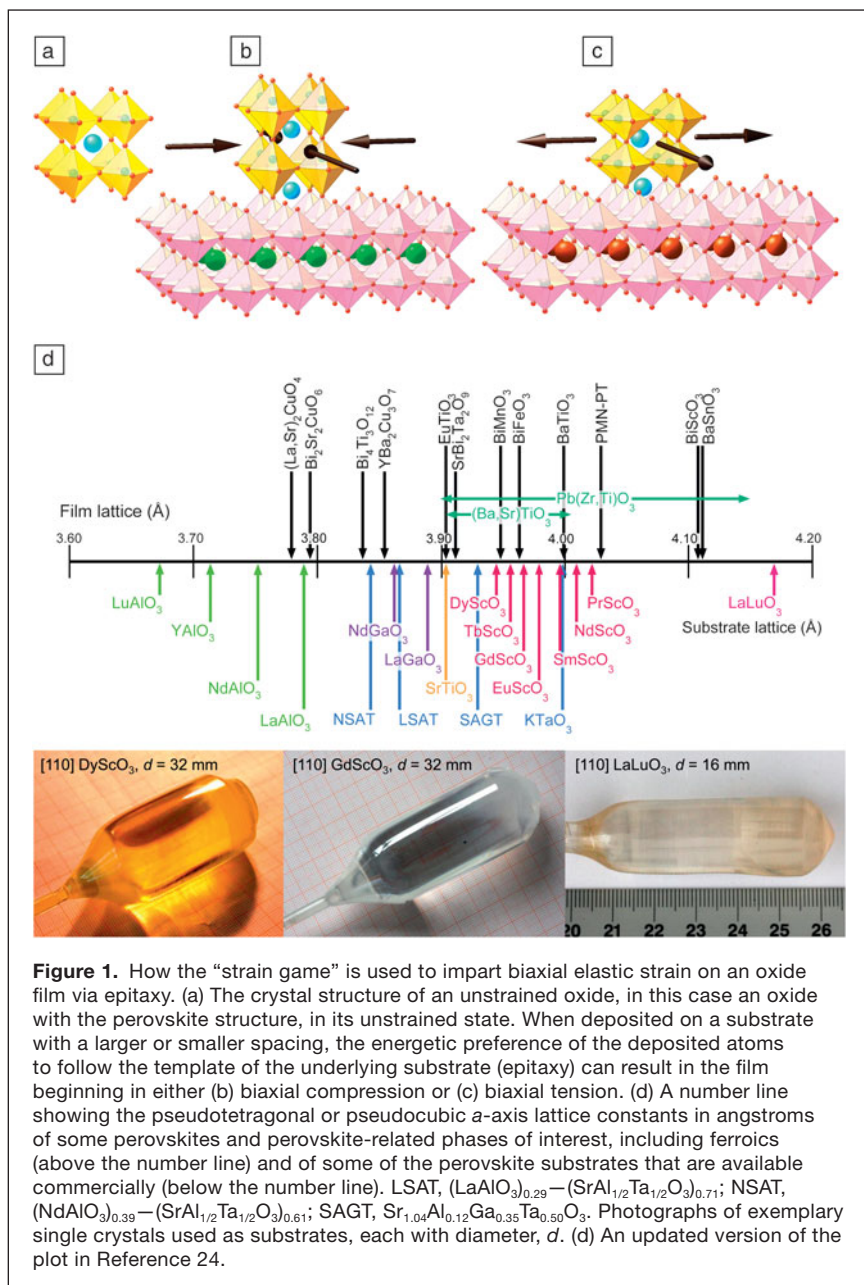
this issue), alter band structure⁶ (see the article by Yu et al. in this issue), and significantly increase superconducting,^{7,8} ferromagnetic,^{9–11} and ferroelectric^{12–16} transition temperatures. This approach, which we refer to as the “strain game,” is illustrated in **Figure 1** for elastically strained films of oxides with the perovskite structure.

Strains of about $\pm 3\%$ are common in epitaxial oxide films today,^{17–20} with the record to date being a whopping 6.6% compressive strain achieved in thin BiFeO₃ films grown on (110) YAlO₃.^{21–24} These strains are an order of magnitude higher than where these materials would crack in bulk.^{25–27}

Strained SrTiO₃ and the importance of suitable substrates

The strain game for ferroics was ignited by the demonstration that an oxide that normally is not ferroelectric at any temperature can be made ferroelectric at room temperature through the application of biaxial strain.¹² Such a gigantic shift in properties and T_C had never before been clearly seen in any

Darrell G. Schlom, Department of Materials Science and Engineering, Cornell University and Kavli Institute at Cornell for Nanoscale Science; schlom@cornell.edu
Long-Qing Chen, Millennium Science Complex, Materials Research Institute, Penn State University; lqc3@psu.edu
Craig J. Fennie, School of Applied and Engineering Physics, Cornell University; fennie@cornell.edu
Venkatraman Gopalan, Materials Science and Engineering, Penn State University; vgopalan@psu.edu
David A. Muller, School of Applied and Engineering Physics, Cornell University and Kavli Institute at Cornell for Nanoscale Science, Cornell; dm24@cornell.edu
Xiaoqing Pan, Department of Materials Science and Engineering, University of Michigan; panx@umich.edu
Ramamoorthy Ramesh, Oak Ridge National Laboratory; rameshr@ornl.gov
Reinhard Uecker, Leibniz Institute for Crystal Growth, Berlin; reinhard.uecker@ikz-berlin.de
DOI: 10.1557/mrs.2014.1

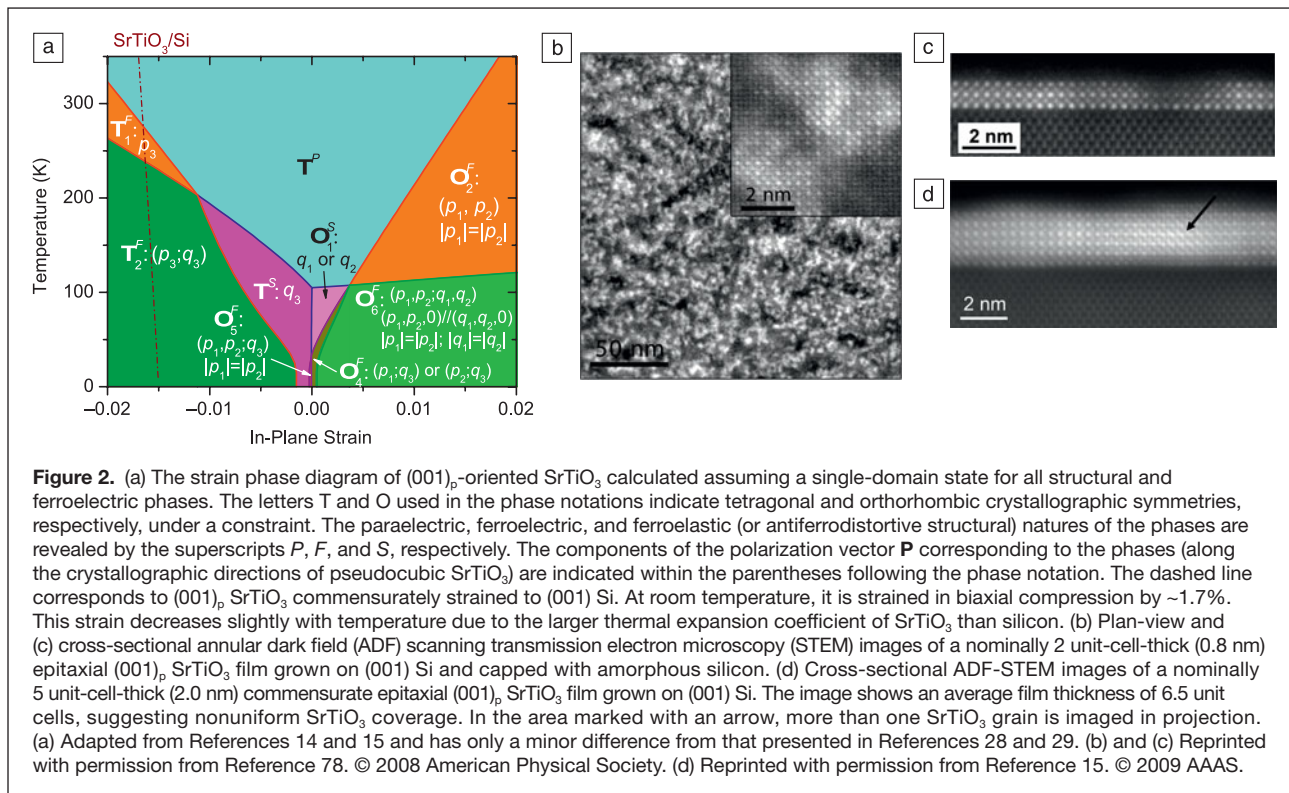


ferroic system; nonetheless, this achievement was the experimental realization of what had been predicted years earlier by theory.^{28,29} **Figure 2** shows the strain phase diagram of $(001)_p$ SrTiO_3 calculated by thermodynamic analysis,^{12,14,15,28–30} where the *p* subscript indicates pseudocubic Miller indices. These predictions imply that a biaxial tensile strain on the order of 1% will shift the T_C of SrTiO_3 to the vicinity of room temperature.^{12,28–32} Although many researchers had grown SrTiO_3 films on substrates with different spacings, the lattice mismatches were so large and the films so thick that the films were no longer elastically strained.

Fully commensurate, elastically strained epitaxial films have the advantage that high densities of threading dislocations

(e.g., the $\sim 10^{11}$ dislocations cm^{-2} observed, for example, in partially relaxed $(\text{Ba}_x\text{Sr}_{1-x})\text{TiO}_3$ films)^{33,34} are avoided. Strain fields around dislocations locally alter the properties of a film, making its ferroelectric properties inhomogeneous and often degraded.^{35–37} To achieve highly strained ferroic films and keep them free of such threading dislocations, one needs to keep them thin, typically not more than a factor of five beyond the Matthews-Blakeslee critical thickness, beyond which it becomes energetically favorable (though typically constrained by kinetics) for a film to relax by the introduction of dislocations.^{27,38} Thickness-dependent studies, involving the growth of a ferroic on just one substrate material to study the effect of strain in partially relaxed films, are not as easy to interpret as experiments utilizing commensurate films grown on several different substrate materials covering a range of lattice spacings. In the former, the strains are inhomogeneous, and the high concentration of threading dislocations can obfuscate intrinsic strain effects.

Exploring the strain predictions in Figure 2a was greatly simplified by the development of new substrates with a broad range of spacings to impart a desired strain state into the overlying SrTiO_3 film. These substrates have the same structure as SrTiO_3 —the perovskite structure—but different lattice spacings. The number of perovskite single crystals that are available commercially as large substrates (with surfaces at least $10\text{ mm} \times 10\text{ mm}$ in size) has nearly doubled in the last decade due to the work of the present authors.^{39–41} Today, various single crystal perovskite and perovskite-related substrates are commercially available (see Figure 1d), including LuAlO_3 ,^{42,43} YAlO_3 ,⁴⁴ LaSrAlO_4 ,⁴⁵ NdAlO_3 ,⁴⁶ LaAlO_3 ,^{47,48} LaSrGaO_4 ,⁴⁹ $(\text{NdAlO}_3)_{0.39} - (\text{SrAl}_{1/2}\text{Ta}_{1/2}\text{O}_3)_{0.61}$ (NSAT),⁵⁰ NdGaO_3 ,^{51,52} $(\text{LaAlO}_3)_{0.29} - (\text{SrAl}_{1/2}\text{Ta}_{1/2}\text{O}_3)_{0.71}$ (LSAT),^{50,53} LaGaO_3 ,⁵⁴ SrTiO_3 ,^{55–58} $\text{Sr}_{1.04}\text{Al}_{0.12}\text{Ga}_{0.35}\text{Ta}_{0.50}\text{O}_3$ (SAGT), DyScO_3 ,^{12,39} TbScO_3 ,⁴⁰ GdScO_3 ,^{13,39,59} EuScO_3 ,^{39,60} KTaO_3 ,⁶¹ NdScO_3 ,^{39,62} PrScO_3 ,⁶³ and LaLuO_3 ,⁶⁴ many of these are produced with structural perfection rivaling that of conventional semiconductors. The perfection of the substrate, the best of which are grown by the Czochralski method (which is not applicable to most ferroic oxides because they do not melt congruently), can be passed on to the film via epitaxy. This has led to the growth of strained epitaxial films of the ferroics SrTiO_3 ,^{38,65} BaTiO_3 ,¹⁴ BiFeO_3 ,⁶⁶ BiMnO_3 ,⁶⁷ and EuTiO_3 ,¹⁶ with rocking curve full width at half maximum values ≤ 11 arcsec (0.003°)—identical to those of the commercial substrates upon which they are grown and significantly narrower



(indicative of higher structural perfection) than the most perfect bulk single crystals of these same materials.

Using these new perovskite substrates, predictions of the SrTiO₃ strain phase diagram shown in Figure 2 were assessed. Not only was it found possible to transmute SrTiO₃ into a room temperature ferroic,^{12,68,69} but the experimentally determined point group,^{31,32,70–72} direction and magnitude of spontaneous polarization (P_S),^{31,32,65,70–73} observed shifts in T_C ^{12,70,71} and soft mode frequency with biaxial strain,⁷⁴ and existence of a transition to a simultaneously ferroelectric and ferroelastic phase at lower temperatures^{70–72,74} were all in accord with theory. Not all of the experimental observations, however, were in agreement with theory. For example, it was observed that strained SrTiO₃ films exhibit a significant frequency dependence to their dielectric response.^{65,73} This relaxor ferroelectric behavior is due to defects. On account of the strain, the SrTiO₃ matrix is highly polarizable and can be easily polarized by defect dipoles that arise from non-stoichiometry in the SrTiO₃ film. Based on how the properties of strained SrTiO₃ films vary with non-stoichiometry, strained, perfectly stoichiometric SrTiO₃ films are not expected to show relaxor behavior.⁷⁵

To make it possible for strain-enabled or strain-enhanced functionalities to be exploited in mainstream device architectures, it is desirable to play the strain game on substrates relevant to the semiconductor industry. One such example is the integration of commensurately strained SrTiO₃ films with silicon.¹⁵ The lattice mismatch between (001)_p SrTiO₃ and (001) Si is 1.7%, as indicated by the dashed line on the left side of the strain phase diagram in Figure 2a. From theory

(Figure 2a), such a film would be expected to be ferroelectric with a T_C near room temperature. This integration is, however, rather challenging due to (1) the high reactivity of silicon with many elements and their oxides,^{76,77} and (2) the thermodynamic driving force for a pristine silicon surface to oxidize and form an amorphous native oxide (SiO₂), which blocks epitaxy, under the oxidizing conditions typically used for the growth of oxide thin films. Despite these impediments, thin commensurate SrTiO₃ films have been grown directly on silicon without discernible intermediate layers and free of reaction, and are found to be ferroelectric at room temperature.¹⁵

Planar-view and cross-sectional annular dark field (ADF) scanning transmission electron micrographs (STEM) of epitaxial (001)_p SrTiO₃ films grown on and commensurately strained to (001) Si are shown in Figure 2b–d. Although the interface between SrTiO₃ and silicon is seen to be abrupt and free of reaction, these images reveal additional challenges to the growth of SrTiO₃ on silicon. First is the propensity of SrTiO₃ to nucleate as islands and not wet the surface of the silicon substrate.⁷⁸ Even using kinetically limited growth conditions,^{15,79} it takes multiple unit cells of growth before the SrTiO₃ islands coalesce.⁷⁸ Second are frequent out-of-phase boundaries in the SrTiO₃ film (see Figure 2d) resulting from the step height of (001) Si (0.14 nm) not matching the step height of (001)_p SrTiO₃ (0.39 nm). Out-of-phase boundaries can form during the coalescence of SrTiO₃ islands that have nucleated on different (001) Si terraces. The arrow in Figure 2d marks an area where the SrTiO₃ islands are out-of-phase with each other.

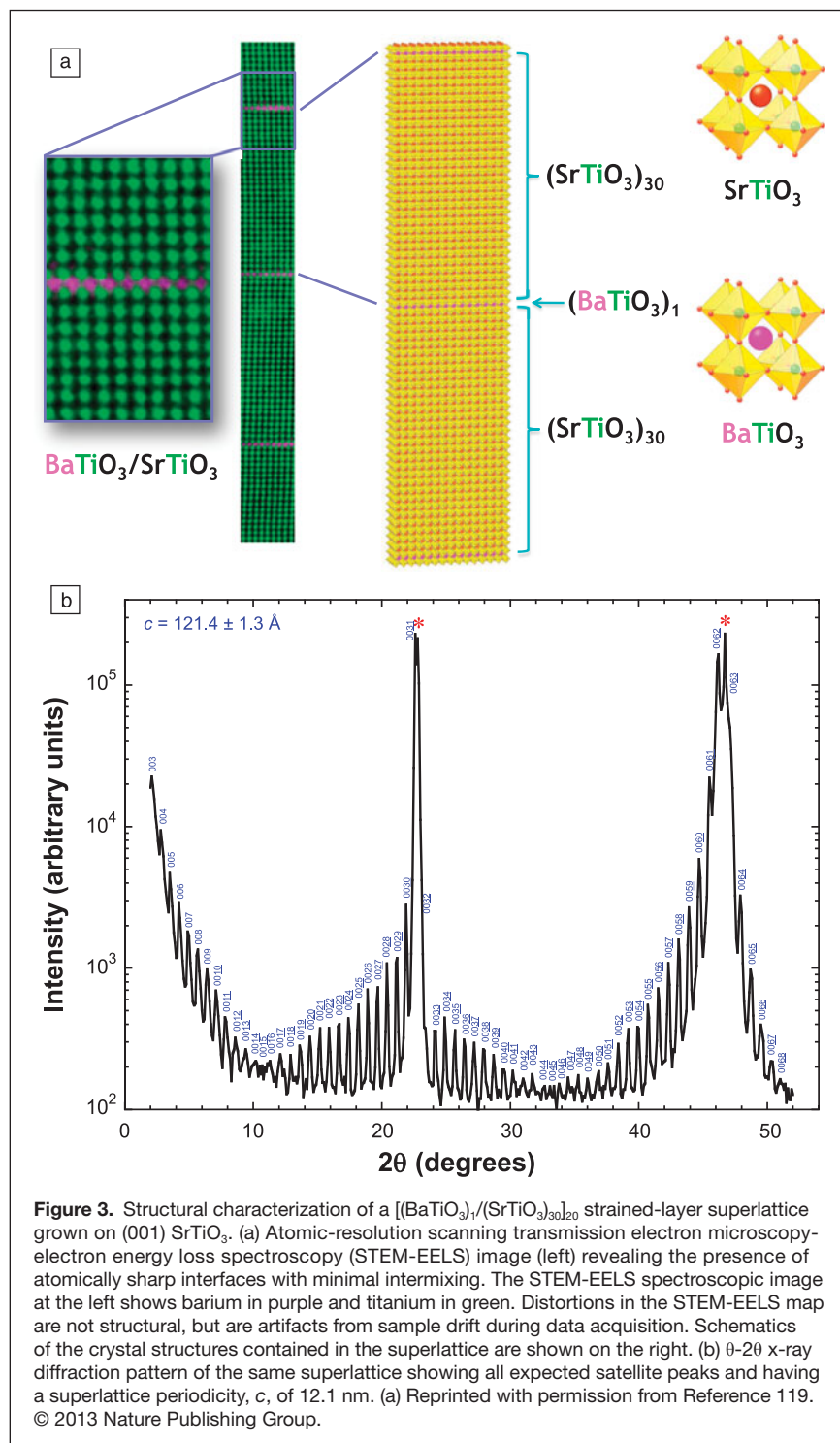
For the growth of high-quality films of ferroic oxides with a desired strain state, not only are appropriate substrates of exceptionally high perfection needed, but also methods to prepare them with smooth, well-ordered surfaces with a specific chemical termination on which epitaxial growth can be reliably initiated. For example, chemical-mechanically polished (001) SrTiO₃ substrates display a mixture of SrO- and TiO₂-terminated surfaces.

A combination of chemical etching and annealing has been shown to yield SrTiO₃ substrates with known surface termination. Kawasaki et al.⁸⁰ showed that an NH₄F-buffered HF solution with controlled pH enables etching of the more basic SrO layer and leaves a completely TiO₂ terminated surface on the substrate. This method of preparing a TiO₂-terminated (001) SrTiO₃ surface has been further perfected by Koster et al.⁸¹ SrO-terminated (001) SrTiO₃ substrates can also be prepared.⁸² A means to prepare low defect surfaces with controlled termination has since been developed for (110) SrTiO₃,⁸³ (111) SrTiO₃,^{83,84} (001)_p LaAlO₃,^{85,86} (111)_p LaAlO₃,⁸⁵ (110) NdGaO₃,⁸⁶ (001)_p LSAT,^{86,87} (110) DyScO₃,^{88,89} (110) TbScO₃,⁸⁸ (110) GdScO₃,⁸⁸ (110) EuScO₃,⁸⁸ (110) SmScO₃,⁸⁸ (001) KTaO₃,⁹⁰ (110) NdScO₃,⁸⁸ and (110) PrScO₃.⁸⁸ substrates.

The strain game is capable of enhancing the properties of a multitude of ferroelectric systems. Shifts in ferroelectric T_c of roughly 300 K per percent biaxial strain, quite comparable to those predicted^{28–32} and observed^{12,68–74} for SrTiO₃, were first predicted by theory and subsequently verified by experiments on biaxially strained BaTiO₃^{13,14,91–94} and PbTiO₃^{14,91,95–100} films. Strain effects of comparable magnitude have also been observed in strained (Ba,Sr)TiO₃ films^{101,102} and in strained-layer superlattices: KTaO₃/KNbO₃,¹⁰³ SrTiO₃/SrZrO₃,¹⁰⁴ SrTiO₃/BaZrO₃,¹⁰⁵ PbTiO₃/SrTiO₃,^{106,107} BaTiO₃/SrTiO₃,^{108–111} and CaTiO₃/SrTiO₃/BaTiO₃.^{112–114}

The success of theory in predicting the effect of strain on a multitude of ferroelectrics, together with advances in the ability to customize the structure and strain of oxide heterostructures at the atomic-layer level, has enabled a new era: ferroelectric oxides by design.¹⁴ The appropriate theoretical methods to design strain-enhanced ferroelectrics depend on the material and whether or not domains need to be taken into account. First-principles methods are good for new materials where the coefficients of the Landau–Devonshire free energy expansion,³⁰ a Taylor expansion of the

free energy of a material in powers of its order parameter (polarization for typical ferroelectrics), are unknown. Due to the relatively small number of atoms that can be included in such calculations, however, the calculations are limited to single-domain materials. Measurements on materials can yield the coefficients needed in Landau–Devonshire thermodynamic analysis to calculate the effect of strain in the absence of domains.³⁰



Phase-field simulations, which also require coefficients obtained from either experiment or first-principles calculations, can be used to take domains into account.^{97,98} An example is $(\text{BaTiO}_3)_n/(\text{SrTiO}_3)_m$ strained-layer superlattices, where n and m refer to the thickness, in unit cells, of the $(001)_p$ BaTiO_3 and $(001)_p$ SrTiO_3 layers, respectively. Despite the 2.3% lattice mismatch between the $(001)_p$ BaTiO_3 and $(001)_p$ SrTiO_3 layers, such superlattices can be commensurately strained. In **Figure 3**, the structural characterization of a commensurate $(\text{BaTiO}_3)_n/(\text{SrTiO}_3)_m$ superlattice with $n = 1$ and $m = 30$ is shown. The macroscopic regularity of this superlattice, which was grown by molecular beam epitaxy (MBE), is demonstrated by the presence and sharpness of all of the superlattice reflections in its x-ray diffraction pattern (see Figure 3b).^{60,119} Despite the BaTiO_3 layer being just a single unit cell thick (0.4 nm) and well-separated from neighboring BaTiO_3 layers, ultraviolet Raman measurements show that it is still ferroelectric.⁶⁰

The ability to compare theory and experiment has motivated refinements in theory, including attention to not only mechanical (strain) and electrical boundary conditions (whether the ferroelectric is bounded by conducting electrodes or insulating layers), but also to unequal biaxial strain^{115,116} and the ability of a ferroelectric film to break up into multiple domains.^{97,98} For strained-layer superlattices of $\text{BaTiO}_3/\text{SrTiO}_3$, it was shown that quantitative agreement between the predicted and observed T_C for superlattices with a wide range of periodicities only occurred if calculations in which the possibility of multiple domains was considered.^{109,110} For some $\text{BaTiO}_3/\text{SrTiO}_3$ superlattices, such three-dimensional phase-field calculations indicated that the low energy configuration was a multiple-domain state, which allowed the polarization in the $(001)_p$ SrTiO_3 layers to drop considerably when the $(001)_p$ BaTiO_3 layer was thinner than the $(001)_p$ SrTiO_3 layer, resulting in a significant increase in T_C compared to the single-domain state.^{109,110} The domains anticipated to be present by theory, in order to quantitatively explain the observed T_C values, have recently been observed in $\text{BaTiO}_3/\text{SrTiO}_3$ strained-layer superlattices.^{117,118}

Strain engineering of multiferroics

Emboldened by these successes, the strain game has more recently turned to enhancing materials containing multiple ferroic order parameters (i.e., multiferroics such as BiFeO_3) or to create new multiferroics from materials that are on the verge of being ferroic (e.g., EuTiO_3). Illustrative examples are described in the sections that follow.

Strained BiFeO_3 —Morphing a room-temperature multiferroic

Bismuth ferrite, BiFeO_3 , is one of the few materials that is simultaneously ferroelectric and magnetically ordered (antiferromagnetically in the case of BiFeO_3) at room temperature.^{120–124} All of the other room-temperature multiferroics are, however, metastable. These include the high-pressure phase BiCoO_3 ,¹²² strain-stabilized ScFeO_3 with the corundum structure,¹²³ and the hexagonal polymorph of LuFeO_3 that has been stabilized via epitaxy.¹²⁴ In its unstrained state, BiFeO_3 has the highest remnant polarization of any known ferroelectric.^{120,121,125–127} BiFeO_3 also exhibits several polymorphs that are relatively close in energy to each other. Further, in BiFeO_3 , the four fundamental degrees of freedom—electronic

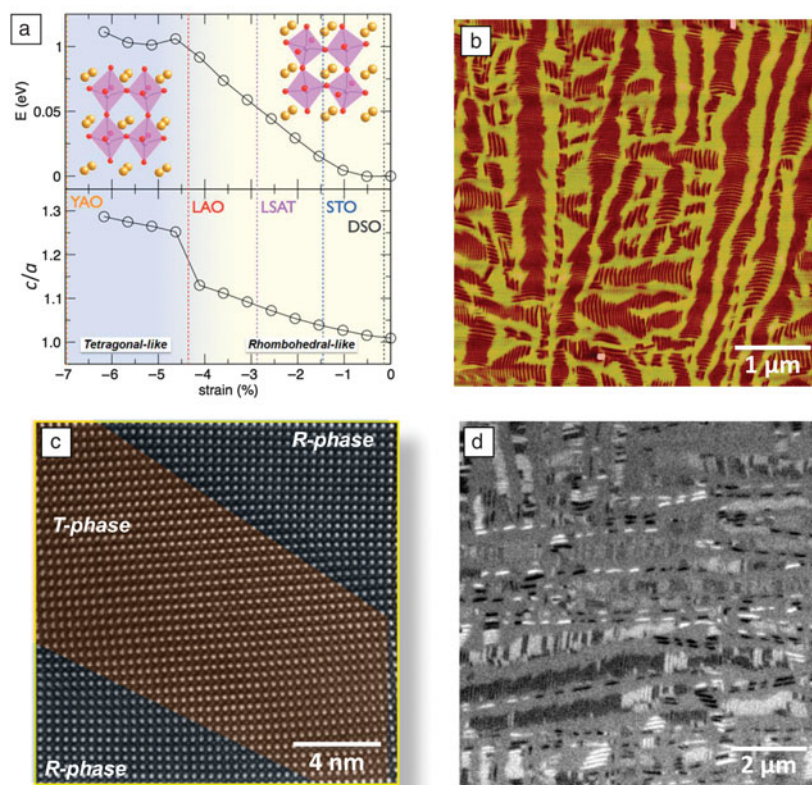


Figure 4. (a) *Ab initio* calculations of the energy and structure (ratio of pseudotetragonal lattice constants c/a) of the ground state of BiFeO_3 as a function of bi-axial, in-plane compressive strain on various substrates: YAO, YAlO_3 ; LAO, LaAlO_3 ; STO, SrTiO_3 ; LSAT, $(\text{LaAlO}_3)_{0.29}-(\text{SrAl}_{1/2}\text{Ta}_{1/2}\text{O}_3)_{0.71}$; DSO, DyScO_3 . (b) Atomic force microscopy image of a partially relaxed, ~ 70 -nm-thick BiFeO_3 film grown on a LaAlO_3 substrate that exhibits a characteristic tetragonal and rhombohedral (T+R) mixed phase nanostructure. (c) High-resolution transmission electron microscopy image of the T+R mixed phase that illustrates the commensurate nature of the interface, with the complete absence of misfit dislocations. (d) X-ray magnetic circular dichroism photoemission electron microscopy (XMCD-PEEM) image obtained using the iron absorption edge showing that the highly constrained R-phase shows enhanced ferromagnetism compared to the bulk or the T-phase. Enhanced magnetic contrast is given from the ratio of PEEM images taken with left and right circularly polarized x-rays at the same location. Black and white contrasts indicate magnetic moments pointing parallel and antiparallel to the incident x-rays. (a) Reprinted with permission from Reference 21. © 2009 AAAS. (b) Adapted from Reference 21. (c) Reprinted with permission from Reference 21. © 2009 AAAS. (d) Reprinted with permission from Reference 134. © 2011 Nature Publishing Group.

spin, charge, orbital, and lattice—are highly interactive. As a consequence, its ground state exhibits a strong sensitivity to temperature, pressure, electric fields, and magnetic fields. These qualities make BiFeO₃ unique and a natural candidate to tweak using the strain game.

Elastic strain, imparted via epitaxy, is able to distort and eventually change the structure and energy of the ground state of BiFeO₃. In its unstrained state, BiFeO₃ is rhombohedral.¹²⁸ The evolution of the structure of BiFeO₃ can be understood from *ab initio* calculations, **Figure 4a**. As an in-plane biaxial compressive strain is imposed via the substrate, the rhombohedral (R) structure becomes progressively monoclinic (and perhaps even triclinic) until a critical strain of ~4.5% is reached. For substrates that impose a larger strain (such as (110) YAlO₃, which imposes a hefty 6.6% biaxial compressive strain on commensurate BiFeO₃ thin films grown upon it^{21–24}), the structure changes into a “super-tetragonal” (T) state (or a monoclinic derivative thereof) with a distinct jump in the ratio of its pseudotetragonal lattice constants *c/a*.²¹ Such an isostructural monoclinic-to-monoclinic phase transition—in which the symmetry does not change, but the coordination chemistry changes dramatically—has also been observed in other materials.^{129–132} The overlapping, roughly parabolic free energy versus strain curves of the R- and T-phases can be seen in **Figure 4a**. It is the change in ground state with strain from the R phase to the T phase that enables the huge (6.6%) biaxial strains to be achieved in BiFeO₃ films. In more typical oxide systems, the free energy versus strain landscape limits the growth of epitaxial perovskite films under common growth conditions to about 3% strain.

Partial relaxation of the epitaxial constraint by increasing the film thickness leads to the formation of a mixed-phase nanostructure that exhibits the coexistence of both the R- and T-phases, as illustrated in the atomic force microscope (AFM) image in **Figure 4b**. This mixed-phase nanostructure is fascinating from many perspectives. First, high-resolution electron microscopy shows that the interface between these two phases is essentially commensurate, **Figure 4c**. This is important because it means that movement of this interface should be possible simply by the application of an electric field, as is indeed the case.¹³³ Second, and perhaps more importantly, the highly distorted R-phase in this ensemble, shows significantly enhanced ferromagnetism. This can be discerned from the x-ray magnetic circular dichroism-photoemission electron microscopy (XMCD-PEEM) image in **Figure 4d**. The R-phase appears in either bright or dark stripe-like contrast in such PEEM images, corresponding to the thin slivers being magnetized either along the x-ray polarization direction or anti-parallel to it.

A rough estimate of the magnetic moment of this highly strained R-phase (from the PEEM images as well as from superconducting quantum interference device magnetometry measurements) gives a local moment of the order of 25–35 emu/cc.¹³⁴ It is noteworthy that the canted moment of the R-phase (~6–8 emu/cc) is not observable by the XMCD technique due to the small magnitude of the moment. This enhanced magnetic moment in the highly strained R-phase

disappears around 150°C.¹³⁴ Application of an electric field converts this mixed (R+T) phase into the T-phase, and the enhanced magnetic moment disappears; reversal of the electric field brings the mixed phase back accompanied by the magnetic moment in the distorted R-phase.¹³⁴

There has been limited work on the tensile side of the BiFeO₃ strain phase diagram. It was, however, predicted, using phase-field calculations, that an orthorhombic (O) phase of BiFeO₃ should exist under sufficient tensile strain,²¹ and recent work has shown that an O-phase can indeed be stabilized.¹³⁵ These observations on biaxially strained BiFeO₃ films raise several questions. First, what is the magnetic ground state of the various strained BiFeO₃ phases (e.g., do they have enhanced canting or exhibit spin glass behavior?). Second, given that spin-orbit coupling is the source of the canted moment in the bulk of BiFeO₃, can this enhanced moment be explained based on the strain and confinement imposed on the R-phase? Finally, what is the state of the Dzyaloshinskii–Moriya vector, the antisymmetric microscopic coupling between two localized magnetic moments, in such a strained system?

Strained EuTiO₃—Transforming a boring dielectric into the world’s strongest ferroelectric ferromagnet

The strain game involving EuTiO₃ is another tale in which theory led the way to a remarkable strain-enabled discovery. The idea behind this new route to ferroelectric ferromagnets is that appropriate magnetically ordered insulators that are neither ferroelectric nor ferromagnetic, of which there are many, can be transmuted into ferroelectric ferromagnets. Fennie and Rabe predicted¹³⁶ that EuTiO₃, a normally boring paraelectric and antiferromagnetic insulator (in its unstrained bulk state), could be transformed using strain into the strongest known multiferroic with a spontaneous polarization and spontaneous magnetization each 100× superior to the reigning multiferroic it displaced, Ni₃B₇O₁₃I.^{137,138}

The physics behind this discovery makes use of spin-lattice coupling as an additional parameter to influence the soft mode of an insulator on the verge of a ferroelectric transition.¹³⁹ The soft mode is the lowest frequency transverse optical phonon, which as it goes to zero results in the phase transition from a paraelectric to a ferroelectric. Appropriate materials for this (1) have a ground state that in the absence of strain is antiferromagnetic and paraelectric, (2) are on the brink of a ferroelectric transition, and (3) exhibit large spin-lattice coupling manifested by a significant decrease in permittivity as the material is cooled through its Néel temperature.¹³⁶ EuTiO₃ meets these criteria and has much in common with SrTiO₃ except that EuTiO₃ magnetically orders at 5 K due to the existence of localized 4*f* moments on the Eu²⁺ site.^{140,141} Similar to SrTiO₃, strain can be used to soften the soft mode and drive it to a ferroelectric instability. In contrast to SrTiO₃, which is diamagnetic, the permittivity of bulk EuTiO₃ is strongly coupled with its magnetism, showing an abrupt decrease in permittivity at the onset of the antiferromagnetic Eu²⁺ ordering.¹⁴² This indicates that the

soft mode frequency hardens when the spins order antiferromagnetically; conversely, it will soften if the spins order ferromagnetically. This extra interaction provides the coupling favoring a simultaneously ferroelectric and ferromagnetic ground state under sufficient strain in EuTiO_3 .

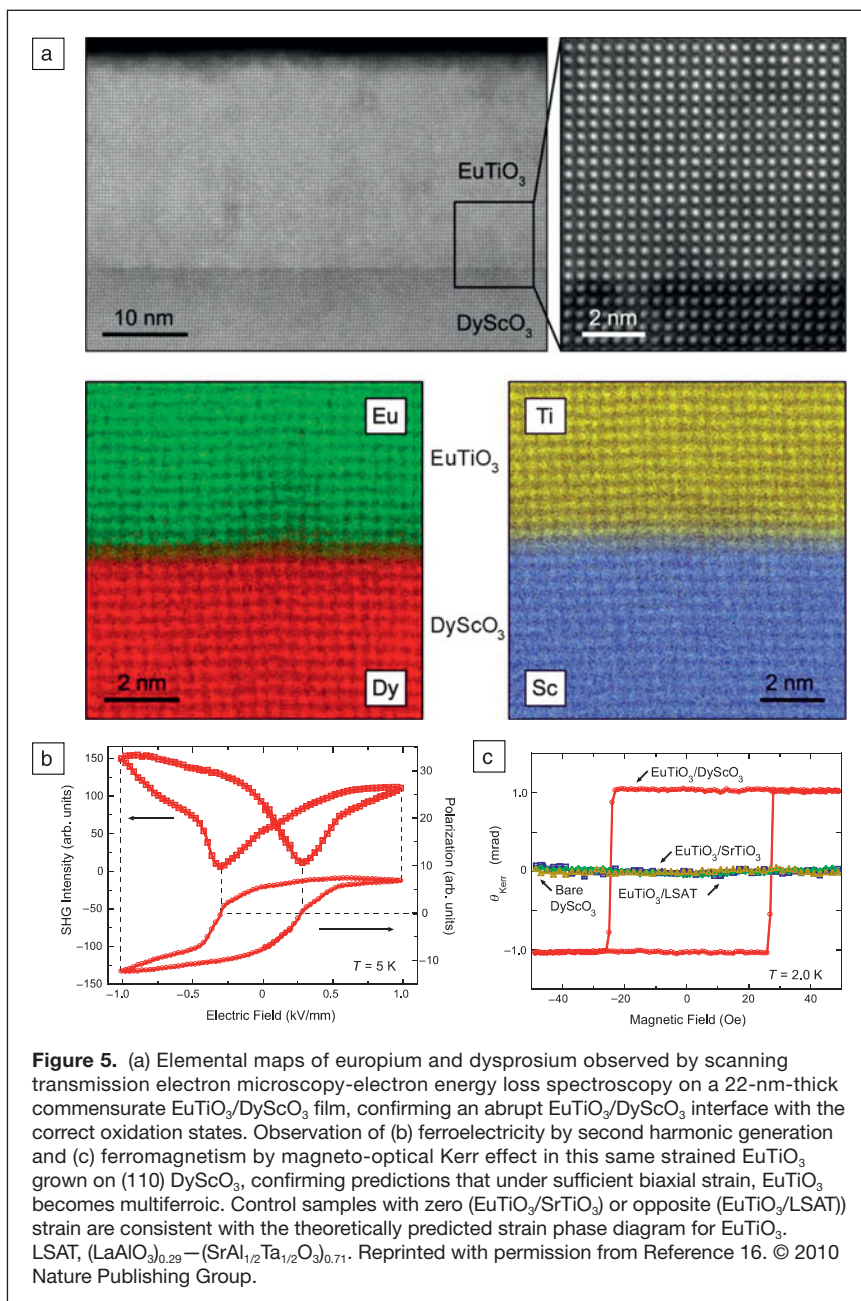
Although testing this prediction seems straightforward, the groups who first tested it ran into an unforeseen complication: no matter what substrate they deposited EuTiO_3 on, it was ferromagnetic. With its identical lattice constant (both are 3.905 Å at room temperature), SrTiO_3 is an obvious substrate for the growth of unstrained epitaxial EuTiO_3 films. Surprisingly, as-grown $\text{EuTiO}_{3-\delta}$ thin films synthesized by pulsed-laser deposition (PLD) on (001) SrTiO_3 substrates exhibit expanded out-of-plane spacings (0.4% to 2% longer than bulk EuTiO_3)^{143–146} and are ferromagnetic with a Curie temperature of about 5 K.^{144,145}

Could the observed expanded lattice spacings in $\text{EuTiO}_{3-\delta}$ thin films be due to oxygen vacancies? The effect of oxygen deficiency on lattice constant has been studied in $\text{EuTiO}_{3-\delta}$ bulk samples down to the $\text{EuTiO}_{2.5}$ limit of the perovskite $\text{EuTiO}_{3-\delta}$ structure, and negligible (<0.5%) variation in the cubic lattice constant was found.^{147,148} Oxygen vacancies alone are thus insufficient to explain the 2% variation in out-of-plane lattice spacings observed in epitaxial $\text{EuTiO}_{3-\delta}$ films grown on (001) SrTiO_3 by PLD.^{144–146}

One possible explanation is that the ferromagnetism observed in epitaxial EuTiO_3 films prepared by PLD on SrTiO_3 arises from extrinsic effects, masking the intrinsic properties of EuTiO_3 thin films. Extrinsic effects are known to occur in thin films, particularly for deposition methods involving energetic species, which can induce defects. Another factor favoring defect introduction is the relatively low growth temperatures common for oxide thin-film growth, enabling defects to be frozen in. For example, some epitaxial SrTiO_3 films grown on SrTiO_3 substrates by PLD have been reported to be ferroelectric,¹⁴⁹ in striking contrast to the intrinsic nature of unstrained SrTiO_3 , which is not ferroelectric at any temperature.¹⁵⁰ Homoepitaxial SrTiO_3 films grown by PLD are also known to exhibit lattice spacings that deviate significantly from the SrTiO_3 substrates they are grown on,^{151–153} although bulk $\text{SrTiO}_{3-\delta}$ (in either single crystal or polycrystalline form) exhibits negligible variation in its cubic lattice constant up to the $\text{SrTiO}_{2.5}$ limit^{154,155} of the perovskite $\text{SrTiO}_{3-\delta}$ structure. The sensitivity of EuTiO_3 that made it an appropriate material to transmute via strain into a multiferroic also makes it quite sensitive to defects.

To overcome this issue and examine the intrinsic effect of strain on EuTiO_3 , a more delicate deposition technique was needed.

In contrast to PLD, homoepitaxial SrTiO_3 films grown by MBE¹⁵⁶ show bulk behavior and none of the unusual effects reported in homoepitaxial SrTiO_3 films grown by PLD.^{149,151–153} Indeed unstrained, stoichiometric EuTiO_3 thin films grown by MBE on (001) SrTiO_3 have the same lattice constant as bulk EuTiO_3 and are antiferromagnetic.¹⁵⁷ Seeing that MBE can produce EuTiO_3 films with intrinsic properties in their unstrained state, MBE was used to test Fennie and Rabe's strained EuTiO_3 predictions.¹³⁶ Commensurate EuTiO_3 films were grown on three substrates: (001) LSAT, (001) SrTiO_3 , and (110) DyScO_3 to impart -0.9% , 0% , and $+1.1\%$ biaxial



strain, respectively. Using scanning transmission electron microscopy with electron energy loss spectroscopy (STEM-EELS), the oxidation state of the film constituents and the abruptness of the interface between the film and substrate was checked with atomic resolution and chemical specificity (**Figure 5a**). Experimental measurements utilizing second harmonic generation (SHG) and magneto-optic Kerr effect (MOKE) confirmed that the EuTiO_3 grown on (110) DyScO_3 was simultaneously ferroelectric (**Figure 5b**) and ferromagnetic (**Figure 5c**), while on the other substrates it was not, in agreement with theory¹³⁶ and resulting in the strongest multiferroic material known today.¹⁶

There are many other exciting predictions that remain to be verified of even stronger and higher temperature ferroelectric ferromagnets in strained SrMnO_3 ¹⁵⁸ and EuO ,¹⁵⁹ as well as the prediction that an electric field on the order of 10^5 V cm^{-1} can be used to turn on ferromagnetism in EuTiO_3 when it is poised on the verge of such a phase transition via strain.¹³⁶ It was recently shown that through the application of an electric field, the antiferromagnetic ground state of EuTiO_3 , strained to be close to where it would have a ferromagnetic ground state (but still on the antiferromagnetic side), can be electrically tuned to the verge of the ferromagnetic state.¹⁶⁰ Turning on magnetism in a material by applying an electric field to it remains an open challenge. Such an important milestone would be a key advance to the field of ferroics, both scientifically and technologically.

Electronics has flourished because of the ability to route voltages with ease and on extremely small scales. If magnetism could be similarly controlled and routed, it would impact memory devices, spin valves, and many other spintronics devices and make numerous hybrid devices possible.

Strained $\text{Sr}_{n+1}\text{Ti}_n\text{O}_{3n+1}$ —Creating a tunable dielectric with record performance

Strain has also been used to create a new family of tunable microwave dielectrics, which due to their low dielectric loss have a figure of merit at room temperature that rivals those of all such known materials.¹⁶¹ In contrast to standard (textbook) dielectrics, whose dielectric displacement (**D**) as a function of applied electric field (**E**) can be described by the linear equation

$$\mathbf{D} = \epsilon_0 \mathbf{K} \mathbf{E}, \quad (1)$$

where ϵ_0 is the permittivity of free space and **K** is the dielectric constant of the material, a tunable dielectric has a highly nonlinear relationship between **D** and **E**. The nonlinearity results in the effective dielectric constant of the material ($\mathbf{D}/\epsilon_0\mathbf{E}$) behaving not as a constant, but changing greatly with **E**; changes of tens of percent in the dielectric “constant” are common in tunable dielectrics at high **E**. This nonlinearity can be described by adding higher order terms to Equation 1. In tensor form, this more general relationship is

$$D_i = \epsilon_0 K_{ij} E_j + \epsilon_{ijk} E_j E_k + \epsilon_{ijkl} E_j E_k E_l + \dots, \quad (2)$$

where ϵ_{ijk} and ϵ_{ijkl} are higher order permittivity coefficients.

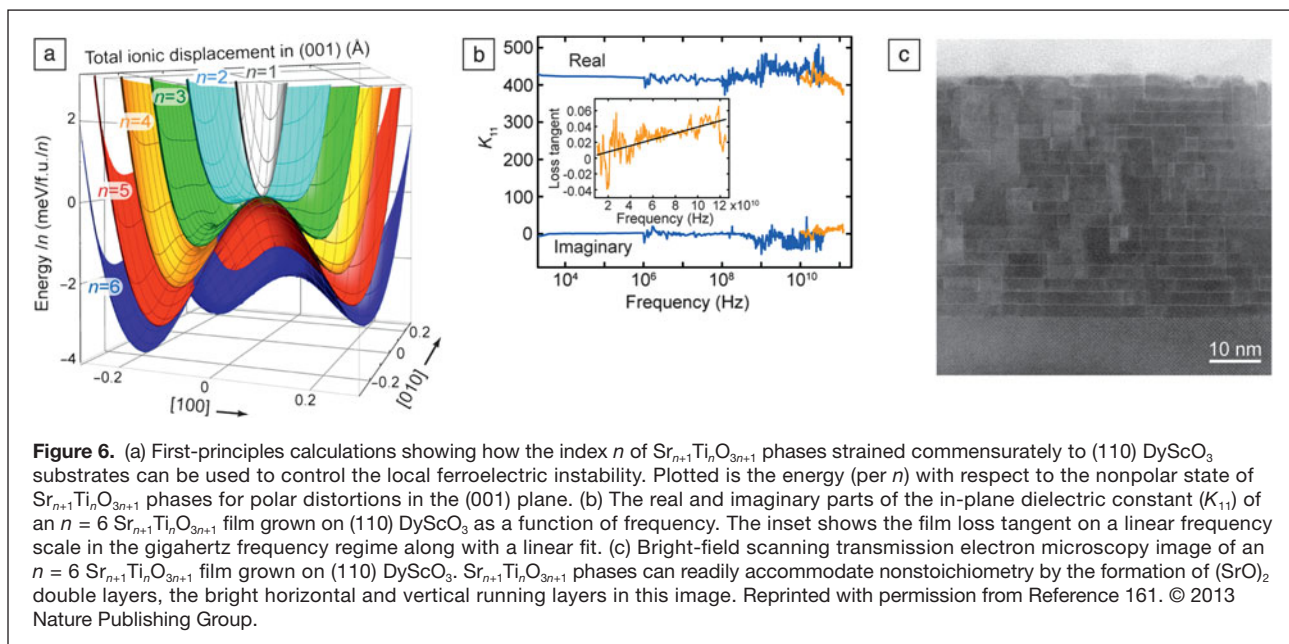
Highly nonlinear dielectrics, including the most extensively studied material with such properties, $\text{Ba}_x\text{Sr}_{1-x}\text{TiO}_3$,^{162–165} are found in displacive ferroelectric systems at temperatures just above the paraelectric-to-ferroelectric transition temperature.^{162,165} These tunable dielectrics are normally used in their paraelectric state to avoid the dielectric losses that would occur in the ferroelectric state due to the motion of domain walls. Although thin films provide an excellent geometry for the application of high **E** at low applied voltages, $\text{Ba}_x\text{Sr}_{1-x}\text{TiO}_3$ films unfortunately suffer significant dielectric losses arising from defects; the dielectric loss in today’s best $\text{Ba}_x\text{Sr}_{1-x}\text{TiO}_3$ tunable dielectrics films at GHz frequencies is about an order of magnitude worse than the best $\text{Ba}_x\text{Sr}_{1-x}\text{TiO}_3$ in bulk form.¹⁶⁵

A new approach to tunable microwave dielectrics is to take a system with exceptionally low loss and introduce a ferroelectric instability into it using strain. The appeal of this approach is that it can be applied to systems that are known to have exceptionally low dielectric loss, particularly in thin-film form. Such systems do not need to have a ferroelectric instability in their unstrained form; strain can be used to help impart the ferroelectric instability. This relaxed design constraint greatly increases the number of eligible systems that could yield improved performance over the best of today’s known tunable dielectrics.

This approach has been applied to $\text{Sr}_{n+1}\text{Ti}_n\text{O}_{3n+1}$ phases—where $(\text{SrO})_2$ crystallographic shear^{166,167} planes provide an alternative to point-defect formation for accommodating nonstoichiometry.^{168,169} These phases are known to have low dielectric loss,^{170,171} even in thin-film form.¹⁷² In their unstrained state, these phases are centrosymmetric, and thus lack a ferroelectric instability.

The strain game in combination with control of the distance between the $(\text{SrO})_2$ planes in $\text{Sr}_{n+1}\text{Ti}_n\text{O}_{3n+1}$ phases can, however, induce a ferroelectric instability.^{161,173} The emergence of this ferroelectric instability in $\text{Sr}_{n+1}\text{Ti}_n\text{O}_{3n+1}$ phases commensurately strained in biaxial tension to (110) DyScO_3 substrates (about 1% biaxial tension) can be seen in **Figure 6a**. For $n \geq 3$, a ferroelectric instability is evident from the double-well energy potential of the ion displacements, and this double-well becomes deeper with increasing n . A deeper well corresponds to the ferroelectric instability occurring at higher temperature until, by $n = 6$, it is just below room temperature.¹⁶¹

The low loss of this tunable dielectric at high frequencies is evident from **Figure 6b**, where both the real and imaginary parts of the in-plane dielectric constant K_{11} are shown over a frequency range spanning more than eight orders of magnitude and up to 125 GHz.¹⁶¹ Only at these highest frequencies can the dielectric loss be seen. This low loss yields unparalleled performance at room temperature for these new tunable dielectrics.¹⁶⁴ The reason for the low dielectric loss, far lower than today’s best $\text{Ba}_x\text{Sr}_{1-x}\text{TiO}_3$ tunable dielectrics at GHz frequencies, is believed to be related to the propensity of $\text{Sr}_{n+1}\text{Ti}_n\text{O}_{3n+1}$ phases to form $(\text{SrO})_2$ planar defects in response to



local stoichiometry deviations rather than point defects.^{168,169} These $(\text{SrO})_2$ double layers show up as bright layers in the STEM image of an $n = 6$ $\text{Sr}_{n+1}\text{Ti}_n\text{O}_{3n+1}$ film in Figure 6c. This is in contrast to the high point-defect concentrations that perovskite films like SrTiO_3 can incorporate in thin-film form,^{75,156} such point defects could be the reason that $\text{Ba}_x\text{Sr}_{1-x}\text{TiO}_3$ tunable dielectric films have significantly higher dielectric losses than bulk $\text{Ba}_x\text{Sr}_{1-x}\text{TiO}_3$.¹⁶⁵

Other ways oxides can react to strain

As the examples described in this article show, the strain game can be a powerful control parameter for enhancing the properties of ferroic oxides. It is important to consider, however, other ways in which a complex oxide might react to strain. Should there be an energetically more favorable route to accommodate the imposed strain, the system might take it. Examples include the possibility that the imposed strain will lead to changes in film composition, microstructure, or crystal structure (e.g., ordering [or disordering] of cations, anions, or their vacancies,^{174,175} atom clustering, the stabilization of other polymorphs, or rotations of the oxygen coordination polyhedra^{176–178}) rather than simply dilating or compressing the spacings between the atoms in the unstrained structure equally. Octahedral rotation patterns from underlying layers and substrates can be imparted into films over distances of several nanometers and can thus complicate a simple biaxial strain picture. An example is the creation of T-phase BiFeO_3 at relatively low biaxial strain (-1.4% , where the BiFeO_3 should be monoclinic), due to the competition between different octahedral rotation patterns in the film and in the substrate.¹⁷⁹ Such chemical and structural changes may also cause dramatic changes in properties, for better or worse, but it is important to distinguish the underlying causes of the changes in properties.

Advances in electron microscopy have been particularly beneficial in identifying these underlying causes (see the Hÿtch and Minor article in this issue). With respect to ferroics, recent advances enabling polarization mapping on the atomic scale,^{180–183} octahedral rotation imaging,¹⁸⁴ and improved STEM-EELS analysis¹⁸⁵ are invaluable in separating true strain effects from changes in composition, structure, and microstructure that can occur to mitigate against a strain effect. These techniques have the potential to visualize closure domains in ferroelectrics,^{182,183} usual domain walls with mixed Bloch–Néel–Ising character in strained ferroelectric superlattices,¹⁸⁶ and the exciting possibility of a dipole-dipole coupling analog of exchange-spring magnets^{187,188} recently predicted to occur in strained ferroelectric systems.¹⁸⁹

Other intriguing predictions, including using strain to poise a material (e.g., SrCoO_3 ¹⁹⁰) on the brink of a metal-insulator transition, which could then be turned on or off through the application of an electric or magnetic field or even a small additional strain, are relevant to emerging piezotronic devices.^{191,192}

Outlook

Elastic strain engineering of ferroics with the perovskite structure has been the most pursued to date. Yet there are many other fascinating oxides that either have a ferroic ground state or are borderline ferroic materials that might be enticed into a ferroic ground state with strain. Such non-perovskite structural families that are relevant include chrysoberyl Cr_2BeO_4 ,¹⁹³ pyrochlore $\text{Ho}_2\text{Ti}_2\text{O}_7$,¹⁹⁴ YMnO_3 ,^{195,196} MnWO_4 ,¹⁹⁷ delafossite CuFeO_2 ,¹⁹⁸ CuO ,¹⁹⁹ and hexaferrite $\text{Sr}_3\text{Co}_2\text{Fe}_{24}\text{O}_{41}$.²⁰⁰ These systems are generally ignored by the thin-film community and have been the focus of the single crystal ferroic community. We believe the issue is the lack of suitable substrates for these latter structures; removing this roadblock would unleash a

huge opportunity in strain engineering for the future. Thin films also have the technological advantage of lower switching voltages and the ability to integrate them into more sophisticated heterostructures, as are relevant for devices.

Imagine the opportunities for strain engineering that substrates for the non-perovskite systems would bring. Substrates for YMnO_3 would enable more variants of hexagonal manganese ferroics to be constructed. These variants include not only known materials, but metastable polymorphs (e.g., LuFeO_3 that is isostructural to YMnO_3 rather than its stable centrosymmetric perovskite form)^{124,201,202} by utilizing lattice misfit strain energies and interfacial energies to favor the desired metastable phase over the equilibrium phase (epitaxial stabilization),^{203–206} or the prospect of interfacial multiferroicity that has been predicted to emerge in superlattices between centrosymmetric components.^{207,208}

Similarly, substrates with the LiNbO_3 structure would enable the growth of the LiNbO_3 -polymorph of FeTiO_3 and related multiferroics.^{209,210} A range of appropriate substrates, like the range of substrates available for perovskites shown in Figure 1d, for each ferroic system of interest would allow the thin-film tricks of strain engineering,^{12–16} epitaxial stabilization,^{203–206} dimensional confinement,^{161,173} polarization engineering,^{112,211} and superlattice formation^{60,103–114,117–119,207,208} to be freely applied to a much larger set of ferroic building blocks. Strain engineering of ferroic oxides is in its infancy and considering its brief, but vibrant past, a brilliant future awaits.

Acknowledgments

We gratefully acknowledge our colleagues and collaborators for sharing their insights and helping us to explore and better understand the exciting area of elastically strained ferroic oxide films. We especially thank the groups of E. Arenholz, M. Bedzyk, M.D. Biegalski, D.H.A. Blank, D.A. Bonnell, J.C. Booth, J.D. Brock, L.E. Cross, C.B. Eom, J.W. Freeland, P. Ghosez, P.C. Hammel, M.E. Hawley, E. Johnston-Halperin, S. Kamba, S.W. Kirchoefer, J. Levy, Yulan Li, T.E. Mallouk, J. Mannhart, L.W. Martin, K. Peters, K.M. Rabe, J.M. Rondinelli, P.J. Ryan, P. Schiffer, J. Schubert, N.A. Spaldin, S.K. Streiffer, A.K. Tagantsev, I. Takeuchi, D.A. Tenne, J.-M. Triscone, S. Trolier-McKinstry, D. Vanderbilt, J.C. Woicik, and X.X. Xi. L.Q.C., C.J.F., V.G., X.Q.P., D.G.S., and R.R. gratefully acknowledge financial support from the National Science Foundation (NSF) under Grant No. DMR-0820404. D.G.S. also acknowledges NSF Grant DMR-0948036. R.R. acknowledges sustained support from the US Department of Energy under Contract No. DE-AC0205CH11231.

References

1. A.E. Lindh, in *Nobel Lectures in Physics 1942–1962* (World Scientific, Singapore, 1998), pp. 49–52.
2. J.M. Lock, *Philos. Trans. R. Soc. London, Ser. A* **208**, 391 (1951).
3. P.W. Forsbergh Jr., *Phys. Rev.* **93**, 686 (1954).
4. L.D. Nguyen, A.S. Brown, M.A. Thompson, L.M. Jelloian, *IEEE Trans. Electron Devices* **39**, 2007 (1992).
5. J. Welser, J.L. Hoyt, J.F. Gibbons, *IEEE Electron Device Lett.* **15**, 100 (1994).
6. W. Shockley, J. Bardeen, *Phys. Rev.* **77**, 407 (1950).

7. H. Sato, M. Naito, *Physica C* **274**, 221 (1997).
8. I. Bozovic, G. Logvenov, I. Belca, B. Narimbetov, I. Sveklo, *Phys. Rev. Lett.* **89**, 107001 (2002).
9. R.S. Beach, J.A. Borchers, A. Matheny, R.W. Erwin, M.B. Salamon, B. Everitt, K. Pettit, J.J. Rhyne, C.P. Flynn, *Phys. Rev. Lett.* **70**, 3502 (1993).
10. Q. Gan, R.A. Rao, C.B. Eom, J.L. Garrett, M. Lee, *Appl. Phys. Lett.* **72**, 978 (1998).
11. D. Fuchs, E. Arac, C. Pinta, S. Schuppler, R. Schneider, H.v. Löhneysen, *Phys. Rev. B* **77**, 014434 (2008).
12. J.H. Haeni, P. Irvin, W. Chang, R. Uecker, P. Reiche, Y.L. Li, S. Choudhury, W. Tian, M.E. Hawley, B. Craigo, A.K. Tagantsev, X.Q. Pan, S.K. Streiffer, L.Q. Chen, S.W. Kirchoefer, J. Levy, D.G. Schlom, *Nature* **430**, 758 (2004).
13. K.J. Choi, M.D. Biegalski, Y.L. Li, A. Sharan, J. Schubert, R. Uecker, P. Reiche, Y.B. Chen, X.Q. Pan, V. Gopalan, L.-Q. Chen, D.G. Schlom, C.B. Eom, *Science* **306**, 1005 (2004).
14. D.G. Schlom, L.Q. Chen, C.B. Eom, K.M. Rabe, S.K. Streiffer, J.-M. Triscone, *Annu. Rev. Mater. Res.* **37**, 589 (2007).
15. M.P. Warusawithana, C. Cen, C.R. Slesman, J.C. Woicik, Y.L. Li, L.F. Kourkoutis, J.A. Klug, H. Li, P. Ryan, L.-P. Wang, M. Bedzyk, D.A. Muller, L.Q. Chen, J. Levy, D.G. Schlom, *Science* **324**, 367 (2009).
16. J.H. Lee, L. Fang, E. Vlahos, X. Ke, Y.W. Jung, L.F. Kourkoutis, J.-W. Kim, P.J. Ryan, T. Heeg, M. Roeckerath, V. Goian, M. Bernhagen, R. Uecker, P.C. Hammel, K.M. Rabe, S. Kamba, J. Schubert, J.W. Freeland, D.A. Muller, C.J. Fennie, P. Schiffer, V. Gopalan, E. Johnston-Halperin, D.G. Schlom, *Nature* **466**, 954 (2010).
17. C. Adamo, X. Ke, H.Q. Wang, H.L. Xin, T. Heeg, M.E. Hawley, W. Zander, J. Schubert, P. Schiffer, D.A. Muller, L. Maritato, D.G. Schlom, *Appl. Phys. Lett.* **95**, 112504 (2009).
18. H. Béa, B. Dupé, S. Fusil, R. Mattana, E. Jacquet, B. Warot-Fonrose, F. Wilhelm, A. Rogalev, S. Petit, V. Cros, A. Anane, F. Petroff, K. Bouzehouane, G. Geneste, B. Dkhil, S. Lisenkov, I. Ponomareva, L. Bellaiche, M. Bibes, A. Barthélémy, *Phys. Rev. Lett.* **102**, 217603 (2009).
19. I.C. Infante, S. Lisenkov, B. Dupé, M. Bibes, S. Fusil, E. Jacquet, G. Geneste, S. Petit, A. Courtial, J. Juraszek, L. Bellaiche, A. Barthélémy, B. Dkhil, *Phys. Rev. Lett.* **105**, 057601 (2010).
20. Z. Chen, Z. Luo, C. Huang, Y. Qi, P. Yang, L. You, C. Hu, T. Wu, J. Wang, C. Gao, T. Sritharan, L. Chen, *Adv. Funct. Mater.* **21**, 133 (2011).
21. R.J. Zeches, M.D. Rossell, J.X. Zhang, A.J. Hatt, Q. He, C.-H. Yang, A. Kumar, C.H. Wang, A. Melville, C. Adamo, G. Sheng, Y.-H. Chu, J.F. Ihlefeld, R. Erni, C. Ederer, V. Gopalan, L.Q. Chen, D.G. Schlom, N.A. Spaldin, L.W. Martin, R. Ramesh, *Science* **326**, 977 (2009).
22. P. Chen, N.J. Podraza, X.S. Xu, A. Melville, E. Vlahos, V. Gopalan, R. Ramesh, D.G. Schlom, J.L. Musfeldt, *Appl. Phys. Lett.* **96**, 131907 (2010).
23. H.M. Christen, J.H. Nam, H.S. Kim, A.J. Hatt, N.A. Spaldin, *Phys. Rev. B* **83**, 144107 (2011).
24. L.W. Martin, D.G. Schlom, *Curr. Opin. Solid State Mater. Sci.* **16**, 199 (2012).
25. A.A. Griffith, *Philos. Trans. R. Soc. London, Ser. A* **221**, 163 (1920).
26. E. Klokholm, J.W. Matthews, A.F. Mayadas, J. Angilello, in *Magnetism and Magnetic Materials*, C.D. Graham Jr., J.J. Rhyne, Eds. (American Institute of Physics, New York, 1972), pp. 105–109.
27. L.B. Freund, S. Suresh, *Thin Film Materials: Stress, Defect Formation and Surface Evolution* (Cambridge University Press, Cambridge, 2003), pp. 60–83, 283–290, 396–416.
28. N.A. Pertsev, A.K. Tagantsev, N. Setter, *Phys. Rev. B* **61**, R825 (2000).
29. N.A. Pertsev, A.K. Tagantsev, N. Setter, *Phys. Rev. B* **65**, 219901 (2002).
30. A.F. Devonshire, *Philos. Mag.* **3** (Suppl.), 85 (1954).
31. A. Antons, J.B. Neaton, K.M. Rabe, D. Vanderbilt, *Phys. Rev. B* **71**, 024102 (2005).
32. Y.L. Li, S. Choudhury, J.H. Haeni, M.D. Biegalski, A. Vasudevarao, A. Sharan, H.Z. Ma, J. Levy, V. Gopalan, S. Trolier-McKinstry, D.G. Schlom, Q.X. Jia, L.Q. Chen, *Phys. Rev. B* **73**, 184112 (2006).
33. C.L. Canedy, H. Li, S.P. Alpay, L. Salamanca-Riba, A.L. Roytburd, R. Ramesh, *Appl. Phys. Lett.* **77**, 1695 (2000).
34. I.B. Misirlioglu, A.L. Vasiliev, M. Aindow, S.P. Alpay, R. Ramesh, *Appl. Phys. Lett.* **84**, 1742 (2004).
35. M.-W. Chu, I. Szafrański, R. Scholz, C. Harnagea, D. Hesse, M. Alexe, U. Gösele, *Nature Mater.* **3**, 87 (2004).
36. S.P. Alpay, I.B. Misirlioglu, V. Nagarajan, R. Ramesh, *Appl. Phys. Lett.* **85**, 2044 (2004).
37. V. Nagarajan, C.L. Jia, H. Kohlstedt, R. Waser, I.B. Misirlioglu, S.P. Alpay, R. Ramesh, *Appl. Phys. Lett.* **86**, 192910 (2005).
38. M.D. Biegalski, D.D. Fong, J.A. Eastman, P.H. Fuoss, S.K. Streiffer, T. Heeg, J. Schubert, W. Tian, C.T. Nelson, X.Q. Pan, M.E. Hawley, M. Bernhagen, P. Reiche, R. Uecker, S. Trolier-McKinstry, D.G. Schlom, *J. Appl. Phys.* **104**, 114109 (2008).
39. R. Uecker, H. Wilke, D.G. Schlom, B. Velickov, P. Reiche, A. Polity, M. Bernhagen, M. Rossberg, *J. Cryst. Growth* **295**, 84 (2006).

40. R. Uecker, B. Velickov, D. Klimm, R. Bertram, M. Bernhagen, M. Rabe, M. Albrecht, R. Fornari, D.G. Schlom, *J. Cryst. Growth* **310**, 2649 (2008).
41. R. Uecker, D. Klimm, R. Bertram, M. Bernhagen, I. Schulze-Jonack, M. Brützmam, A. Kwasniewski, T.M. Gesing, D.G. Schlom, *Acta Phys. Pol. A* **124**, 295 (2013).
42. A. Lempicki, M.H. Randles, D. Wisniewski, M. Balcerzyk, C. Brecher, A.J. Wojtowicz, *IEEE Trans. Nucl. Sci.* **42**, 280 (1995).
43. A.G. Petrosyan, G.O. Shirinyan, C. Pedrini, C. Durjardin, K.L. Ovanesyan, R.G. Manucharyan, T.I. Butaeva, M.V. Derzyan, *Cryst. Res. Technol.* **33**, 241 (1998).
44. H. Asano, S. Kubo, O. Michikami, M. Satoh, T. Konaka, *Jpn. J. Appl. Phys., Part 2* **29**, L1452 (1990).
45. R. Brown, V. Pendrick, D. Kalokitis, B.H.T. Chai, *Appl. Phys. Lett.* **57**, 1351 (1990).
46. Y. Miyazawa, H. Tushima, S. Morita, *J. Cryst. Growth* **128**, 668 (1993).
47. G.W. Berkstresser, A.J. Valentino, C.D. Brandle, *J. Cryst. Growth* **109**, 467 (1991).
48. G.W. Berkstresser, A.J. Valentino, C.D. Brandle, *J. Cryst. Growth* **128**, 684 (1993).
49. S. Hontsu, J. Ishii, T. Kawai, S. Kawai, *Appl. Phys. Lett.* **59**, 2886 (1991).
50. D. Mateika, H. Kohler, H. Laudan, E. Volkel, *J. Cryst. Growth* **109**, 447 (1991).
51. R.W. Simon, C.E. Platt, A.E. Lee, G.S. Lee, K.P. Daly, M.S. Wire, J.A. Luine, M. Urbanik, *Appl. Phys. Lett.* **53**, 2677 (1988).
52. G.W. Berkstresser, A.J. Valentino, C.D. Brandle, *J. Cryst. Growth* **109**, 457 (1991).
53. B.C. Chakoumakos, D.G. Schlom, M. Urbanik, J. Luine, *J. Appl. Phys.* **83**, 1979 (1998).
54. R.L. Sandstrom, E.A. Giess, W.J. Gallagher, A. Segmüller, E.I. Cooper, M.F. Chisholm, A. Gupta, S. Shinde, R.B. Laibowitz, *Appl. Phys. Lett.* **53**, 1874 (1988).
55. L. Merker, US Patent No. 2,684,910 (27 July 1954).
56. J.G. Bednorz, H.J. Scheel, *J. Cryst. Growth* **41**, 5 (1977).
57. P.I. Nabokin, D. Souptel, A.M. Balbashov, *J. Cryst. Growth* **250**, 397 (2003).
58. H.J. Scheel, J.G. Bednorz, P. Dill, *Ferroelectrics* **13**, 507 (1976).
59. S.-G. Lim, S. Kriventsov, T.N. Jackson, J.H. Haeni, D.G. Schlom, A.M. Balbashov, R. Uecker, P. Reiche, J.L. Freeouf, G. Lucovsky, *J. Appl. Phys.* **91**, 4500 (2002).
60. A. Soukiassian, W. Tian, V. Vaithyanathan, J.H. Haeni, L.Q. Chen, X.X. Xi, D.G. Schlom, D.A. Tenne, H.P. Sun, X.Q. Pan, K.J. Choi, C.B. Eom, Y.L. Li, Q.X. Jia, C. Constantin, R.M. Feenstra, M. Bernhagen, P. Reiche, R. Uecker, *J. Mater. Res.* **23**, 1417 (2008).
61. R. Feenstra, L.A. Boatner, J.D. Budai, D.K. Christen, M.D. Galloway, D.B. Poker, *Appl. Phys. Lett.* **54**, 1063 (1989).
62. J.C. Yang, Q. He, S.J. Suresha, C.Y. Kuo, C.Y. Peng, R.C. Haislmaier, M.A. Motyka, G. Sheng, C. Adamo, H.J. Lin, Z. Hu, L. Chang, L.H. Tjeng, E. Arenholz, N.J. Podraza, M. Bernhagen, R. Uecker, D.G. Schlom, V. Gopalan, L.Q. Chen, C.T. Chen, R. Ramesh, Y.H. Chu, *Phys. Rev. Lett.* **109**, 247606 (2012).
63. S. Coh, T. Heeg, J.H. Haeni, M.D. Biegalski, J. Lettieri, L.F. Edge, K.E. O'Brien, M. Bernhagen, P. Reiche, R. Uecker, S. Trolier-McKinstry, D.G. Schlom, D. Vanderbilt, *Phys. Rev. B* **82**, 064101 (2010).
64. K.L. Ovanesyan, A.G. Petrosyan, G.O. Shirinyan, C. Pedrini, L. Zhang, *J. Cryst. Growth* **198**, 497 (1999).
65. M.D. Biegalski, Y. Jia, D.G. Schlom, S. Trolier-McKinstry, S.K. Streiffer, V. Sherman, R. Uecker, P. Reiche, *Appl. Phys. Lett.* **88**, 192907 (2006).
66. J.F. Ihlefeld, W. Tian, Z.-K. Liu, W.A. Doolittle, M. Bernhagen, P. Reiche, R. Uecker, R. Ramesh, D.G. Schlom, *IEEE Trans. Ultrason. Ferroelectr. Freq. Control* **56**, 1528 (2009).
67. J.H. Lee, X. Ke, R. Misra, J.F. Ihlefeld, X.S. Xu, Z.G. Mei, T. Heeg, M. Roedererath, J. Schubert, Z.K. Liu, J.L. Musfeldt, P. Schiffer, D.G. Schlom, *Appl. Phys. Lett.* **96**, 262905 (2010).
68. P. Irvin, J. Levy, J.H. Haeni, D.G. Schlom, *Appl. Phys. Lett.* **88**, 042902 (2006).
69. H.Z. Ma, J. Levy, M.D. Biegalski, S. Trolier-McKinstry, D.G. Schlom, *J. Appl. Phys.* **105**, 014102 (2009).
70. A. Vasudevarao, A. Kumar, L. Tian, J.H. Haeni, Y.L. Li, C.-J. Klund, Q.X. Jia, R. Uecker, P. Reiche, K.M. Rabe, L.Q. Chen, D.G. Schlom, V. Gopalan, *Phys. Rev. Lett.* **97**, 257602 (2006).
71. A. Vasudevarao, S. Denev, M.D. Biegalski, Y.L. Li, L.Q. Chen, S. Trolier-McKinstry, D.G. Schlom, V. Gopalan, *Appl. Phys. Lett.* **92**, 192902 (2008).
72. S. Denev, A. Kumar, M.D. Biegalski, H.W. Jang, C.M. Folkman, A. Vasudevarao, Y. Han, I.M. Reaney, S. Trolier-McKinstry, C.B. Eom, D.G. Schlom, V. Gopalan, *Phys. Rev. Lett.* **100**, 257601 (2008).
73. M.D. Biegalski, E. Vlahos, G. Sheng, Y.L. Li, M. Bernhagen, P. Reiche, R. Uecker, S.K. Streiffer, L.Q. Chen, V. Gopalan, D.G. Schlom, S. Trolier-McKinstry, *Phys. Rev. B* **79**, 224117 (2009).
74. D. Nuzhnyy, J. Peltzelt, S. Kamba, P. Kužel, C. Kadlec, V. Bovtun, M. Kempa, J. Schubert, C.M. Brooks, D.G. Schlom, *Appl. Phys. Lett.* **95**, 232902 (2009).
75. C.H. Lee, V. Skoromets, M.D. Biegalski, S. Lei, R. Haislmaier, M. Bernhagen, R. Uecker, X.X. Xi, V. Gopalan, X. Martí, S. Kamba, P. Kužel, D.G. Schlom, *Appl. Phys. Lett.* **102**, 082905 (2013).
76. K.J. Hubbard, D.G. Schlom, *J. Mater. Res.* **11**, 2757 (1996).
77. D.G. Schlom, S. Guha, S. Datta, *MRS Bull.* **33**, 1017 (2008).
78. L.F. Kourkoutis, C.S. Hellberg, V. Vaithyanathan, H. Li, M.K. Parker, K.E. Andersen, D.G. Schlom, D.A. Muller, *Phys. Rev. Lett.* **100**, 036101 (2008).
79. H. Li, X. Hu, Y. Wei, Z. Yu, X. Zhang, R. Droopad, A.A. Demkov, J. Edwards, K. Moore, W. Ooms, J. Kulik, P. Fejes, *J. Appl. Phys.* **93**, 4521 (2003).
80. M. Kawasaki, K. Takahashi, T. Maeda, R. Tsuchiya, M. Shinohara, O. Ishiyama, T. Yonezawa, M. Yoshimoto, H. Koinuma, *Science* **266**, 1540 (1994).
81. G. Koster, B.L. Kropman, G.J.H.M. Rijnders, D.H.A. Blank, H. Rogalla, *Appl. Phys. Lett.* **73**, 2920 (1998).
82. A.G. Schrott, J.A. Misewich, M. Copel, D.W. Abraham, Y. Zhang, *Appl. Phys. Lett.* **79**, 1786 (2001).
83. A. Biswas, P.B. Rossen, C.H. Yang, W. Siemons, M.H. Jung, I.K. Yang, R. Ramesh, Y.H. Jeong, *Appl. Phys. Lett.* **98**, 051904 (2011).
84. J. Chang, Y.-S. Park, S.-K. Kim, *Appl. Phys. Lett.* **92**, 152910 (2008).
85. J.L. Blok, X. Wan, G. Koster, D.H.A. Blank, G. Rijnders, *Appl. Phys. Lett.* **99**, 151917 (2011).
86. T. Ohnishi, K. Takahashi, M. Nakamura, M. Kawasaki, M. Yoshimoto, H. Koinuma, *Appl. Phys. Lett.* **74**, 2531 (1999).
87. J.H. Ngai, T.C. Schwendemann, A.E. Walker, Y. Segal, F.J. Walker, E.I. Altman, C.H. Ahn, *Adv. Mater.* **22**, 2945 (2010).
88. J.E. Kleibecker, G. Koster, W. Siemons, D. Dubbink, B. Kuiper, J.L. Blok, C.-H. Yang, J. Ravichandran, R. Ramesh, J.E. ten Elshof, D.H.A. Blank, G. Rijnders, *Adv. Funct. Mater.* **20**, 3490 (2010).
89. J.E. Kleibecker, B. Kuiper, S. Harkema, D.H.A. Blank, G. Koster, G. Rijnders, P. Tinnemans, E. Vlieg, P.B. Rossen, W. Siemons, G. Portale, J. Ravichandran, J.M. Szeplieniec, R. Ramesh, *Phys. Rev. B* **85**, 165413 (2012).
90. H.-J. Bae, J. Sigman, D.P. Norton, L.A. Boatner, *Appl. Surf. Sci.* **241**, 271 (2005).
91. N.A. Pertsev, A.G. Zembilgotov, A.K. Tagantsev, *Phys. Rev. Lett.* **80**, 1988 (1998).
92. O. Diéguez, S. Tinte, A. Antons, C. Bungaro, J.B. Neaton, K.M. Rabe, D. Vanderbilt, *Phys. Rev. B* **69**, 212101 (2004).
93. Y.L. Li, L.Q. Chen, *Appl. Phys. Lett.* **88**, 072905 (2006).
94. D.A. Tenne, P. Turner, J.D. Schmidt, M. Biegalski, Y.L. Li, L.Q. Chen, A. Soukiassian, S. Trolier-McKinstry, D.G. Schlom, X.X. Xi, D.D. Fong, P.H. Fuoss, J.A. Eastman, G.B. Stephenson, C. Thompson, S.K. Streiffer, *Phys. Rev. Lett.* **103**, 177601 (2009).
95. A. Pertsev, V.G. Koukhar, *Phys. Rev. Lett.* **84**, 3722 (2000).
96. V.G. Koukhar, N.A. Pertsev, R. Waser, *Phys. Rev. B* **64**, 214103 (2001).
97. Y.L. Li, S.Y. Hu, Z.K. Liu, L.Q. Chen, *Appl. Phys. Lett.* **78**, 3878 (2001).
98. Y.L. Li, S.Y. Hu, Z.K. Liu, L.Q. Chen, *Acta Mater.* **50**, 395 (2002).
99. S.K. Streiffer, J.A. Eastman, D.D. Fong, C. Thompson, A. Munkholm, M.V.R. Murty, O. Auciello, G.R. Bai, G.B. Stephenson, *Phys. Rev. Lett.* **89**, 067601 (2002).
100. D.D. Fong, G.B. Stephenson, S.K. Streiffer, J.A. Eastman, O. Auciello, P.H. Fuoss, C. Thompson, *Science* **304**, 1650 (2004).
101. K. Abe, N. Yanase, K. Sano, M. Izuha, N. Fukushima, T. Kawakubo, *Integr. Ferroelectr.* **21**, 197 (1998).
102. N. Yanase, K. Abe, N. Fukushima, T. Kawakubo, *Jpn. J. Appl. Phys., Part 1* **38**, 5305 (1999).
103. E.D. Specht, H.-M. Christen, D.P. Norton, L.A. Boatner, *Phys. Rev. Lett.* **80**, 4317 (1998).
104. H.-M. Christen, L.A. Krauss, K.S. Harshavardhan, *Mater. Sci. Eng., B* **56**, 200 (1998).
105. H.-M. Christen, E.D. Specht, S.S. Silliman, K.S. Harshavardhan, *Phys. Rev. B* **68**, 20101 (2003).
106. M. Dawber, C. Lichtensteiger, M. Cantoni, M. Veithen, P. Ghosez, K. Johnston, K.M. Rabe, J.-M. Triscone, *Phys. Rev. Lett.* **95**, 177601 (2005).
107. E. Bousquet, M. Dawber, N. Stucki, C. Lichtensteiger, P. Hermet, S. Gariglio, J.M. Triscone, P. Ghosez, *Nature* **452**, 732 (2008).
108. J.B. Neaton, K.M. Rabe, *Appl. Phys. Lett.* **82**, 1586 (2003).
109. D.A. Tenne, A. Bruchhausen, N.D. Lanzillotti-Kimura, A. Fainstein, R.S. Katiyar, A. Cantarero, A. Soukiassian, V. Vaithyanathan, J.H. Haeni, W. Tian, D.G. Schlom, K.J. Choi, D.M. Kim, C.B. Eom, H.P. Sun, X.Q. Pan, Y.L. Li, L.Q. Chen, Q.X. Jia, S.M. Nakhmanson, K.M. Rabe, X.X. Xi, *Science* **313**, 1614 (2006).
110. Y.L. Li, S.Y. Hu, D. Tenne, A. Soukiassian, D.G. Schlom, X.X. Xi, K.J. Choi, C.B. Eom, A. Saxena, T. Lookman, Q.X. Jia, L.Q. Chen, *Appl. Phys. Lett.* **91**, 112914 (2007).
111. Y.L. Li, S.Y. Hu, D. Tenne, A. Soukiassian, D.G. Schlom, L.Q. Chen, X.X. Xi, K.J. Choi, C.B. Eom, A. Saxena, T. Lookman, Q.X. Jia, *Appl. Phys. Lett.* **91**, 252904 (2007).
112. N. Sai, B. Meyer, D. Vanderbilt, *Phys. Rev. Lett.* **84**, 5636 (2000).
113. M.R. Warusawithana, E.V. Colla, J.N. Eckstein, M.B. Weissman, *Phys. Rev. Lett.* **90**, 036802 (2003).
114. H.N. Lee, H.M. Christen, M.F. Chisholm, C.M. Rouleau, D.H. Lowndes, *Nature* **433**, 395 (2005).
115. A.G. Zembilgotov, N.A. Pertsev, U. Böttger, R. Waser, *Appl. Phys. Lett.* **86**, 052903 (2005).

116. G. Sheng, Y.L. Li, J.X. Zhang, S. Choudhury, Q.X. Jia, V. Gopalan, D.G. Schlom, Z.K. Liu, L.Q. Chen, *J. Appl. Phys.* **108**, 084113 (2010).
117. K. Kathan-Galipeau, P.P. Wu, Y.L. Li, L.Q. Chen, A. Soukiassian, X.X. Xi, D.G. Schlom, D.A. Bonnelli, *ACS Nano* **5**, 640 (2011).
118. K. Kathan-Galipeau, P.P. Wu, Y.L. Li, L.Q. Chen, A. Soukiassian, Y. Zhu, D.A. Muller, X.X. Xi, D.G. Schlom, D.A. Bonnelli, *J. Appl. Phys.* **112**, 052011 (2012).
119. J. Ravichandran, A.K. Yadav, R. Cheaito, P.B. Rossen, A. Soukiassian, S.J. Suresha, J.C. Duda, B.M. Foley, C.H. Lee, Y. Zhu, A.W. Lichtenberger, J.E. Moore, D.A. Muller, D.G. Schlom, P.E. Hopkins, A. Majumdar, R. Ramesh, M.A. Zurbuchen, *Nat. Mater.* (2013), in press, doi: 10.1038/nmat3826.
120. J. Wang, J.B. Neaton, H. Zheng, V. Nagarajan, S.B. Ogale, B. Liu, D. Viehland, V. Vaithyanathan, D.G. Schlom, U.V. Waghmare, N.A. Spaldin, K.M. Rabe, M. Wuttig, R. Ramesh, *Science* **299**, 1719 (2003).
121. R. Ramesh, N.A. Spaldin, *Nat. Mater.* **6**, 21 (2007).
122. A.A. Belik, S. Iikubo, K. Kodama, N. Igawa, S.-I. Shamoto, S. Niitaka, M. Azuma, Y. Shimakawa, M. Takano, F. Izumi, E. Takayama-Muromachi, *Chem. Mater.* **18**, 798 (2006).
123. M.-R. Li, U. Adem, S.R.C. McMitchell, Z. Xu, C.I. Thomas, J.E. Warren, D.V. Giap, H. Niu, X. Wan, R.G. Palgrave, F. Schiffrmann, F. Cora, B. Slater, T.L. Burnett, M.G. Cain, A.M. Abakumov, G. van Tendeloo, M.F. Thomas, M.J. Rosseinsky, J.B. Claridge, *J. Am. Chem. Soc.* **134**, 3737 (2012).
124. W. Wang, J. Zhao, W. Wang, Z. Gai, N. Balke, M. Chi, H.N. Lee, W. Tian, L. Zhu, X. Cheng, D.J. Keavney, J. Yi, T.Z. Ward, P.C. Snijders, H.M. Christen, W. Wu, J. Shen, X. Xu, *Phys. Rev. Lett.* **110**, 237601 (2013).
125. J.F. Li, J. Wang, M. Wuttig, R. Ramesh, N. Wang, B. Ruetter, A.P. Pyatakov, A.K. Zvezdin, D. Viehland, *Appl. Phys. Lett.* **84**, 5261 (2004).
126. R.R. Das, D.M. Kim, S.H. Baek, C.B. Eom, F. Zavaliche, S.Y. Yang, R. Ramesh, Y.B. Chen, X.Q. Pan, X. Ke, M.S. Rzchowski, S.K. Streiffer, *Appl. Phys. Lett.* **88**, 242904 (2006).
127. J. Dho, X. Qi, H. Kim, J.L. MacManus-Driscoll, M.G. Blamire, *Adv. Mater.* **18**, 1445 (2006).
128. F. Kubel, H. Schmid, *Acta Crystallogr., Sect. B: Struct. Sci.* **46**, 698 (1990).
129. A.J. Hatt, N.A. Spaldin, C. Ederer, *Phys. Rev. B* **81**, 054109 (2010).
130. A.G. Christy, *Acta Crystallogr. Sect. B: Struct. Sci.* **51**, 753 (1995).
131. L. Ehm, K. Knorr, L. Peters, S. Rath, W. Depmeier, *J. Alloys Compd.* **429**, 82 (2007).
132. J. Haines, J.M. Léger, O. Schulte, *Phys. Rev. B* **57**, 7551 (1998).
133. J.X. Zhang, B. Xiang, Q. He, J. Seidel, R.J. Zeches, P. Yu, S.Y. Yang, C.H. Wang, Y.H. Chu, L.W. Martin, A.M. Minor, R. Ramesh, *Nat. Nanotechnol.* **6**, 98 (2011).
134. Q. He, Y.H. Chu, J.T. Heron, S.Y. Yang, W.I. Liang, C.Y. Kuo, H.J. Lin, P. Yu, C.W. Liang, R.J. Zeches, W.C. Kuo, J.Y. Juang, C.T. Chen, E. Arenholz, A. Scholl, R. Ramesh, *Nat. Commun.* **2**, 225 (2011).
135. J.C. Yang, Q. He, S.J. Suresha, C.Y. Kuo, C.Y. Peng, R.C. Haislmaier, M.A. Motyka, G. Sheng, C. Adamo, H.J. Lin, Z. Hu, L. Chang, L.H. Tjeng, E. Arenholz, N.J. Podraza, M. Bernhagen, R. Uecker, D.G. Schlom, V. Gopalan, L.Q. Chen, C.T. Chen, R. Ramesh, Y.H. Chu, *Phys. Rev. Lett.* **109**, 247606 (2012).
136. C.J. Fennie, K.M. Rabe, *Phys. Rev. Lett.* **97**, 267602 (2006).
137. J.P. Rivera, H. Schmid, *Ferroelectrics* **36**, 447 (1981).
138. W. von Wartburg, *Phys. Status Solidi A* **21**, 557 (1974).
139. T. Birol, C.J. Fennie, *Phys. Rev. B* **88**, 094103 (2013).
140. T.R. McGuire, M.W. Shafer, R.J. Joenk, H.A. Alperin, S.J. Pickart, *J. Appl. Phys.* **37**, 981 (1966).
141. C.-L. Chien, S. DeBenedetti, F. De S. Barros, *Phys. Rev. B* **10**, 3913 (1974).
142. T. Katsufuji, H. Takagi, *Phys. Rev. B* **64**, 054415 (2001).
143. H.-H. Wang, A. Fleet, J.D. Brock, D. Dale, Y. Suzuki, *J. Appl. Phys.* **96**, 5324 (2004).
144. K. Kugimiya, K. Fujita, K. Tanaka, K. Hirao, *J. Magn. Magn. Mater.* **310**, 2268 (2007).
145. S.C. Chae, Y.J. Chang, D.-W. Kim, B.W. Lee, I. Choi, C.U. Jung, *J. Electroceram.* **22**, 216 (2009).
146. K. Fujita, N. Wakasugi, S. Murai, Y. Zong, K. Tanaka, *Appl. Phys. Lett.* **94**, 062512 (2009).
147. M.W. Schafer, *J. Appl. Phys.* **36**, 1145 (1965).
148. G.J. McCarthy, W.B. White, R. Roy, *J. Inorg. Nucl. Chem.* **31**, 329 (1969).
149. Y.S. Kim, D.J. Kim, T.H. Kim, T.W. Noh, J.S. Choi, B.H. Park, J.-G. Yoon, *Appl. Phys. Lett.* **91**, 042908 (2007).
150. K.A. Müller, H. Burkard, *Phys. Rev. B* **19**, 3593 (1979).
151. E.J. Tarsa, E.A. Hachfeld, F.T. Quinlan, J.S. Speck, M. Eddy, *Appl. Phys. Lett.* **68**, 490 (1996).
152. T. Ohnishi, M. Lippmaa, T. Yamamoto, S. Meguro, H. Koinuma, *Appl. Phys. Lett.* **87**, 2419191 (2005).
153. T. Ohnishi, K. Shibuya, T. Yamamoto, M. Lippmaa, *J. Appl. Phys.* **103**, 103703 (2008).
154. M. Kestigian, J.G. Dickinson, R. Ward, *J. Am. Chem. Soc.* **79**, 5598 (1957).
155. D.A. Tenne, I.E. Gonenli, A. Soukiassian, D.G. Schlom, S.M. Nakhmanson, K.M. Rabe, X.X. Xi, *Phys. Rev. B* **76**, 024303 (2007).
156. C.M. Brooks, L. Fitting Kourkoutis, T. Heeg, J. Schubert, D.A. Muller, D.G. Schlom, *Appl. Phys. Lett.* **94**, 162905 (2009).
157. J.H. Lee, X. Ke, N.J. Podraza, L. Fitting Kourkoutis, T. Heeg, M. Roeckerath, J.W. Freeland, C.J. Fennie, J. Schubert, D.A. Muller, P. Schiffer, D.G. Schlom, *Appl. Phys. Lett.* **94**, 212509 (2009).
158. J.H. Lee, K.M. Rabe, *Phys. Rev. Lett.* **104**, 207204 (2010).
159. E. Bousquet, N.A. Spaldin, P. Ghosez, *Phys. Rev. Lett.* **104**, 037601 (2010).
160. P.J. Ryan, J.-W. Kim, T. Birol, P. Thompson, J.-H. Lee, X. Ke, P.S. Normile, E. Karapetrova, P. Schiffer, S.D. Brown, C.J. Fennie, D.G. Schlom, *Nat. Commun.* **4**, 1334 (2013).
161. C.H. Lee, N.D. Orloff, T. Birol, Y. Zhu, V. Goian, E. Rocas, R. Haislmaier, E. Vlahos, J.A. Mundy, L.F. Kourkoutis, Y. Nie, M.D. Biegalski, J. Zhang, M. Bernhagen, N.A. Benedek, Y. Kim, J.D. Brock, R. Uecker, X.X. Xi, V. Gopalan, D. Nuzhnyy, S. Kamba, D.A. Muller, I. Takeuchi, J.C. Booth, C.J. Fennie, D.G. Schlom, *Nature* **502**, 532 (2013).
162. O.G. Vendik, *Ferroelectrics* **12**, 85 (1976).
163. S.W. Kirchoefer, J.M. Pond, A.C. Carter, W. Chang, K.K. Agarwal, J.S. Horwitz, D.B. Chrisey, *Microwave Opt. Technol. Lett.* **18**, 168 (1998).
164. S.S. Gevorgian, E.L. Kollberg, *IEEE Trans. Microwave Theory Tech.* **49**, 2117 (2001).
165. A.K. Tagantsev, V.O. Sherman, K.F. Astafiev, J. Venkatesh, N. Setter, *J. Electroceram.* **11**, 5 (2003).
166. S. Andersson, A.D. Wadsley, *Nature* **211**, 581 (1966).
167. J.S. Anderson, J.M. Browne, A.K. Cheetham, R. Vondree, J.L. Hutchison, F.J. Lincoln, D.J.M. Bevan, J. Straehle, *Nature* **243**, 81 (1973).
168. R.J.D. Tilley, *Nature* **269**, 229 (1977).
169. R.J.D. Tilley, *J. Solid State Chem.* **21**, 293 (1977).
170. T. Nakamura, P.H. Sun, Y.J. Shan, Y. Inaguma, M. Itoh, I.S. Kim, J.H. Sohn, M. Ikeda, T. Kitamura, H. Konagaya, *Ferroelectrics* **196**, 205 (1997).
171. P.L. Wise, I.M. Reaney, W.E. Lee, T.J. Price, D.M. Iddles, D.S. Cannell, *J. Eur. Ceram. Soc.* **21**, 1723 (2001).
172. N.D. Orloff, W. Tian, C.J. Fennie, C.H. Lee, D. Gu, J. Mateu, X.X. Xi, K.M. Rabe, D.G. Schlom, I. Takeuchi, J.C. Booth, *Appl. Phys. Lett.* **94**, 042908 (2009).
173. T. Birol, N.A. Benedek, C.J. Fennie, *Phys. Rev. Lett.* **107**, 257602 (2011).
174. D.O. Klenov, W. Donner, B. Foran, S. Stemmer, *Appl. Phys. Lett.* **82**, 3427 (2003).
175. W. Donner, C. Chen, M. Liu, A.J. Jacobson, Y.-L. Lee, M. Gadre, D. Morgan, *Chem. Mater.* **23**, 984 (2011).
176. J.M. Rondinelli, N.A. Spaldin, *Adv. Mater.* **23**, 3363 (2011).
177. J.M. Rondinelli, S.J. May, J.W. Freeland, *MRS Bull.* **37**, 261 (2012).
178. W.S. Choi, J.-H. Kwon, H. Jeon, J.E. Hamann-Borrero, A. Radi, S. Macke, R. Sutarto, F. He, G.A. Sawatzky, V. Hinkov, M. Kim, H.N. Lee, *Nano Lett.* **12**, 4966 (2012).
179. Y. Yang, C.M. Schlepütz, C. Adamo, D.G. Schlom, R. Clarke, *APL Mater.* **1**, 052102 (2013).
180. C.-L. Jia, V. Nagarajan, J.-Q. He, L. Houben, T. Zhao, R. Ramesh, K. Urban, R. Waser, *Nat. Mater.* **6**, 64 (2006).
181. C.-L. Jia, S.-B. Mi, K. Urban, I. Vrejoiu, M. Alexe, D. Hesse, *Nat. Mater.* **7**, 57 (2008).
182. C.T. Nelson, B. Winchester, Y. Zhang, S.-J. Kim, A. Melville, C. Adamo, C.M. Folkman, S.-H. Baek, C.-B. Eom, D.G. Schlom, L.-Q. Chen, X. Pan, *Nano Lett.* **11**, 828 (2011).
183. C.L. Jia, K.W. Urban, M. Alexe, D. Hesse, I. Vrejoiu, *Science* **331**, 1420 (2011).
184. A.Y. Borisevich, H.J. Chang, M. Huijben, M.P. Oxley, S. Okamoto, M.K. Niranjan, J.D. Burton, E.Y. Tsybmal, Y.H. Chu, P. Yu, R. Ramesh, S.V. Kalinin, S.J. Pennycook, *Phys. Rev. Lett.* **105**, 087204 (2010).
185. D.A. Muller, L.F. Kourkoutis, M. Murfitt, J.H. Song, H.Y. Hwang, J. Silcox, N. Dellby, O.L. Krivanek, *Science* **319**, 1073 (2008).
186. D. Lee, R. Behera, P. Wu, H. Xu, Y.L. Li, S.B. Sinnott, S. Phillpot, L. Chen, V. Gopalan, *Phys. Rev. B* **80**, 060102 (2009).
187. E.F. Kneller, R. Hawig, *Magnetics, IEEE Trans. Magn.* **27**, 3588 (1991).
188. E.E. Fullerton, J.S. Jiang, S.D. Bader, *J. Magn. Magn. Mater.* **200**, 392 (1999).
189. P. Wu, X. Ma, Y. Li, V. Gopalan, L.Q. Chen, *Appl. Phys. Lett.* **100**, 092905 (2012).
190. J.H. Lee, K.M. Rabe, *Phys. Rev. Lett.* **107**, 067601 (2011).
191. D.M. Newsn, B.G. Elmegreen, X.-H. Liu, G.J. Martyna, *Adv. Mater.* **24**, 3672 (2012).
192. D. Newsn, B. Elmegreen, X. Hu Liu, G. Martyna, *J. Appl. Phys.* **111**, 084509 (2012).
193. R.E. Newnham, J.J. Kramer, W.A. Schulze, L.E. Cross, *J. Appl. Phys.* **49**, 6088 (1978).
194. M.J. Harris, S.T. Bramwell, D.F. McMorrow, T. Zeiske, K.W. Godfrey, *Phys. Rev. Lett.* **79**, 2554 (1997).

195. C. Fennie, K. Rabe, *Phys. Rev. B* **72**, 100103 (2005).
 196. T. Choi, Y. Horibe, H.T. Yi, Y.J. Choi, W. Wu, S.W. Cheong, *Nat. Mater.* **9**, 253 (2010).
 197. A. Arkenbout, T. Palstra, T. Siegrist, T. Kimura, *Phys. Rev. B* **74**, 184431 (2006).
 198. F. Ye, Y. Ren, Q. Huang, J. Fernandez-Baca, P. Dai, J. Lynn, T. Kimura, *Phys. Rev. B* **73**, 220404 (2006).
 199. T. Kimura, Y. Sekio, H. Nakamura, T. Siegrist, A.P. Ramirez, *Nat. Mater.* **7**, 291 (2008).
 200. Y. Kitagawa, Y. Hiraoka, T. Honda, T. Ishikura, H. Nakamura, T. Kimura, *Nat. Mater.* **9**, 797 (2010).
 201. A.A. Bossak, I.E. Graboy, O.Y. Gorbenko, A.R. Kaul, M.S. Kartavtseva, V.L. Svetchnikov, H.W. Zandbergen, *Chem. Mater.* **16**, 1751 (2004).
 202. W. Wang, J. Zhao, W. Wang, Z. Gai, N. Balke, M. Chi, H.N. Lee, W. Tian, L. Zhu, X. Cheng, D.J. Keavney, J. Yi, T.Z. Ward, P.C. Snijders, H.M. Christen, W. Wu, J. Shen, X. Xu, *Phys. Rev. Lett.* **110**, 237601 (2013).
 203. E.S. Machlin, P. Chaudhari, in *Synthesis and Properties of Metastable Phases*, E.S. Machlin, T.J. Rowland, Eds. (The Metallurgical Society of AIME, Warrendale, 1980), pp. 11–29.
 204. C.P. Flynn, *Phys. Rev. Lett.* **57**, 599 (1986).
 205. R. Bruinsma, A. Zangwill, *J. Phys. (Paris)* **47**, 2055 (1986).
 206. O.Y. Gorbenko, S.V. Samoilenkov, I.E. Graboy, A.R. Kaul, *Chem. Mater.* **14**, 4026 (2002).
 207. J.M. Rondinelli, C.J. Fennie, *Adv. Mater.* **24**, 1961 (2012).
 208. A.T. Mulder, N.A. Benedek, J.M. Rondinelli, C.J. Fennie, *Adv. Funct. Mater.* **23**, 4810 (2013).
 209. C.J. Fennie, *Phys. Rev. Lett.* **100**, 167203 (2008).
 210. T. Varga, A. Kumar, E. Vlahos, S. Denev, M. Park, S. Hong, T. Sanehira, Y. Wang, C. Fennie, S. Streiffner, X. Ke, P. Schiffer, V. Gopalan, J. Mitchell, *Phys. Rev. Lett.* **103**, 047601 (2009).
 211. G. Singh-Bhalla, C. Bell, J. Ravichandran, W. Siemons, Y. Hikita, S. Salahuddin, A.F. Hebard, H.Y. Hwang, R. Ramesh, *Nat. Phys.* **7**, 80 (2010). □

Career Center

JOB SEEKERS MEET YOUR NEXT EMPLOYER!

We'll show off your talents to the world's most prestigious high-tech firms, universities and laboratories. At the 2014 MRS Spring Meeting Career Center, you can access many interesting job postings, visit recruitment booths and interview with prospective employers. Please bring extra copies of your resume for your own use.

The Career Center is FREE to all MRS members and those registered to attend the 2014 MRS Spring Meeting.

ON-SITE REGISTRATION HOURS


Monday, April 21 1:00 pm – 4:00 pm
(Candidate Registration Only)

CAREER CENTER HOURS

Tuesday, April 22 10:00 am – 5:00 pm
Wednesday, April 23 10:00 am – 5:00 pm


Register and submit your resume today!
www.mrs.org/spring-2014-career-center

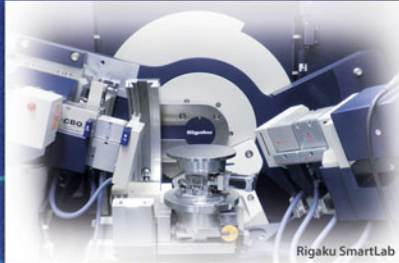




Rigaku

Better measurements. Better confidence. Better world.





Rigaku SmartLab


www.Rigaku.com/products/xrd/smartlab

Powder Diffraction • Thin Film Diffraction • SAXS • In-Plane Grazing Incidence

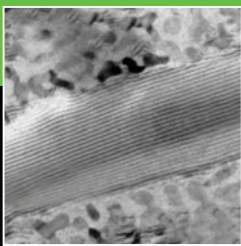
Rigaku's SmartLab® is the most versatile diffractometer in the world. You can start using all XRD applications from the very first day because of the unique knowledge-based Guidance control software. The available 9 kW line focus X-ray source provides ultimate power for the most demanding applications. Automatic self-alignment ensures that you always collect the best data possible and beam path selection can be made without touching a multilayer optic.

for Material Scientists

The SmartLab combined with a novel two-dimensional detector enables one to measure a large-area reciprocal space map in minutes rather than days.



Rigaku Corporation and its Global Subsidiaries | www.Rigaku.com | info@Rigaku.com



Strain scaling for CMOS

S.W. Bedell, A. Khakifirooz, and D.K. Sadana

This article describes various techniques for applying strain to current and future complementary metal–oxide–semiconductor (CMOS) channels to boost CMOS performance. A brief history of both biaxial and uniaxial strain engineering in planar CMOS technology is discussed. Scalability challenges associated with process-induced uniaxial strain in sub-22 nm CMOS is highlighted in view of shrinking device dimensions and 3D device architecture (such as fin field-effect transistors [FinFETs]). Non-uniform strain relaxation in patterned geometries in tight pitch two- and three-dimensional devices is addressed. A case is made that the future scalable strain platform will require a combination of biaxial strain at wafer level in conjunction with local uniaxial strain. Finally, potential application of strain engineering to advanced III–V metal oxide semiconductor FET channels will be examined.

Brief history of strain engineering in planar CMOS technology

Over the past few decades, a great deal of theoretical and experimental work has been carried out in the field of carrier transport in strained semiconductors;¹ however, it was not until the late 1990s that strained channels were viewed as requisite elements in complementary metal–oxide–semiconductor (CMOS) technology. Since then, a variety of innovative techniques have been devised and integrated as strain-inducing elements into existing CMOS technology. For example, compressive and tensile stressed silicon nitride liners,² wafer-scale biaxial strain,³ local epitaxial stressors for uniaxial strain,⁴ and even the strain fields surrounding defects⁵ have been used to improve the current drive of modern field-effect transistors (FETs). Here, we explore the most successful of these strain-inducing approaches in planar FET technology, namely lattice-engineering by epitaxial growth. We begin by presenting some of the early work on biaxial strain engineering for FET applications that showed a promising path for drive current enhancement by improving the electron and hole mobility in Si. We then describe the introduction of process-induced uniaxial strain and its advantages compared to biaxial strain with respect to drive current in scaled FETs. Finally, the limitations of strain scaling and possible future strategies are explored.

The perfect miscibility of the $\text{Ge}_x\text{Si}_{(1-x)}$ alloy system permits control of the lattice parameter from that of Si (0.543 nm) to that of Ge (0.566 nm) by controlling the composition during epitaxial growth. Because the lattice parameters of these alloys are larger than that of Si, subsequent layers of Si grown on relaxed $\text{Ge}_x\text{Si}_{(1-x)}$ alloy layers will be under tensile strain. Early work⁶ on thick, strain-relaxed compositionally graded $\text{Ge}_x\text{Si}_{(1-x)}$ layers grown on Si substrates demonstrated that although relaxation was dislocation-mediated, defect densities could be made relatively low ($\sim 10^6\text{ cm}^{-2}$). Shortly thereafter, some of the first strained-Si FET devices were fabricated using thin Si layers grown on these thick, relaxed $\text{Ge}_x\text{Si}_{(1-x)}$ graded buffer layers (GBLs) formed on Si substrates. The amount of (biaxial) tensile strain in the thin Si channel layer was varied by controlling the Ge content in the GBL. This process of engineering the lattice parameter directly on the starting substrate prior to device fabrication would eventually be referred to as “wafer-scale” or “global” strain. The main advantages to this approach were that the magnitude and uniformity of the strain could be well-controlled, and standard device fabrication steps could then be used. Both electron³ and hole⁷ mobilities were shown to improve significantly with increasing strain in long-channel FETs fabricated on biaxially strained Si using this approach.

S.W. Bedell, IBM T.J. Watson Research Center; bedells@us.ibm.com
A. Khakifirooz, IBM T.J. Watson Research Center; khaki@us.ibm.com
D.K. Sadana, IBM T.J. Watson Research Center; dksadana@us.ibm.com
DOI: 10.1557/mrs.2014.5

Based largely on these early results, and the prospect of both *n*- and *p*-type FET (nFET and pFET) drive current enhancement using the same strained Si layer, attempts were made to develop production-worthy relaxed $\text{Ge}_x\text{Si}_{(1-x)}$ buffer layers as the starting substrates for biaxial strained Si CMOS. IBM demonstrated functional strained Si (0.55% tensile strain) CMOS with an nFET drive current enhancement of 80% for long channel devices and ~20% for 60 nm devices compared to silicon-on-insulator (SOI) control devices using SiGe-on-insulator (SGOI) substrates. **Figure 1a** shows a cross-sectional TEM image of the biaxially strained Si nFET device.⁸ The SGOI substrates represented a new way to integrate strain-relaxed SiGe buffer layers with SOI technology and were fabricated by high-temperature (~1250°C) oxidation of epitaxial SiGe layers grown on SOI wafers. This process allowed the formation of thin, high-quality SiGe layers directly on a buried oxide layer. Because the relaxation during oxidation was strictly dislocation-mediated for unpatterned wafers, both the Ge content as well as the final strain state of the SGOI (including fully strained) could be controlled independently.⁹ Although the observed nFET drive current enhancement was notable, the pFET devices did not show any drive current enhancement.

By growing strained $\text{Ge}_x\text{Si}_{(1-x)}$ layers within the source/drain regions of the device, uniaxial compressive strain can be imparted to the channel region directly. The introduction of this “process-induced” or “local” channel strain using embedded SiGe in pFET devices¹⁰ demonstrated the advantages of uniaxial compressive over biaxial tensile strain in hole transport. In that work, greater than 50% enhancement in hole mobility was reported as a result of both uniaxial channel strain and reduced access resistance due to the higher amount of substitutional B in the SiGe alloy and reduction of the Schottky barrier height between the silicide and the SiGe. **Figure 1b** shows a cross-sectional TEM image of a pFET device with uniaxial channel strain using embedded SiGe in

the source/drain regions. The advantage of uniaxial compressive strain compared to biaxial tensile strain in hole transport is ascribed to the difference in the resulting band structure in the two cases.¹¹ The primary origin of hole mobility enhancement in biaxial tensile Si is the reduced scattering that results from strain-induced splitting of the heavy and light hole sub-bands. In the case of uniaxial compressive Si, the primary origin is valence band warping resulting in a lower effective mass in the channel direction. In devices with channel lengths in the tens of nanometers, scattering becomes less important than carrier mass, and therefore uniaxial compressive strain results in superior drive current enhancement in scaled pFETs. Additionally, valence band splitting due to confinement effects in biaxial tensile Si counteract the strain-induced splitting, leading to overall degradation of hole mobility at high vertical electric fields. For nFET devices, biaxial tensile and uniaxial tensile strains both led to mobility enhancement. The complete analysis is somewhat more complicated, and an excellent review can be found in Reference 11.

Scalability of process-induced strain

In subsequent technology generations, uniaxial process-induced strain was increased in a number of ways, including by (1) increasing the Ge content of the embedded SiGe (e-SiGe), (2) increasing the proximity of the SiGe stressor to the channel region (including thinner spacers and alternate recess geometry), and (3) taking advantage of replacement gate integration schemes to transfer more strain to the channel (including strained gate material).^{12,13} In fact, the uniaxial strain engineering approach has been leveraged not only in pFETs but also in nFETs to increase effective strain in both types of channels in the latest 22 nm technology node.¹⁴ A fourth generation of pFET e-SiGe (**Figure 2a**) and a novel *in situ* doped nFET e-Si:C (**Figure 2b**) have been introduced into IBM’s 22 nm CMOS. Because nFETs require uniaxial tensile strain to enhance electron mobility, a material with a smaller lattice

parameter than Si must be used in the source/drain region. Unfortunately, the perfectly miscible SiGe alloy system has no counterpart to enable lattice contraction. The very low solubility of C in Si (~ 10^{17} cm^{-3}) makes using the Si:C system as a stressor layer challenging. However, by incorporating ~1.5% substitutional carbon, the embedded Si:C (e-Si:C) applies ~340 MPa additional tensile strain to the nFET channel for improved electron mobility. The dual embedded source/drain modules are integrated with dual stress liners, with a resulting nominal strain enhancement of ~1.25× relative to 32 nm SOI (**Figure 2c**).

Limitations of process-induced strain scaling

Although strain scaling efforts have largely been successful so far, the continued shrinking

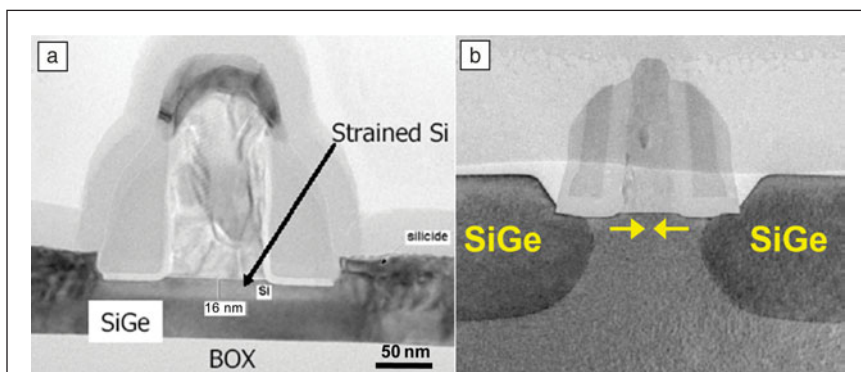
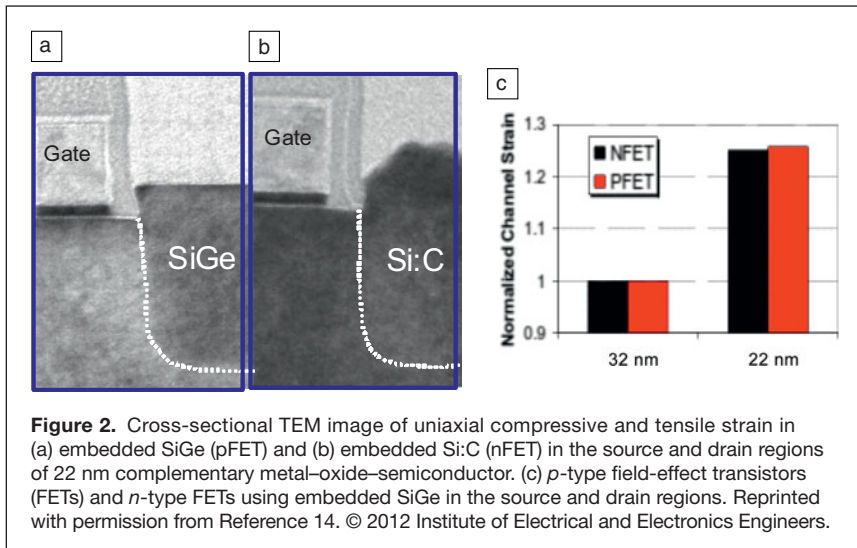


Figure 1. (a) Cross-sectional transmission electron microscopy (TEM) image of biaxial (tensile) strained Si *n*-type field-effect transistor (FET) fabricated using SiGe-on-insulator as a growth template. Reprinted with permission from Reference 8. © 2004 American Institute of Physics. (b) Cross-sectional TEM image of an uniaxial strained (compressive) *p*-type FET device using embedded SiGe in the source and drain regions. Reprinted with permission from Reference 10. © 2003 IEEE.



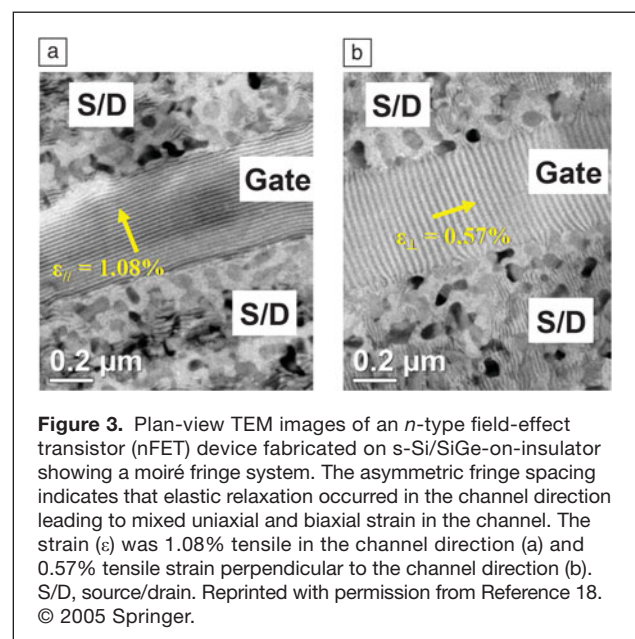
of device pitch (feature density) at approximately fixed gate length is making localized stressors less effective at each technology generation. Due to the loss of embedded SiGe volume in pFETs, one has to increase Ge content and increase proximity simply to match the transistor performance benchmarks of the previous technology generation.¹⁵ Similarly, C substitutional content has to increase from the current 1.5% to >2% in the future to maintain nFET performance scaling, and this is highly challenging. Even though both dimensional scaling and strain scaling in Si pose fundamental physical limitations, future strain scaling may end up having a more abrupt terminus in the form of material failure. For example, a high density of defects accompanied by stress relaxation is expected in pFETs with high Ge content in the embedded Si_xGe_y (e.g., >50%). Similarly, defects in high substitutional C are expected to create strain relaxation in nFETs in addition to lower *n*-doping. We next describe a potential path forward to continue strain scaling beyond 22 nm CMOS.

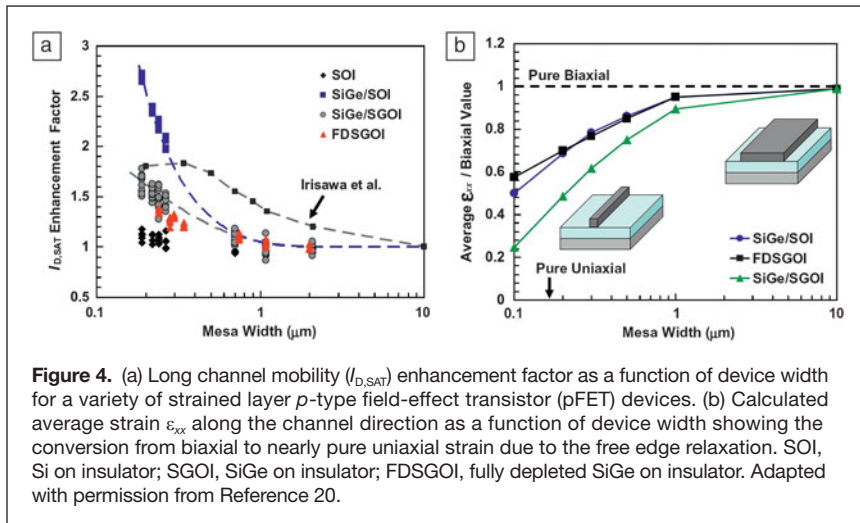
A scalable strain platform: Mixed bi- and uniaxial wafer-level strain

One of the strongest arguments in favor of wafer-level strain as opposed to process-induced strain has always been that the former is independent of device pitch. In other words, because the strained material is integral to the substrate itself, the magnitude of strain would be independent of patterned feature (mesa) size or device geometry. This is true for dimensions down to roughly the micron length scale, however, below this, elastic relaxation due to the free edges of the mesa becomes a significant fraction of the average strain across the mesa. Early work on elastic (non-dislocation mediated) relaxation of strained SiGe islands on borophosphate silicate glass layers^{16,17} showed that if the oxide layer was above the reflow temperature, strained SiGe layers could relax by physical expansion. In early 2005, plan-view transmission electron microscopy (TEM) moiré analysis was used to map the two-dimensional

strain fields in nFET devices formed on SGOI substrates.¹⁸ Mixed biaxial and uniaxial strain components were shown to exist under the gate regions formed on asymmetric mesas, indicating that mesa geometry could be used to convert biaxial strained layers into mixed biaxial/uniaxial ones. **Figure 3** shows a plan-view TEM image of an nFET device with a fringe system (moiré pattern) resulting from the two-beam interference between the Si/SGOI above the buried SiO₂ (BOX) layer and the bulk Si below the BOX layer. By converting the fringe spacing into strain, it is concluded that 1.08% tensile Si strain is present parallel with the channel direction, while only 0.57% Si strain is present perpendicular to the channel.

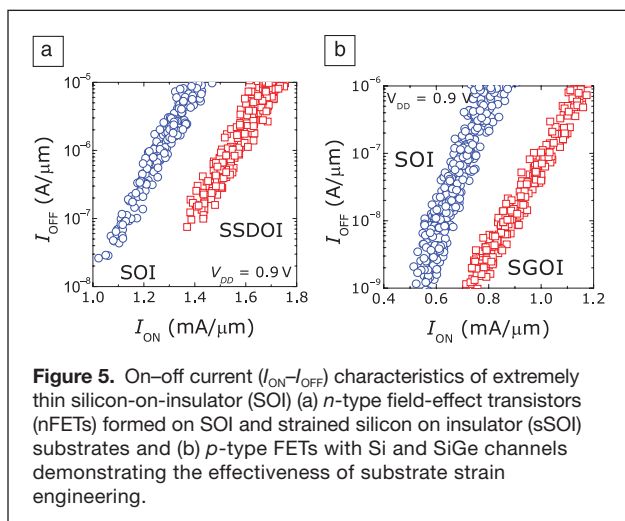
Later, pFET devices were demonstrated¹⁹ on elastically relaxed SGOI mesas. Mobility enhancement was measured as a function of device width, which essentially translates into pure biaxial strain for the widest mesas to nearly pure uniaxial. The results showed an astounding ~2× drive current enhancement for mesa widths below about 0.3 μm. Because nearly all modern CMOS technology features are at or below these dimensions, this approach may open up new opportunities for scalable strain engineering. The effect of biaxial-to-uniaxial conversion by elastic relaxation was studied on a number of different strained layer combinations for pFET devices,²⁰ and the results were consistent with the performance enhancement results in Reference 19. In the latter work, the simplest structure, namely SiGe/SOI, showed the highest drain current enhancement (2.7× for long channels and 2× for short channels).²⁰ Moreover, the SiGe/SOI devices with the smallest width demonstrated on-off current ratio (I_{ON}/I_{OFF}) characteristics





comparable to published pFET data with process-induced uniaxial strain. **Figure 4** shows a summary of the effect of uniaxial strain conversion on a variety of device structures (long channel) compared to the calculated average strain along the mesa width.²⁰

The above approach of mixed biaxial and uniaxial strain has recently been extended to enhance the drive current of fully depleted nFETs in extremely thin (ETSOI) substrates where the device layer contains strained Si.²¹ These substrates are known as strained silicon on insulator (sSOI) substrates. **Figure 5a**²² shows that at $\sim 0.8\%$ tensile strain in sSOI, an I_{ON} enhancement of $\sim 25\%$ is achieved in nFETs over those fabricated on virgin SOI despite 100 nm gate pitch. Most recently, similar results have been reported on FinFETs fabricated on sSOI substrates, with gate pitch down to 64 nm.²³ Similarly, the effectiveness of a compressively strained SGOI substrate²² in enhancing the drive current of a pFET is apparent in **Figure 5b**. At $\sim 0.9\%$ strain in SGOI, I_{ON} enhancement of $\sim 35\%$ in pFETs is achieved over those fabricated on virgin SOI.



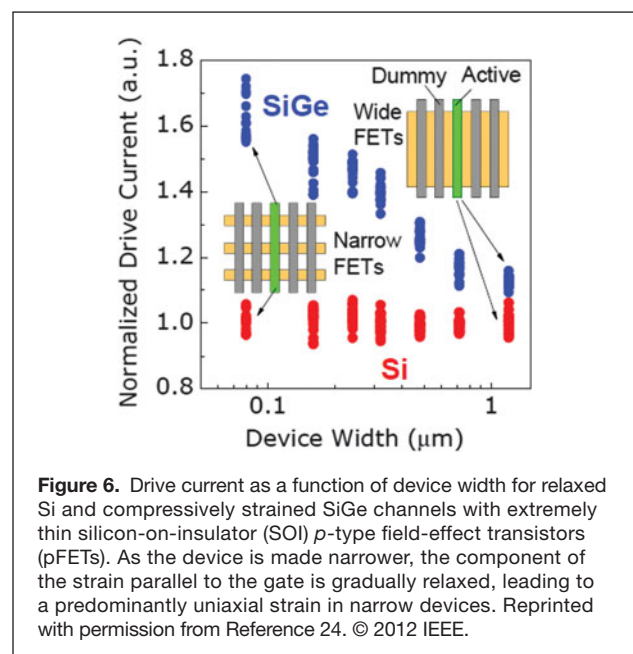
The effect of strain relaxation at the edges of a narrow ETSOI pFET is shown in **Figure 6**.²⁴ In a relatively wide device (e.g., 1 μm wide), the compressive strain in the SiGe channel is purely biaxial, and the I_{ON} enhancement is modest ($<20\%$). However, as the devices are made narrower and strain relaxation at edges increases, part of the biaxial strain is converted to uniaxial strain (see earlier discussion, **Figures 3** and **4**), thus contributing to even higher I_{ON} . The conversion of predominantly biaxial strain to predominantly uniaxial strain in narrow devices bodes well for substrate engineering-based strain scaling for future CMOS.

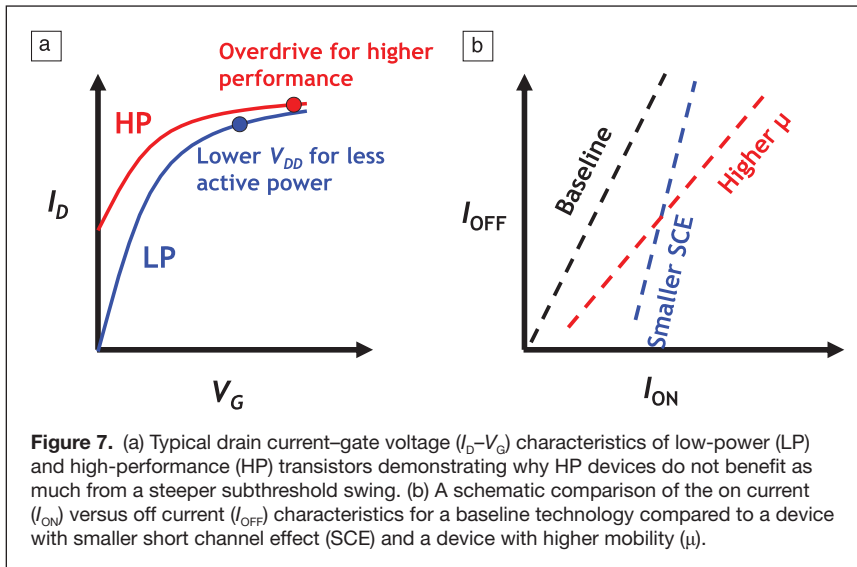
Nevertheless, edge relaxation in small devices is still a concern. Proper process engineering is required to alleviate such stress relaxation. For example, recessing of source and drain regions, which is traditionally used to form embedded stressors, should be avoided and instead raised source drain structures should be used. Similarly, implantation in source-drain regions should either be avoided altogether, or implant conditions should be adjusted to minimize strain relaxation.

3D device architectures: FinFETs

It has been frequently argued that with a steeper subthreshold swing in a fully depleted device, such as a FinFET, strain may not be required as a performance booster. Smaller subthreshold swing and drain-induced barrier lowering in these devices compared to bulk CMOS are considered to be performance boosters.

At low I_{OFF} , better short channel control in FinFETs indeed provides a significant boost compared to the baseline, but this





benefit diminishes at higher I_{OFF} , where high-performance devices typically operate. Low-power devices that operate at supply voltages (V_{DD}) smaller than 1 V with I_{OFF} in the low $\text{nA } \mu\text{m}^{-1}$ range (to reduce active and leakage power) can benefit significantly from a smaller subthreshold swing (Figure 7). However, high-performance applications that operate at higher supply voltages (typically >1 V) with I_{OFF} in the hundreds of $\text{nA } \mu\text{m}^{-1}$ range (for maximum performance) require both higher channel mobility (Figure 7) and improved short channel control.²⁵ Therefore, there is a drive to apply strain engineering even to FinFETs.

Strain engineering in FinFETs

Several theoretical and experimental studies have already been conducted to determine channel strain-carrier mobility correlation in FinFETs at the fundamental level. This includes carrier mobility measurements in FinFETs²⁶⁻²⁸ under mechanical strain by wafer bending. However, since the magnitude of the maximum mechanical strain is limited to $<0.1\%$, these experiments do not provide quantitative feedback that is required to accurately calibrate theoretical calculations and for an in-depth understanding of high-field carrier transport in short channel FinFETs. We next describe the role and limitations of strain engineering in FinFETs.

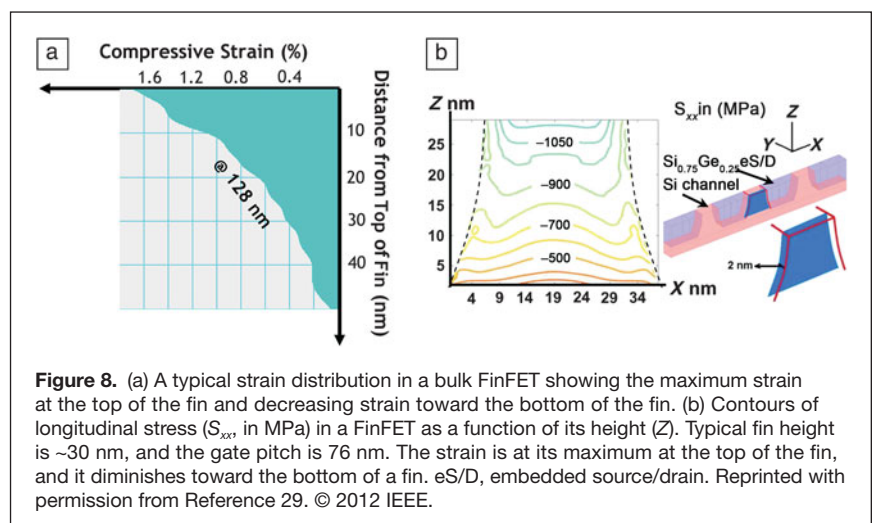
Technology computer aided design (TCAD) simulations have been used to study the effectiveness of process-induced stressors previously developed for planar devices, such as e-SiGe, SiN_x stress liners, gate electrodes, contacts, and device isolation in FinFET structures.²⁹⁻³¹ It was shown that strain transfer in FinFETs can occur in an analogous manner to planar FETs, albeit with a non-uniform strain distribution due to its three-dimensional nature. However, initial

experimental data suggest that the magnitude of strain transfer in FinFETs is lower than that in planar FETs. For example, the I_{ON} data from 22 nm FinFETs, when normalized to the actual device width, are inferior to that from 32 nm planar FETs, suggesting that the effective channel strain is lower in FinFETs than in planar FETs. This occurs despite increased Ge content in e-SiGe and its closer proximity to the channel in FinFETs.

Figure 8a shows the strain profile along the fin height measured using nano-beam diffraction in a typical bulk FinFET with e-SiGe. The maximum strain occurs at the top of the fin where its magnitude is comparable to what is expected from a planar device with an equivalent e-SiGe. The strain decreases gradually from the top of the fin toward its bottom. Consequently, the average mobility boost

is only a fraction (nearly half) of that in a planar device. This observation is in qualitative agreement with TCAD simulations,²⁹ shown in Figure 8b. It should be noted that non-uniform strain distribution occurs even in bulk planar devices; however, its impact on such devices is minimal because carrier transport is localized in the vicinity of the top surface.

Despite an overall reduction in strain, e-SiGe remains an upfront option for future high-performance pFinFETs because in addition to strain, e-SiGe provides much needed low series resistance to achieve high drive current. Another effective knob to enhance strain, particularly in FinFETs, is the gate electrode itself, as it wraps around the channel and can efficiently transfer its stress to the channel.³² In fact, process conditions to produce gate electrodes with the desired strain level have already been identified, and direct coupling of the gate stress to the channel has also been confirmed by both physical (strain measurements) and electrical measurements. However,



the choice of the stressor metal electrode is constrained by not only its work function, which impacts the threshold voltage, but also other factors, such as inversion capacitance, device reliability, and complexity of integration.

Substrate strain engineering for high-performance FinFETs

Although, performance gain in nFinFETs on sSOI and pFinFETs on SGOI with a relaxed pitch has been experimentally verified,³³ such gain and its magnitude in tight ground-rule (<100 nm pitch) devices has yet to be determined. Furthermore, co-integration of nFETs and pFETs will require two opposite kinds of strain (i.e., tensile and compressive) on the same substrate, which has not yet been demonstrated. It may be possible to convert tensile strain of sSOI to compressive strain locally via a combination of selective SiGe (>40%) growth and thermal mixing (or Ge condensation).

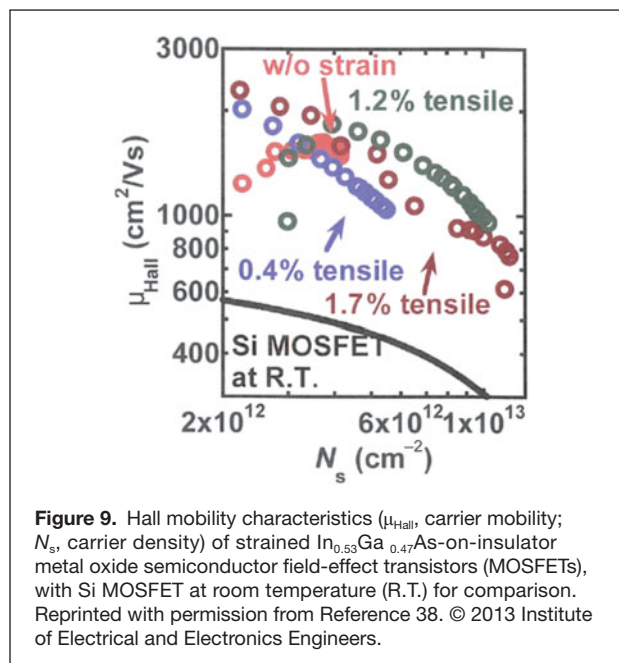
Strain effects in III–V devices

Even though III–V compounds can provide a wealth of strain engineering options for both *n*- and/or *p*FETs because of a variety of substrate/grown layer combinations, there is a surprisingly limited body of published literature on this topic.^{34–37} For example, for *n*-channel devices, InGaAs can be grown with tensile or compressive strain by varying the In and/or Ga content on an InP or a GaAs substrate. Similarly, compressively strained AlGaSb can be grown on GaAs, or InGaSb can be grown on GaSb in multiple configurations (single or multiple quantum wells) for *p*-channels.

Unlike for electrons in III–Vs, where polar scattering is the only dominant scattering mechanism, both deformation potential and polar scattering mechanisms are important for hole mobility. The hole mobility can be significantly enhanced by varying the group V element while keeping the group III element fixed. For example, hole mobility increases from 200 for InP to 450 for InAs to 850 cm² V⁻¹ s⁻¹ for InSb. A similar pattern is true for holes in GaP (150 cm² V⁻¹ s⁻¹) to GaSb (900 cm² V⁻¹ s⁻¹).³⁵ On the other hand, varying the III element does not significantly impact the hole mobility. The impact of strain on *p*-type hole mobility is profound, especially that of compressive strain, which yields 2× mobility enhancement under a biaxial strain of 2%. The hole mobility enhancement for GaAs under uniaxial compressive strain is expected to be even greater (10).

The effect of strain on the quantized bandgaps of both 5 nm (001) and (111) GaAs and In_{0.75}Ga_{0.25}As has been studied in detail.³⁴ The quantized bandgap narrows under compressive strain and increases under tensile strain. The observed bandgap modulation in conjunction with strain is very attractive for InGaAs based III–V metal oxide semiconductor FETs (MOSFETs) and can potentially be exploited to reduce band-to-band tunneling current while maintaining high channel mobility.

The latest MOSFETs fabricated on strained InGaAs-on-insulator indeed confirm that high strain up to 1.7% can be



successfully introduced in the channels, and these channels exhibit 1.65× mobility enhancement compared to those without strain (Figure 9).³⁸ These results indicate that the thin body (<15 nm) III–V-on-insulator structure with highly strained channels is a promising way to realize ultimately scaled future III–V MOSFETs.

Concluding remarks

Implementation of strain as a performance enhancing element has been phenomenally successful and effective since 90 nm Si CMOS. Strain scaling has continued unabated through 22 nm CMOS via a combination of SiGe and Si:C epitaxial stressors, dielectric stressors, and crystallographic defects in the vicinity of the MOSFET channel. However, such strain scaling in future CMOS is becoming challenging due to the limited device footprint and device geometry (planar or FinFETs). We have demonstrated that a combination of wafer level biaxial strain in conjunction with local uniaxial strain can provide a plausible platform for continued strain scaling in Si. Advances in cost-effective SGOI and sSOI substrate manufacturing in conjunction with successful reduction in substrate defect density will be paramount for continued success of strain scaling in Si. The demonstrated performance benefit of strain in III–Vs should open yet another option for continued CMOS scaling beyond 2020.

Acknowledgments

The author would like to acknowledge contributions from IBM's Yorktown, Fishkill, and Albany process and integration teams. We are indebted to Ghavam Shahidi for his support, and Shreesh Narasimha for insightful discussions on IBM's strain-Si technology.

References

1. H.M. Manasevit, I.S. Gergis, A.B. Jones, *Appl. Phys. Lett.* **41**, 464 (1982).
2. S. Ito, H. Namba, K. Yamaguchi, T. Hirata, K. Ando, S. Koyama, S. Kuroki, N. Ikezawa, T. Suzuki, T. Saitoh, T. Horiuchi, *IEDM Tech. Dig.* 247 (2000).
3. J. Welsler, J.L. Hoyt, J.F. Gibbons, *IEDM Tech. Dig.* 1000 (1992).
4. S. Gannavaram, N. Pesovic, C. Ozturk, *IEDM Tech. Dig.* 437 (2000).
5. K.-Y. Lim, H. Lee, C. Ryu, K.-I. Seo, U. Kwon, S. Kim, J. Choi, K. Oh, H.K. Jeon, C. Song, T.-O. Kwon, J. Cho, S. Lee, Y. Sohn, H.S. Yoon, J. Park, K. Lee, W. Kim, E. Lee, S.-P. Sim, C.G. Koh, S.B. Kang, S. Choi, C. Chung, *IEDM Tech. Dig.* 229 (2010).
6. E.A. Fitzgerald, Y.-H. Xie, M.L. Green, D. Brasen, A.R. Kortan, J. Michel, Y.-J. Mii, B.E. Weir, *Appl. Phys. Lett.* **59**, 811 (1991).
7. K. Rim, J. Welsler, J.L. Hoyt, J.F. Gibbons, *IEDM Tech. Dig.* 517 (1995).
8. B.H. Lee, A. Mocuta, S. Bedell, H. Chen, D. Sadana, K. Rim, P. O'Neil, R. Mo, K. Chan, C. Cabral, C. Lavoie, D. Mocuta, A. Chakravarti, R.M. Mitchell, J. Mezzapelle, F. Jamin, M. Sendelbach, H. Kermel, M. Gribelyuk, A. Domenicucci, K.A. Jenkins, S. Narasimha, S.H. Ku, M. Jeong, I.Y. Yang, E. Leobandung, P. Agnello, W. Haensch, J. Welsler, *IEDM Tech. Dig.* 946 (2002).
9. S.W. Bedell, K. Fogel, D.K. Sadana, H. Chen, *Appl. Phys. Lett.* **85**, 5869 (2004).
10. T. Ghani, M. Armstrong, C. Auth, C.M. Bost, P. Charvat, G. Glass, T. Hoffmann, K. Johnson, C. Kenyon, J. Klaus, B. McIntyre, K. Mistry, A. Murthy, J. Sandford, M. Silberstein, S. Sivakumar, P. Smith, K. Zawadzki, S. Thompson, M. Bohr, *IEDM Tech. Dig.* 978 (2003).
11. Y. Sun, S.E. Thompson, T. Nishida, *J. Appl. Phys.* **101**, 104503 (2007).
12. J. Wang, Y. Tateshita, S. Yamakawa, K. Nagano, T. Hirano, Y. Kikuchi, Y. Miyanami, S. Yamaguchi, K. Tai, R. Yamamoto, S. Kanda, T. Kimura, K. Kugimiya, M. Tsukamoto, H. Wakabayashi, Y. Tagawa, H. Iwamoto, T. Ohno, M. Saito, S. Kadamura, N. Nagashima, *Symp. VLSI Tech.* 46 (2007).
13. P. Packan, S. Akbar, M. Armstrong, D. Bergstrom, M. Brazier, H. Deshpande, K. Dev, G. Ding, T. Ghani, O. Golonzka, W. Han, J. He, R. Heussner, R. James, J. Jopling, C. Kenyon, S.-H. Lee, M. Liu, S. Lodha, B. Mattis, A. Murthy, L. Neiberg, J. Neiryneck, S. Pae, C. Parker, L. Pipes, J. Sebastian, J. Seiple, B. Sell, A. Sharma, S. Sivakumar, B. Song, A. St. Amour, K. Tone, T. Troeger, C. Weber, K. Zhang, Y. Luo, S. Natarajan, *IEDM Tech. Dig.* 659 (2009).
14. S. Narasimha, P. Chang, C. Ortolland, D. Fried, E. Engbrecht, K. Nummy, P. Parries, T. Ando, M. Aquilino, N. Arnold, R. Bolam, J. Cai, M. Chudzik, B. Cipriani, G. Costrini, M. Dai, J. Dechene, C. DeWan, B. Engel, M. Gribelyuk, D. Guo, G. Han, N. Habib, J. Holt, D. Ioannou, B. Jagannathan, D. Jaeger, J. Johnson, W. Kong, J. Koshy, R. Krishnan, A. Kumar, M. Kumar, J. Lee, X. Li, C. Lin, B. Linder, S. Lucarini, N. Lustig, P. McLaughlin, K. Onishi, V. Ontalus, R. Robison, C. Sheraw, M. Stoker, A. Thomas, G. Wang, R. Wise, L. Zhuang, G. Freeman, J. Gill, E. Maciejewski, R. Malik, J. Norum, P. Agnello, *IEDM Tech. Dig.* 52 (2012).
15. C. Auth, C. Allen, A. Blattner, D. Bergstrom, M. Brazier, M. Bost, M. Buehler, V. Chikarmane, T. Ghani, T. Glassman, R. Grover, W. Han, D. Hanken, M. Hattendorf, P. Hentges, R. Heussner, J. Hicks, D. Ingerly, P. Jain, S. Jaloviar, R. James, D. Jones, J. Jopling, S. Joshi, C. Kenyon, H. Liu, R. McFadden, B. McIntyre, J. Neiryneck, C. Parker, L. Pipes, I. Post, S. Pradhan, M. Prince, S. Ramey, T. Reynolds, J. Roesler, J. Sandford, J. Seiple, P. Smith, C. Thomas, D. Towner, T. Troeger, C. Weber, P. Yashar, K. Zawadzki, K. Mistry, *Symp. VLSI Tech.* 131–132 (2012).
16. H. Yin, R. Huang, K.D. Hobart, Z. Suo, T.S. Kuan, C.K. Inoki, S.R. Shieh, T.S. Duffy, F.J. Kub, J.C. Sturm, *J. Appl. Phys.* **91**, 9716 (2002).
17. H. Yin, K.D. Hobart, F.J. Kub, S.R. Shieh, T.S. Duffy, J.C. Sturm, *Appl. Phys. Lett.* **84**, 3624 (2004).
18. A. Domenicucci, S. Bedell, R. Roy, D.K. Sadana, A. Mocuta, in *Proceedings of the 14th Conference of Microscopy of Semiconducting Materials*, A.G. Cullis, J.L. Hutchinson, Eds. (Oxford, UK, 2005), vol. 107, p. 89.
19. T. Irisawa, T. Numata, T. Tezuka, K. Usuda, N. Hiroshita, N. Sugiyama, *VLSI Symp. Tech. Dig.* 178 (2005).
20. S.W. Bedell, N. Daval, A. Khakifirooz, P. Kulkarni, K. Fogel, A. Domenicucci, D.K. Sadana, *Microelectron. Eng.* **88**, 324 (2011).
21. W. Xiong, C.R. Cleavelin, P. Kohli, C. Huffman, T. Schulz, K. Schrufer, G. Gebara, K. Mathews, P. Patruno, Y.-M. Le Vaillant, I. Cayrefourcq, M. Kennard, C. Mazure, K. Shin, T.-J.K. Liu, *IEEE Electron Device Lett.* **27** (7), 612 (2006).
22. A. Khakifirooz, K. Cheng, T. Nagumo, N. Loubet, T. Adam, A. Reznicek, J. Kuss, D. Shahrjerdi, R. Sreenivasan, S. Ponoht, H. He, P. Kulkarni, Q. Liu, P. Hashemi, P. Khare, S. Luning, S. Mehta, J. Gimbert, Y. Zhu, Z. Zhu, J. Li, A. Madan, T. Levin, F. Monsieur, T. Yamamoto, S. Naczas, S. Schmitz, S. Holmes, C. Aulnette, N. Daval, W. Schwarzenbach, B.-Y. Nguyen, V. Paruchuri, M. Khare, G. Shahidi, B. Doris, *Symp. VLSI Tech.* 117 (2012).
23. A. Khakifirooz, R. Sreenivasan, B.N. Taber, F. Allibert, P. Hashemi, W. Chern, N. Xu, E.C. Wall, S. Mochizuki, J. Li, Y. Yin, N. Loubet, A. Reznicek, S.M. Mignot, D. Lu, H. He, T. Yamashita, P. Morin, G. Tsutsui, C.-Y. Chen, V.S. Basker, T.E. Standaert, K. Cheng, T. Levin, B.Y. Nguyen, T.-J. King Liu, D. Guo, H. Bu, K. Rim, B. Doris, paper presented at IEEE S3S Conference, Monterey, CA, 7–10 October, 2013.
24. K. Cheng, A. Khakifirooz, N. Loubet, S. Luning, T. Nagumo, M. Vinet, Q. Liu, A. Reznicek, T. Adam, S. Naczas, P. Hashemi, J. Kuss, J. Li, H. He, L. Edge, J. Gimbert, P. Khare, Y. Zhu, Z. Zhu, A. Madan, N. Klymko, S. Holmes, T.M. Levin, A. Hubbard, R. Johnson, M. Terrizzi, S. Teehan, A. Upham, G. Pfeiffer, T. Wu, A. Inada, F. Allibert, B. Nguyen, L. Grenouillet, Y. Le Tiec, R. Wacquez, W. Kleemeier, R. Sampson, R.H. Dennard, T.H. Ning, M. Khare, G. Shahidi, B. Doris, *IEDM Tech. Dig.* 420 (2012).
25. L. Chang, D.J. Frank, R.K. Montoye, S.J. Koester, B.L. Ji, P.W. Coteus, R.H. Dennard, W. Haensch, *Proc. IEEE* **98** (2), 215 (2010).
26. S. Suthram, M.M. Hussain, H.R. Harris, C. Smith, H.-H. Tseng, R. Jammy, S.E. Thompson, *IEEE Electron Device Lett.* **29** (5), 480 (2008).
27. N. Xu, B. Ho, M. Choi, V. Moroz, T.-J. King Liu, *IEEE Trans. Electron Devices* **59** (6), 1592 (2012).
28. M. Saitoh, A. Kaneko, K. Okano, T. Kinoshita, S. Inaba, Y. Toyoshima, K. Uchida, *Symp. VLSI Tech.* 18 (2008).
29. S. Mujumdar, K. Maitra, S. Datta, *IEEE Trans. Electron Devices* **59** (1), 72 (2012).
30. A. Nainani, S. Gupta, V. Moroz, C. Munkang, K. Yihwan, Y. Cho, J. Gelatos, T. Mandekar, A. Brand, P. Er-Xuan, M.C. Abraham, K. Schuegraf, *IEDM Tech. Dig.* 427 (2012).
31. M. Choi, V. Moroz, L. Smith, O. Penzin, in *6th International Silicon-Germanium Technology and Device Meeting* (2012 ISTDM).
32. C.Y. Kang, R. Choi, S.C. Song, K. Choi, B.S. Ju, M.M. Hussain, B.H. Lee, G. Bersuker, C. Young, D. Heh, P. Kirsch, J. Barnett, J.-W. Yang, W. Xiong, H. Tseng, R. Jammy, *IEDM Tech. Dig.* 885 (2006).
33. I. Ok, K. Akarvardar, S. Lin, M. Baykan, C.D. Young, P.Y. Hung, M.P. Rodgers, S. Bennett, H.O. Stamper, D.L. Franca, J. Yum, J.P. Nadeau, C. Hobbs, P. Kirsch, P. Majhi, R. Jammy, *IEDM Tech. Dig.* 776 (2010).
34. R. Droopad, K. Rajagopalan, J. Abrokwha, M. Canonico, M. Passlack, *Solid State Electron.* **50**, 1175 (2006).
35. D. Kim, PhD thesis, Stanford University (2009).
36. A. Nainani, R. Shyam, D. Witte, M. Kobayashi, T. Irisawa, T. Krishnamohan, K. Saraswat, B.R. Bennett, M.G. Ancona, J.B. Boos, *IEDM Tech. Dig.* 857 (2009).
37. T. Kaneko, H. Asahi, Y. Okuno, S.-I. Gonda, *J. Cryst. Growth* **95**, 158 (1989).
38. S.H. Kim, M. Yokoyama, R. Nakane, O. Ichikawa, T. Osada, M. Hata, M. Takenaka, S. Takagi, *Symp. VLSI Tech.* T51 (2013). □

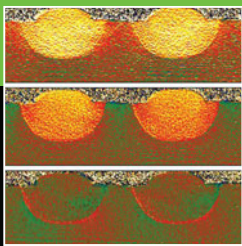


2014 MRS[®]
SPRING MEETING & EXHIBIT

April 21-25, 2014 | San Francisco, CA

Register by 5:00 pm (ET)
April 4, 2014 and Save!

www.mrs.org/spring2014



Observing and measuring strain in nanostructures and devices with transmission electron microscopy

Martin J. Hÿtch and Andrew M. Minor

The evolution of elastic strain engineering in nanostructures and devices requires characterization tools that can be used to not only observe but also quantify the actual strain in a sample, whether this strain is intrinsic or applied. Strain contrast in crystalline samples has always been one of the primary contrast mechanisms used for imaging the microstructure of a material in a transmission electron microscope (TEM). In this regard, TEM is a particularly powerful tool due to its ability to spatially resolve strain information with high precision and spatial resolution. This article reviews the techniques currently available for directly measuring strain in the TEM. Examples are given for measuring strain in semiconductor devices using imaging, diffraction, and holographic techniques. For strain measurement during *in situ* mechanical testing, two general methods are presented: the conversion of displacement from an actuation device or the direct measurement of strain using image features during deformation.

Introduction

Strain is a key parameter for understanding many physical phenomena at the nanoscale. The mechanical and electronic properties of a material are directly related to the strain in the material, and the response of a material to an applied strain is fundamental to the engineering of mechanical or electronic properties. Strain fields in materials have always been one of the main contrast mechanisms in a transmission electron microscope (TEM), generating contrast by altering the diffracting conditions around a defect, for example. In recent years, TEM methods have been used and developed specifically to study strain fields, either to measure strain directly or to apply strains and observe the evolution of materials *in situ*. This article will review the current state of the art in this field. The first part will concentrate on the measurement of strain from imaging and diffraction, and the second on the quantitative measurement of strain during *in situ* experiments.

The concept of elastic strain engineering for electronic properties came originally from the field of microelectronics, and naturally many of the examples will be taken from this area. By straining silicon, the mobility of carriers can be increased significantly. Engineering strain in the active region of transistors has been, and continues to be, essential in helping the industry upgrade performance year after year. Different

methods have been employed to inject strain into the channel region of devices, including recessed sources and drains of alloys of silicon and stress liners.¹ The complex geometry of devices also leads to non-uniform strain distributions. It is therefore important to be able to measure the strain at a very local level and ideally to be able to map the strain over the whole device.

It is also important to understand that the physical phenomena of interest, such as stress, piezoresistivity, and piezoelectricity, are all related by tensor relations, which means that there is a complex interplay between the components in the different directions of the crystal.² Stress, for example, does not depend uniquely on the strain in one particular direction:

$$\sigma_{ij} = c_{ijkl}\epsilon_{kl}, \quad (1)$$

where σ_{ij} are the stress components, c_{ijkl} are the constants of elasticity, and ϵ_{kl} are the different strain components. To determine stress from strain, it is therefore necessary to measure all the strain components. Naturally, the most significant contribution for the σ_{xx} stress component is ϵ_{xxx} but not uniquely so. The same goes for mobility and the piezoelectric effect; even mobility is affected by shear components.

A distinction needs to be made between strain, which has a mechanical sense in Equation 1, and deformation. Mechanical strain is defined with respect to the relaxed, unstrained state of the material. TEM techniques, on the other hand, measure the change in local lattice parameter and orientation of the lattice planes with respect to some reference material, usually the substrate or an undeformed part of the material. A deformed sample can have both regions of elastic (recoverable) strain as well as inelastic strain. TEM contrast also arises from a local change in the chemical composition. Without knowing the local composition, it is therefore not possible to determine the local mechanical strain. This also motivates *in situ* experiments, where the sample can be loaded within the microscope, thus providing knowledge of both the undeformed and deformed states.

Strain measurements by transmission electron microscopy

Four main TEM techniques have been developed to measure strain and will be described in this article: convergent-beam electron diffraction (CBED),^{3,4} nano-beam electron diffraction (NBED),^{5,6} high-resolution TEM (HRTEM),^{7,8} and dark-field electron holography (DFEH).^{9,10} In addition, *in situ* mechanical testing techniques have been developed to measure both applied and local strains. They can be diffraction or image based. A change in the lattice parameter will change the diffraction angle. At their most basic level, diffraction techniques, such as NBED, are based on measuring the displacement of the diffraction spots. Imaging techniques rely on quantifying the displacement of atomic columns from micrographs obtained via HRTEM or high-angle annular dark-field scanning TEM (HAADF-STEM), or by directly mapping the distortion of a sample with digital image correlation (DIC). These are then related to strain by taking the spatial derivatives. Diffraction is therefore a direct measurement of strain and imaging techniques of displacements.

There also exist hybrid techniques that are a mix of diffraction and imaging based on imaging a particular diffracted beam in dark-field mode, either to map its intensity, as in conventional TEM, or its phase through DFEH. Unlike the intensity of a diffracted beam, the phase can be related directly to the strain, or more precisely to the displacement field, through the following relation:

$$\varphi_g^G = -2\pi\mathbf{g}\cdot\mathbf{u}, \quad (2)$$

where φ_g^G is the so-called geometric phase of the diffracted beam, \mathbf{g} is the corresponding reciprocal lattice vector, and \mathbf{u} is the local displacement vector.¹¹

It should be noted that displacements can only be measured in the direction of the reciprocal lattice vector of the diffracted beam in question. This is general to all TEM techniques, diffraction and imaging, and excludes measurement of strain in the direction of propagation of the beam except for CBED, which makes use of diffraction to high-order Laue zones (HOLZ).

Specimen preparation and thin-film relaxation

A common feature of TEM techniques is that the specimen needs to be thinned to become sufficiently transparent to electrons, typically to the order of 100 nm for silicon. This means that TEM specimen preparation techniques are necessarily destructive, unless the original object was of these dimensions (such as a nanocrystal). Second, the sample studied will not be in the same strain-state as the original “bulk” material. The two new surfaces of the thin lamella allow for relaxation of stress and are commonly referred to as the “thin-film effect.”¹² In addition, the method of specimen thinning itself (ion-beam or mechanical polishing) may also modify strain in the sample. Every effort is generally made to reduce these phenomena, but the thin-film effect is inherent and cannot be avoided. In general, imaging techniques, which can use thicker specimens, are preferred, and measurements need to be compared with modeling to evaluate the corrections to be applied to the measured data.

For studying devices, focused ion beam (FIB) is the required technique for specimen preparation because of its site specificity. It also has the advantage of providing samples of uniform (and specified) thickness. However, obtaining thicknesses under 100 nm through FIB preparation is demanding, and care needs to be taken to protect surfaces and limit the amorphous surface layers caused by ion milling. Specimen geometry considerations for *in situ* tests will be described later.

The projection problem, dynamic scattering, and imaging aberrations

The position of the diffracted spot in a diffraction pattern can be related directly by the Bragg law to the local spacing of the atomic lattice, which is simplistic. Similarly, directly relating the lattice fringes in a HRTEM image to the position of the atomic lattice is problematic.

First, there is the projection problem: in TEM, the fast electron travels through a three-dimensional sample to produce two-dimensional information. For example, specimens are never uniformly strained along the viewing direction. This is a direct result of the thin-film effect mentioned previously. Therefore, the strain measured at a particular point on the specimen, viewed in projection, is some average over the thickness of the sample.¹³ If electron scattering was kinematical, the result would be the linear average, but electron scattering is highly dynamical, and multiple scattering events occur. Effects are particularly pronounced at interfaces between materials where strain gradients are high.

Second, electron diffraction does not occur only at the Bragg angle due to the thinness of the specimens or through dynamical scattering.¹⁴ A certain spread of scattering angles, therefore, is always present. Again, the average scattering angle does not always coincide exactly with the reciprocal lattice vector of the atomic lattice that we wish to measure.

Finally, the strain in the samples is never uniform across the field of view. A measurement is always a local average

Table I. Comparison of transmission electron microscopy strain measurement techniques.

	Mode	Precision	Spatial Resolution	Field of View
CBED	Probe	2×10^{-4}	0.5–2 nm	n.a.
NBED	Probe	10^{-3}	5–10 nm	n.a.
HR(S)TEM	Image	10^{-3}	1–2 nm	150 × 150 nm
DFEH	Image	2×10^{-4}	2–4 nm	1500 × 500 nm

CBED, convergent-beam electron diffraction; NBED, nano-beam electron diffraction; HR(S)TEM, high-resolution (scanning) TEM; DFEH, dark-field electron holography.

spatially, and not always a simple one. The most striking case is for HRTEM imaging.¹⁵ Lenses are not perfect, even in the age of aberration correction. There are therefore slight shifts between the image of the atomic lattice and its actual position.¹⁶ Indeed, the position of neighboring atomic columns can even influence the apparent position of the atomic column of interest.

Precision, accuracy, and spatial resolution

The precision and accuracy of strain measurements depend on their spatial resolution (**Table I**). In general, the higher the spatial resolution, the less accurate the technique. Measuring the strain, atom column by atom column at an interface, is not the same as measuring strain broadly over a few nanometers in a more uniform region of the specimen. High strain gradients mean lower precision and accuracy. Similarly, the thickness of the sample should be as uniform as possible. It all comes down to the required level of accuracy.

Diffraction-based TEM methods

Convergent-beam electron diffraction

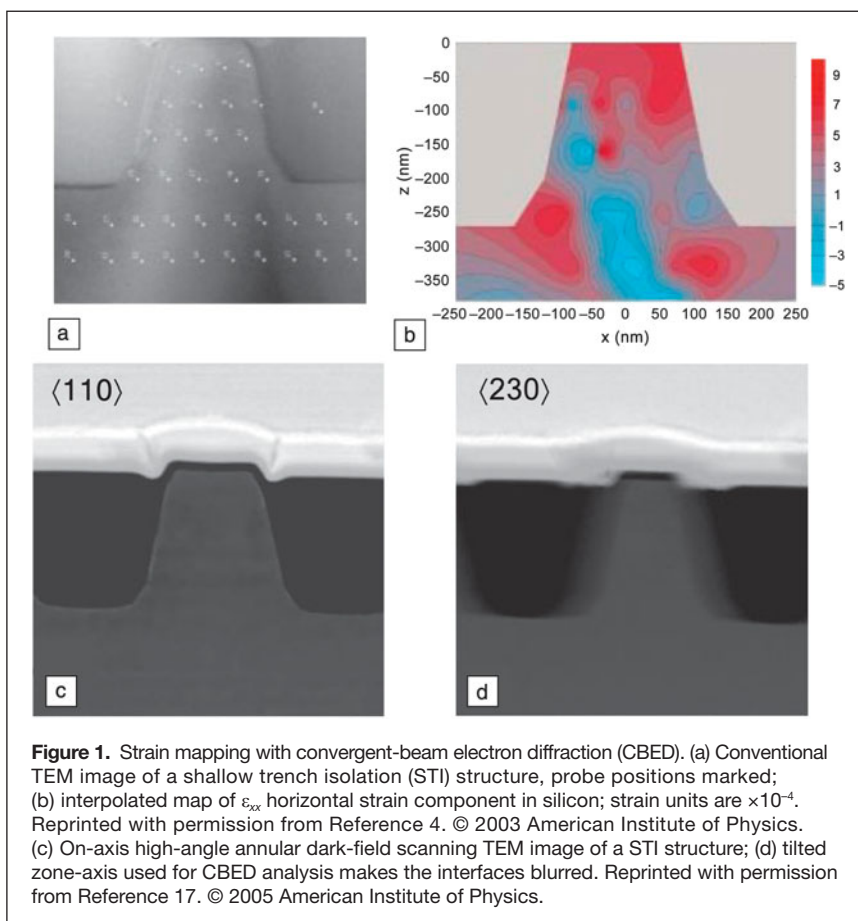
Historically, CBED was the first TEM technique to be used to measure strain in nanostructures. As the name suggests, the beam is focused into a spot, as small as one or two nanometers, onto the specimen. The diffraction pattern is then formed of large disks representing the intensity at different angles of incidence represented by the probe. Within the transmitted disk, dark HOLZ lines can be seen that represent the scattering to HOLZ. Strain, or more generally speaking, lattice parameters are measured from the shift of the positions of these lines.³

The larger the scattering angle, the higher the sensitivity to strain. CBED, which uses HOLZ lines, is therefore extremely sensitive to strain, typically on the order of 10^{-4} . By scanning the probe over the sample, a map can be obtained (see **Figure 1a–b**).⁴ Nevertheless, to obtain sufficient HOLZ scattering, the crystal needs to be oriented into

a relatively high-order zone axis. Structures are usually grown at low-order zone axes, so interfaces can appear blurred, limiting the spatial resolution and interpretability of the results (see **Figure 1c–d**).¹⁷

It is also true that the high convergence angle and scattering angles mean that quite

a wide region of the specimen is actually sampled, despite the small size of the focused probe, further limiting the actual spatial resolution of the technique.¹⁸ But the real problem with CBED is that it is too sensitive to bending of the atomic columns. The relaxation of the thin film leads to splitting of the fine HOLZ lines.¹⁹ This phenomenon is now well-understood, but the simulations are cumbersome and require the exact knowledge of the geometry and the strain state of the sample, which is of course what we are trying to measure.²⁰ Nevertheless, the technique can work in symmetric positions on devices, like the center of a channel, where bending is minimized.^{21–24} In addition, large-angle CBED is a useful technique to visualize strain in a sample and can even be used quantitatively in certain cases, as demonstrated in **Figure 2**.²⁵



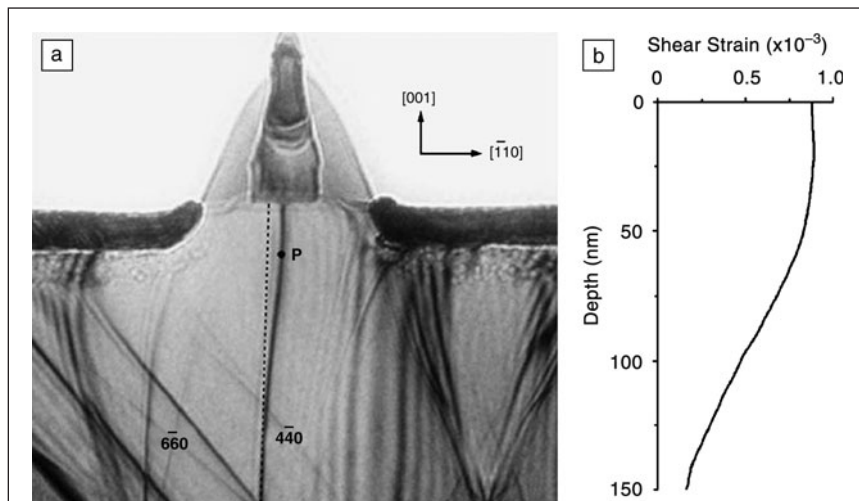


Figure 2. Large-angle convergent-beam electron diffraction pattern of a strained-silicon transistor. (a) Bending of the black 440 diffraction line in the channel is indicative of strain; (b) corresponding shear component, units of $\times 10^{-3}$. Reprinted with permission from Reference 25. © 2008 Elsevier.

Nano-beam electron diffraction

CBED was progressively abandoned in favor of the more widely applicable technique of NBED.⁹ The idea is to form a spot pattern from a small area on the sample (see **Figure 3**). First, a pattern is taken from a reference area of the sample, typically the substrate, and the spot positions are determined. Patterns are then taken successively from different areas, analyzed, and the spot positions are compared with the reference pattern.¹⁰ The shifts in the spot positions are then used to determine the deformation tensor at each of the probe positions.

The challenge was to be able to form narrow beams of relatively parallel illumination (convergence angle typically less than 0.5 mrad). This can be achieved with small objective apertures (1–10 microns), as originally shown in Reference 5, or illumination systems with three condenser lenses.²⁶ The accuracy and precision of the technique has been evaluated to be 10^{-3} strain resolution, and the advantages and disadvantages with respect to CBED are analyzed in Reference 27.

With NBED, a low-order zone axis can be used. The technique is conceptually simple and is less affected by bending of the atomic columns in regions of higher strain gradients than CBED. Dynamic scattering still limits the accuracy, and the precision is limited by an additional factor that is the size of the detector used. For example, a strain of 10^{-3} would represent only a shift of 1 pixel if the spots are spaced by 1000 pixels. Due to the current size of charge coupled devices, sub-pixel precision is required, which can prove problematic.

An alternative to measuring the position of the maximum intensity of the spot is to detect the position of the disks in the NBED patterns, since the convergence is quite high, on the order of 0.5 mrad,⁶ or indeed, to use highly convergent illumination in CBED configuration.²⁴ Another problem inherent to probe methods is knowing exactly where the NBED pattern (or CBED pattern) was taken with respect to the structure analyzed. This can be countered by simultaneously recording the HAADF-STEM image (Figure 3c).^{6,17} NBED has been successfully used to study a number of strained-silicon devices.^{28–30} NBED is usually carried out to create strain profiles, as two-dimensional mapping can be too time consuming.

Imaging techniques

Any technique that can create images of the atomic lattice can be used to measure strain, by HRTEM, or HAADF-STEM. The two main

techniques for measuring the positions of the lattice from the image are peak-finding⁷ and geometric phase analysis (GPA).⁸ Peak-finding, as its name suggests, relies on identifying the positions of intensity peaks related to the atomic column positions. Similar algorithms are used in identifying the spot positions in NBED. A region of substrate is identified as the reference region, and the displacement of the peaks with respect to this extended lattice defines the displacement field.

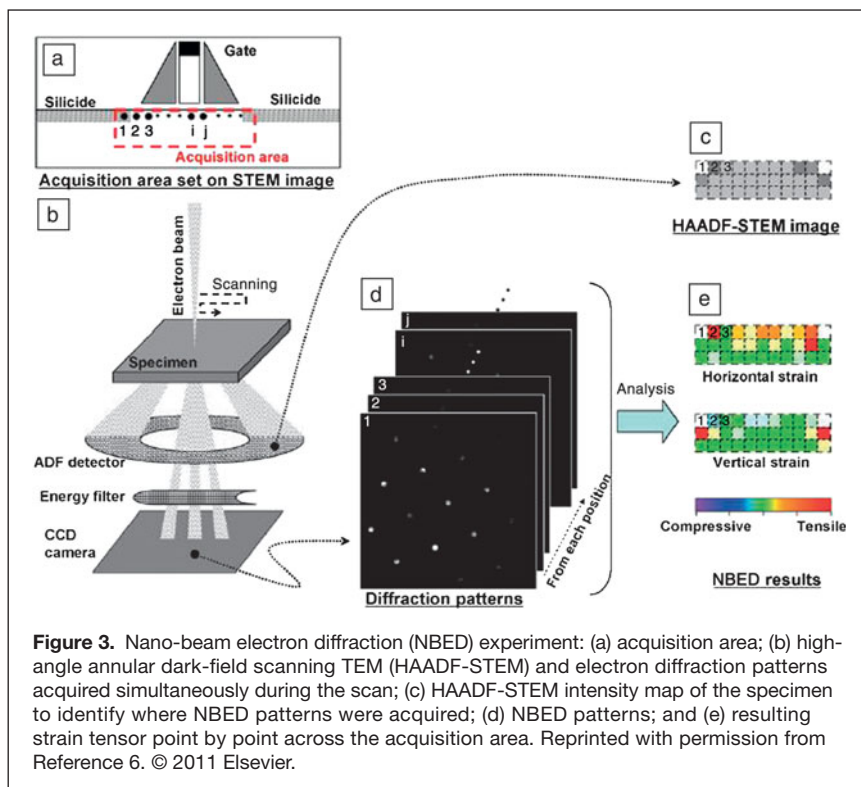


Figure 3. Nano-beam electron diffraction (NBED) experiment: (a) acquisition area; (b) high-angle annular dark-field scanning TEM (HAADF-STEM) and electron diffraction patterns acquired simultaneously during the scan; (c) HAADF-STEM intensity map of the specimen to identify where NBED patterns were acquired; (d) NBED patterns; and (e) resulting strain tensor point by point across the acquisition area. Reprinted with permission from Reference 6. © 2011 Elsevier.

GPA relies on determining the phase of periodicities in the image through Fourier filtering. The phase is related to the displacement field through Equation 2. The spatial resolution is determined by the size of the mask used in the filtering step of the process, with a maximum of two times the lattice spacing. Spatial resolution is typically 1–2 nm for a reasonable strain resolution of 10^{-3} .³¹

High-resolution transmission electron microscopy

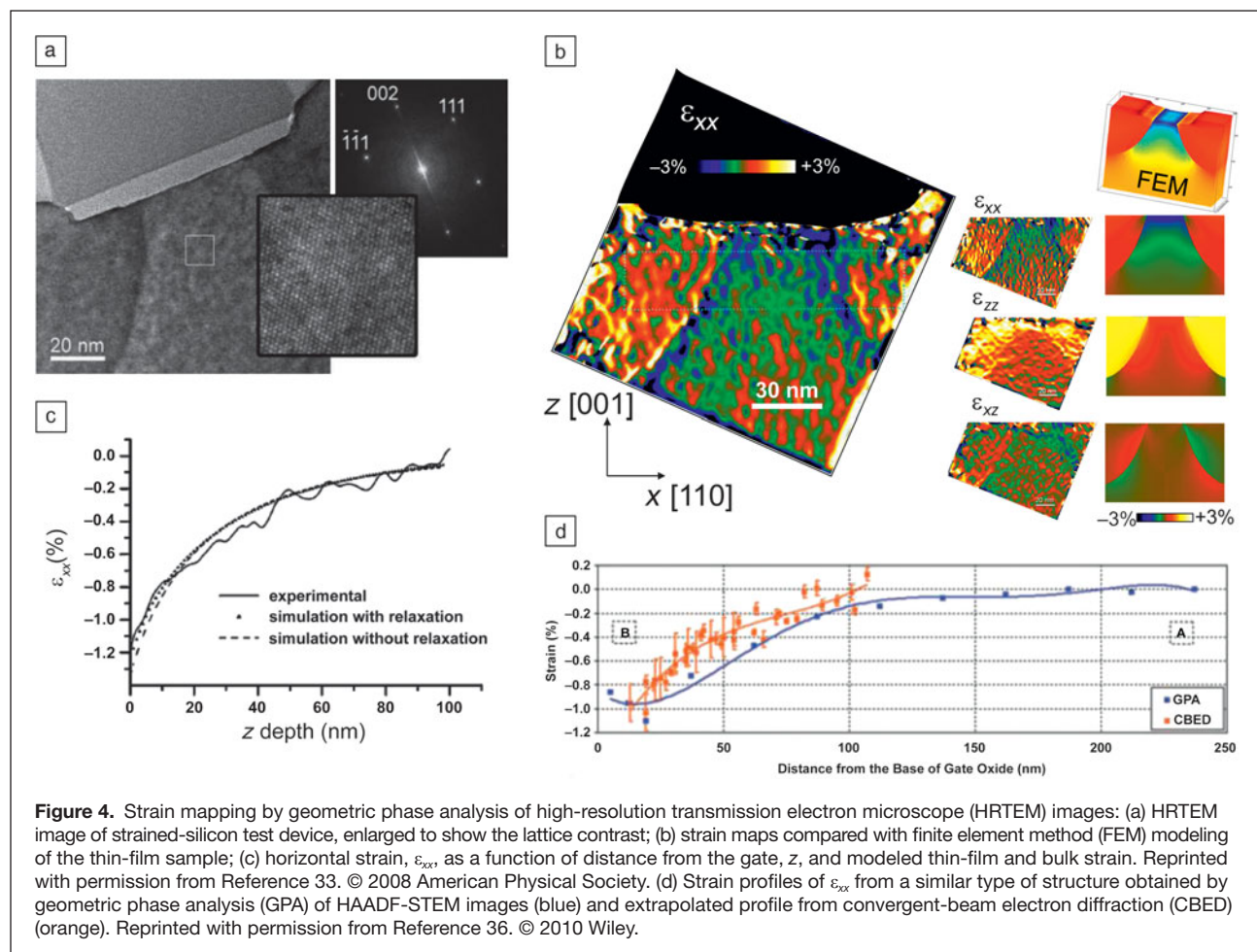
The first method used to study strained-silicon devices was analyzing the local fast Fourier transform in HRTEM images, analogous to NBED.³² Geometric phase analysis was subsequently used to map the different strain components over the active region of a strained-silicon transistor test structure (Figure 4).³³ The challenge was to obtain sufficient contrast from a FIB prepared specimen of about 100 nm in thickness, whereas HRTEM normally requires a foil thickness of less than 50 nm. In this case, aberration correction was used but is not strictly necessary.³⁴ According to the finite-element modeling method, the difference between the strain, ϵ_{xx} , in the relaxed TEM sample and the bulk structure is rather small (Figure 4c). This is generally the case for components parallel to the surface, which are constrained by the geometry of the

source and drain region. The largest relaxation is observed for the components in the growth direction, z , and can reach 20–30% of the value of the strain in extreme cases.

As an alternative to HRTEM, HAADF-STEM can be used.^{35,36} Thicker specimens can be used, but STEM images suffer from additional distortions from the scanning process itself that are difficult to correct. Both HRTEM and HAADF-STEM imaging suffer from relatively small fields of view partly from the limited size of detectors and the difficulties of obtaining uniform contrast over large areas. This means that the reference region is not always in a truly unstrained region of the device, as a comparison with CBED measurements reveals (Figure 4d).³⁶

Diffraction imaging in dark-field mode

Since the very beginning of TEM, the dark-field technique of imaging with a diffracted beam has allowed for the study of strain, in particular by revealing the presence of dislocations or precipitate strain fields. A common sign of strain in a sample is bend contours, which occur due to flexing of the sample. This phenomenon is described in any text book on conventional TEM (e.g., see Reference 37). For quantitative mapping of strain fields, the intensity of the diffracted beam can be fitted to dynamical scattering simulations based on finite-element



modeling of the strains.³⁸ The technique, called quantitative electron diffraction contrast, suffers from heavy reliance on modeling, specimen bending, and the nonlinear relationship between strain and diffracted intensity.

Dark-field electron holography

DFEH is the most recent of the TEM techniques presented here and was developed to map strain by directly measuring the phase of diffracted beams.^{9,10} The phase of the diffracted beam is related to the strain, through Equation 2, and depends on other factors, such as the specimen thickness, the mean-inner potential of the material, and dynamic scattering.¹¹ It is therefore important to have specimens prepared with uniform specimen thickness and uniform diffraction conditions (i.e., without significant bending).

The setup for DFEH is similar to conventional off-axis electron holography, except that the experiment is carried out in dark-field mode (i.e., the diffracted beam is oriented along the optical axis by tilting the incident beam) (Figure 5). A part of the diffracted beam emerging from an unstrained part of the specimen, typically the substrate, is interfered with the beam emerging from the region of interest. With the precautions mentioned previously, the resulting phase difference is due only to strain. With DFEH, a much larger area can be mapped compared to HRTEM (Figure 6a–b), even up to several microns. By capturing the phase of two non-collinear diffracted beams, the two-dimensional strain tensor can be determined (Figure 6c).

While the technique was aimed at fairly low spatial resolutions, the technique can be pushed to a spatial resolution of 1 nm.^{39,40} The real limitations to spatial resolution are the approximations and assumptions underlying the method rather than instrumental. The precision can reach 2×10^{-4} in strain profiles if lateral averaging is applied.⁴¹ DFEH has found a number of applications, thanks to its mapping capability and precision.^{42–44} A brief review of different applications can

be found in Reference 13. In addition to using off-axis holographic techniques, dark-field inline holography (DFIH) is possible using variations in intensity of dark-field images with defocus. The results of DFIH are similar to off-axis techniques but with more relaxed requirements on the spatial coherence of the electron beam.⁴⁵

As mentioned in the introduction, the simple relation between the phase of the diffracted beam and the displacement field described by Equation 2 is not exact, notably due to the projection problem and dynamic scattering. However, analysis of the simple diffraction conditions relevant to DFEH has allowed an analytical formula for the projection rule and the averaging of strain over different depths in the thin foil to be determined.⁴⁶

In situ techniques for measuring strain

The basic mechanisms that determine materials deformation behavior occur at nanometer length scales, and the defects that control mechanical properties are best characterized through electron microscopy. Therefore, it is not surprising that mechanical testing methods were among the first *in situ* methods to be developed for the TEM.^{14,47} Starting in the late 1950s, *in situ* straining stages were developed for dynamic observations of dislocation motion in metals.⁴⁸ Throughout the last 50 years, there have been significant developments in the field of *in situ* TEM mechanical testing,⁴⁹ including the evolution of mechanical probing techniques such as *in situ* nanoindentation.⁵⁰ However, there is a large difference between deforming a sample *in situ* in a TEM and measuring the imposed strain in the material. In order to measure strain, it is necessary first and foremost to have an accurate measurement of the gauge section of the deforming volume, something that requires precise sample manufacturing. Thus it was not until recent developments in the field of microfabrication and FIB preparation that quantitative measurements of the actual strain imposed on a material during an *in situ* TEM mechanical test were routinely achieved.^{51,52} *In situ* TEM mechanical testing with quantitative force versus displacement measurements have been demonstrated using multiple testing configurations and types of samples, including nanoindentation, compression, tension, and bending, as described in a recent review article.⁵³

In general, there are two methods to measure strain during an *in situ* TEM mechanical test, either through measurement of the displacement imposed on the sample by the actuation device, or through direct visualization techniques using markers and DIC. In both cases, it is critical that the geometry of the deforming volume is well known. One method to know the sample geometry precisely is to use microfabrication, such as when a thin film of known thickness is deposited on a microfabricated structure.⁵⁴ By monitoring the

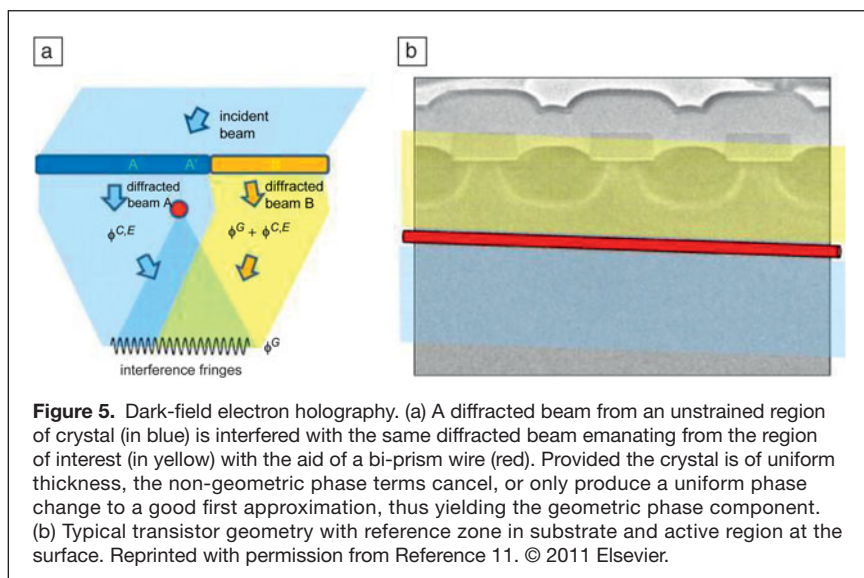
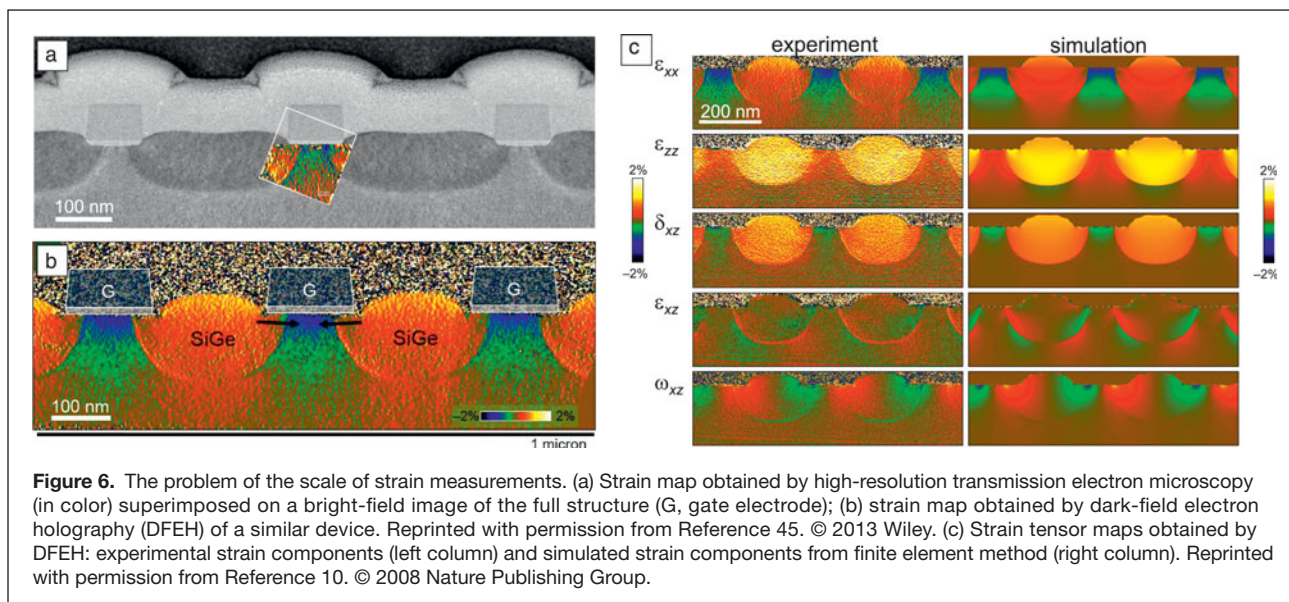


Figure 5. Dark-field electron holography. (a) A diffracted beam from an unstrained region of crystal (in blue) is interfered with the same diffracted beam emanating from the region of interest (in yellow) with the aid of a bi-prism wire (red). Provided the crystal is of uniform thickness, the non-geometric phase terms cancel, or only produce a uniform phase change to a good first approximation, thus yielding the geometric phase component. (b) Typical transistor geometry with reference zone in substrate and active region at the surface. Reprinted with permission from Reference 11. © 2011 Elsevier.



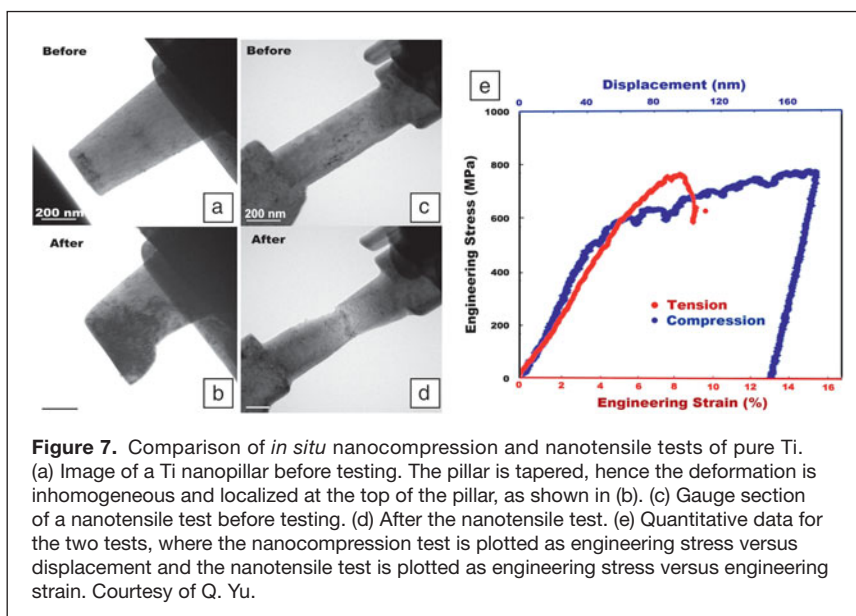
displacement in the device, one can obtain precise measurements of the strain applied to the suspended thin film. More recently, FIB microfabrication of TEM test samples has been shown to be a more generally applicable method to prepare precise sample geometries.

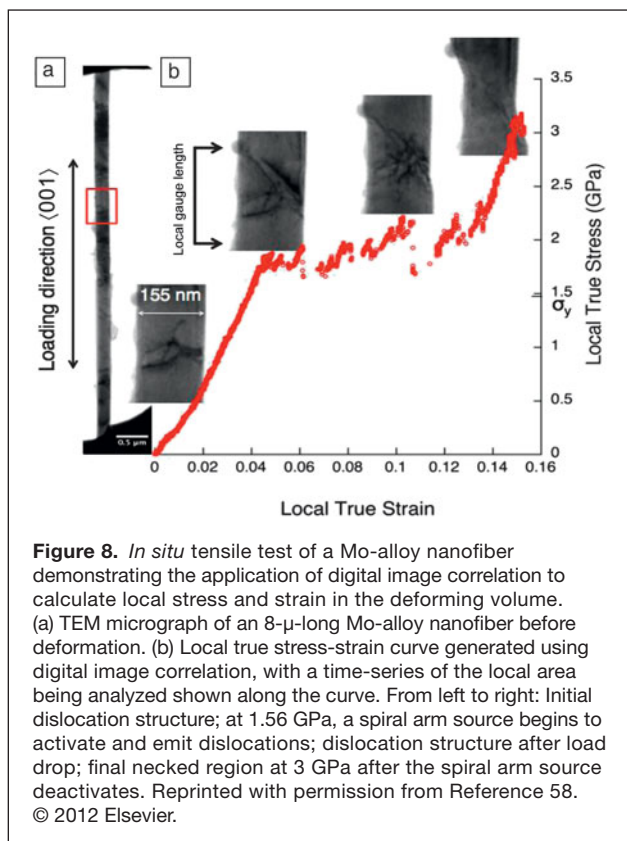
Using FIB, it is possible to prepare nanopillars where the cross-section of the sample is easily measured, although achieving a uniform cross-section throughout a pillar is not easy at small scales. As a further extension of FIB preparation of mechanical test samples, it has been recently shown that *in situ* TEM tensile testing can be achieved by milling a dog-bone-shaped sample out of a bulk material with a FIB and also milling an inverted diamond gripper to pull the sample.⁵⁵ Through this method, uniaxial quantitative tensile testing is possible. Tensile tests have numerous advantages over compression testing, including decreased specimen taper, increased flexibility in sample geometry, and a homogeneously deforming gauge section.

Figure 7 shows a comparison of a nanocompression and nanotensile test of a FIB-prepared Ti sample. As shown in Figure 7a–b, the nanocompression test resulted in a relatively non-uniform deformation at the top of the pillar. In this case, it is difficult to describe the strain in the sample since the initial length of the sample is not an accurate estimation of the length of the deforming volume. Figure 7c–d shows the results of a nanotensile test on the same sample, where more homogeneous deformation across the gauge length of the sample makes the initial sample length more precise for strain measurement. Figure 7e shows the resulting quantitative data for both tests, where the nanocompression test is most accurately represented by engineering stress

versus displacement of the compression device, while the nanotensile test can accurately plot engineering stress versus engineering strain. In the case of the nanocompression test, the engineering stress is calculated using the contact area, whereas the engineering stress in the nanotensile test can be calculated using the uniform gauge area of the sample and assuming homogeneous deformation, which until necking occurs is a reasonable approximation.

The second general method of measuring strain during *in situ* testing is to rely on analysis of images using DIC. The DIC technique uses post-experiment image processing to measure the displacement between features such as FIB-deposited markers.^{56,57} In the example shown in **Figure 8**, an 8- μm -long Mo-alloy nanofiber of known geometry is pulled in tension using a microfabricated “push-to-pull” device and





an *in situ* TEM nanoindentation system.⁵⁸ Since the sample geometry is known and the instrumented nanoindenter can provide calibrated displacement during the test, the strain of the nanowire can be calculated directly, similar to the FIB-prepared nanotensile test in Figure 7. However, during the test, it was observed that the actual deformation in the sample was highly localized, and therefore the strain calculation for the entire 8- μ m-long nanofiber does not give an accurate representation of the strain in the actively deforming region of the sample, which is only a few hundred nanometers in length. Therefore, DIC was applied to the still frames extracted from the recorded videos to measure the local instantaneous projected area and the local elongation of the sample. Figure 8b shows the local true stress-strain curve for the necking region, as calculated using DIC with images of the fiber at notable points overlaid on the curve. By calculating the strain directly from the TEM images, it is possible to get a much more accurate measurement and actually report that the sample shows an increase in strength as the dislocation source is exhausted (the source stops emitting dislocations to carry the strain).⁵⁸ Without the DIC calibration of the local strain, the local hardening of the sample would go unnoticed in a stress-strain curve of the entire nanofiber.

Summary

Within the context of semiconductor devices, nano-beam electron diffraction (NBED) and dark-field electron holography (DFEH) are the most commonly used techniques today for

measuring strain. In a wider context, high-resolution transmission electron microscope (HRTEM) is the most used technique because of its availability. Convergent-beam electron diffraction (CBED) is used for more specialized case studies or as a benchmark for other techniques. A brief summary of the different techniques can be found later in the text (and see Table I).

CBED is still probably the most accurate technique for measuring strain in samples with small strain gradients. Otherwise, line splitting causes the analysis to be too complicated for practical use. Thick samples can be used for CBED, and it is the only technique providing information on the three-dimensional strain components, notably those in the incident beam direction. NBED is a practical and versatile technique that is conceptually simple but with sensitivity limited to about 10^{-3} . Some specialized instrumentation is required, including small objective apertures or three condenser lenses. HRTEM, whether in TEM or STEM mode, offers the possibility of strain mapping with precision similar to NBED but requires demanding specimen preparation and is limited in field of view. In principle, any high-resolution image can be analyzed for strain. DFEH is capable of mapping strain over micron fields of view with a precision similar to CBED of 10^{-4} . However, dedicated equipment is required, notably an electrostatic bi-prism, and operators need to be trained in electron holography, which has slowed wider usage of the technique.

In situ TEM mechanical testing can report accurate values of strain, but the key experimental parameters rely on precise knowledge of the dimensions of the deforming gauge section of the sample. There are two general methods to report strain from an *in situ* test: (1) conversion of displacement of the actuating mechanism to strain through knowledge of the sample geometry or (2) direct imaging techniques such as digital image correlation.

Acknowledgments

M.J.H. acknowledges financial support from the European Union under the Seventh Framework Programme under a contract for an Integrated Infrastructure Initiative Reference 312483-ESTEEM2 and the European Metrology Research Programme (EMRP) Project IND54 Nanostrain. The EMRP is jointly funded by the EMRP participating countries within EURAMET and the European Union. A.M.M. acknowledges support from the National Center for Electron Microscopy, Lawrence Berkeley National Laboratory, which is supported by the US Department of Energy under Contract #DE-AC02-05CH11231.

References

1. S.E. Thomson, M. Armstrong, C. Auth, M. Alavi, M. Buehler et al. *IEEE Trans. Electron Devices* **51**, 1790 (2004).
2. J.F. Nye, *Physical Properties of Crystals: Their Representation by Tensors and Matrices* (Oxford University Press, Oxford, 1985).
3. P.M. Jones, G.M. Rackham, J.W. Steeds, *Proc. R. Soc. London, Ser. A* **354**, 197 (1977).
4. A. Armigliato, R. Balboni, G.P. Carnevale, G. Pavia, D. Piccolo, S. Frabboni, A. Benedetti, A.G. Cullis, *Appl. Phys. Lett.* **82**, 2172 (2003).

5. K. Usuda, T. Numata, T. Irisawa, N. Hirashita, S. Takagi, *Mater. Sci. Eng.*, **B 124–125**, 143 (2005).
6. F. Uesugi, A. Hokazono, S. Takeno, *Ultramicroscopy* **111**, 995 (2011).
7. R. Bierwolf, M. Hohenstein, F. Philipp, O. Brandt, G.E. Crook, K. Ploog, *Ultramicroscopy* **49**, 273 (1993).
8. M.J. Hÿtch, E. Snoeck, R. Kilaas, *Ultramicroscopy* **74**, 131 (1998).
9. M.J. Hÿtch, E. Snoeck, F. Houdellier, F. Hÿe, US Patent 8502143 (August 6, 2013).
10. M.J. Hÿtch, F. Houdellier, F. Hÿe, E. Snoeck, *Nature* **453**, 1086 (2008).
11. M.J. Hÿtch, F. Houdellier, F. Hÿe, E. Snoeck, *Ultramicroscopy* **111**, 1328 (2011).
12. J.M. Gibson, M.M.J. Treacy, *Ultramicroscopy* **14**, 345 (1984).
13. A. Lubk, E. Javon, N. Cherkashin, S. Reboh, C. Gatel, M.J. Hÿtch, *Ultramicroscopy* **136**, 42 (2014).
14. P. Hirsch, A. Howie, R. Nicholson, D.W. Pashley, M.J. Whelan, *Electron Microscopy of Thin Crystals* (Krieger Publishing, Malabar, 1965).
15. J.C.H. Spence, *High-Resolution Electron Microscopy* (Oxford University Press, Oxford, Ed. **3**, 2003).
16. M. J. Hÿtch, T. Plamann, *Ultramicroscopy* **87**, 199 (2001).
17. A. Armigliato, R. Balboni, S. Frabboni, *Appl. Phys. Lett.* **86**, 063508 (2005).
18. A. Chuvilin, U. Kaiser, *Ultramicroscopy* **104**, 73 (2005).
19. L. Cl  ment, R. Pantel, L.F.T. Kwakman, J.-L. Rouvi  re, *Appl. Phys. Lett.* **85**, 651 (2004).
20. F. Houdellier, C. Roucau, L. Cl  ment, J.L. Rouvi  re, M.J. Casanove, *Ultramicroscopy* **106**, 951 (2006).
21. J. Huang, M.J. Kima, P.R. Chidambaram, R.B. Irwin, P.J. Jones, J.W. Weijtjans, E.M. Koontz, Y.G. Wang, S. Tang, R. Wise, *Appl. Phys. Lett.* **89**, 063114 (2006).
22. P. Zhang, A.A. Istratov, E.R. Weber, C. Kisielowski, H. He, C. Nelson, J.C.H. Spence, *Appl. Phys. Lett.* **89**, 161907 (2006).
23. W. Zhao, G. Duscher, G. Rozgonyi, M.A. Zikry, S. Chopra, M.C. Ozturk, *Appl. Phys. Lett.* **90**, 191907 (2007).
24. K. M  ller, A. Rosenauer, M. Schowalter, J. Zweck, R. Fritz, K. Volz, *Microsc. Microanal.* **18**, 995 (2012).
25. H.H. Liu, X.F. Duan, Q. Xu, B.-G. Liu, *Ultramicroscopy* **108**, 816 (2008).
26. A. B  ch  , J.-L. Rouvi  re, L. Cl  ment, J.M. Hartmann, *Appl. Phys. Lett.* **95**, 123114 (2009).
27. A. Armigliato, S. Frabboni, G.C. Gazzadi, *Appl. Phys. Lett.* **93**, 161906 (2008).
28. J.P. Liu, K. Li, S.M. Pandey, F.L. Benistant, A. See, M.S. Zhou, L.C. Hsia, R. Schampers, D.O. Klenov, *Appl. Phys. Lett.* **93**, 221912 (2008).
29. S.W. Kim, J.-H. Yoo, S.-M. Koo, D.-H. Ko, H.-J. Lee, *Appl. Phys. Lett.* **99**, 133107 (2011).
30. T. Sato, H. Matsumoto, K. Nakano, M. Konno, M. Fukui, I. Nagaoki, Y. Taniguchi, *J. Phys. Conf. Ser.* **241**, 012014 (2010).
31. M.J. Hÿtch, J.-L. Putaux, J.-M. P  nissou, *Nature* **423**, 270 (2003).
32. K.-W. Ang, K.-J. Chui, V. Bliznetsov, C.-H. Tung, A. Du, N. Balasubramanian, G. Samudra, M.F. Li, Y.-C. Yeo, *Appl. Phys. Lett.* **86**, 093102 (2005).
33. F. Hÿe, M.J. Hÿtch, H. Bender, F. Houdellier, A. Claverie, *Phys. Rev. Lett.* **100**, 156602 (2008).
34. J.H. Chung, G.D. Lian, L. Rabenberg, *Appl. Phys. Lett.* **93**, 081909 (2008).
35. J.H. Chung, G.D. Lian, L. Rabenberg, *IEEE Electron Device Lett.* **31**, 854 (2010).
36. D. Diercks, G. Lian, J. Chung, M. Kaufman, *J. Microsc.* **241**, 195 (2010).
37. M. de Graef, *Introduction to Conventional Transmission Electron Microscopy* (Cambridge University Press, Cambridge, 2003).
38. J. Demarest, R. Hull, S.T. Schonenberg, K.G.F. Janssens, *Appl. Phys. Lett.* **77**, 412 (2000).
39. D. Cooper, J.-L. Rouvi  re, A. B  ch  , S. Kadkhodazadeh, E.S. Semenova, K. Yvind, R.E. Dunin-Borkowski, *Appl. Phys. Lett.* **99**, 261911 (2011).
40. Y.Y. Wang, J. Bruley, H. van Meer, J. Li, A. Domenicucci, C.E. Murray, J. Rouvi  re, *Appl. Phys. Lett.* **103**, 052104 (2013).
41. F. Hÿe, M.J. Hÿtch, F. Houdellier, H. Bender, A. Claverie, *Appl. Phys. Lett.* **95**, 073103 (2009).
42. D. Cooper, A. B  ch  , J.-M. Hartmann, V. Carron, J.-L. Rouvi  re, *Appl. Phys. Lett.* **96**, 113508 (2010).
43. T. Denneulin, D. Cooper, J.-M. Hartmann, J.-L. Rouvi  re, *J. Appl. Phys.* **112**, 094314 (2012).
44. Z.F. Wang, Y. Yao, X.Q. He, Y. Yang, L. Gu, Y.G. Wang, X.F. Duan, *Mater. Trans.* **53**, 2019 (2012).
45. M.J. Hÿtch, F. Houdellier, N. Cherkashin, S. Reboh, E. Javon, P. Benzo, C. Gatel, E. Snoeck, A. Claverie, in *Transmission Electron Microscopy in Micro-Nanoelectronics*, A. Claverie, Ed. (Wiley, London, 2013), C. **4**, pp. 81–106.
46. C.T. Koch, V.B. Ozdol, P.A. van Aken, *Appl. Phys. Lett.* **96**, 9 (2010).
47. E.P. Butler, *Rep. Prog. Phys.* **42**, 833 (1979).
48. H.G.F. Wilsdorf, *Rev. Sci. Instrum.* **29**, 323 (1958).
49. I. Robertson, P. Ferreira, G. Dehm, R. Hull, E.A. Stach, *MRS Bull.* **33**, 122 (2008).
50. A.M. Minor, E.A. Stach, J.W. Morris Jr., *Appl. Phys. Lett.* **79**, 1625 (2001).
51. A.M. Minor, S.A. Syed Asif, Z.W. Shan, E.A. Stach, E. Cyranowski, T.J. Wyrobek, O.L. Warren, *Nat. Mater.* **5**, 697 (2006).
52. Z.W. Shan, R.K. Mishra, S.A. Syed Asif, O.L. Warren, A.M. Minor, *Nat. Mater.* **7**, 115 (2008).
53. M. Legros, D.S. Gianola, C. Motz, *MRS Bull.* **35**, 354 (2010).
54. M.A. Haque, M.T.A. Saif, *Proc. Natl. Acad. Sci. U.S.A.* **101**, 6335 (2004).
55. D. Kiener, A.M. Minor, *Nano Lett.* **11**, 3816 (2011).
56. H. Guo, K. Chen, Y. Oh, K. Wang, C. Dejoie, S.A. Syed Asif, O.L. Warren, Z.W. Shan, J. Wu, A.M. Minor, *Nano Lett.* **11**, 3207 (2011).
57. L. Tian, Y.Q. Cheng, Z.W. Shan, J. Li, C.C. Wang, X.D. Han, J. Sun, E. Ma, *Nat. Commun.* **3**, 609 (2012).
58. C. Chisholm, H. Bei, M. Lowry, J. Oh, S.A. Syed Asif, O.L. Warren, Z.W. Shan, E.P. George, A.M. Minor, *Acta Mater.* **60**, 2258 (2012). □

PROPOSE A REVIEW ARTICLE TODAY!

www.mrs.org/energy-sustainability-journal

EDITORS-IN-CHIEF

David S. Ginley, National Renewable Energy Laboratory

David Cahen, Weizmann Institute of Science

Sally M. Benson, Stanford University




MRS ENERGY & SUSTAINABILITY
A Review Journal

Coming Soon


MRS Energy & Sustainability—A Review Journal will publish reviews on key topics in materials research and development as they relate to energy and sustainability. Topics to be reviewed include new R&D of both established and new areas; interdisciplinary systems integration; and objective application of economic, sociological, and governmental models, enabling research and technological developments. The reviews will be set in an integrated context of scientific, technological and sociological complexities relating to environment and sustainability.

The intended readership is a broad spectrum of scientists, academics, policy makers and industry professionals, all interested in the interdisciplinary nature of the science, technology and policy aspects of energy and sustainability.

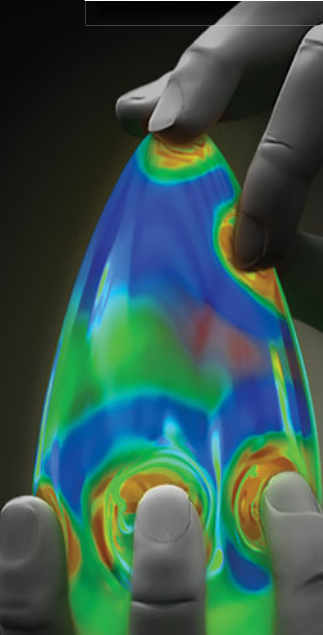
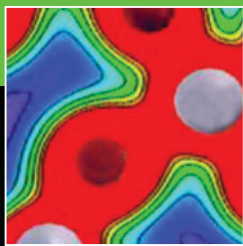
For more information, including author benefits, open access options, indexing and proposal form, visit www.mrs.org/energy-sustainability-journal.



MATERIALS RESEARCH SOCIETY®
Advancing materials. Improving the quality of life.



CAMBRIDGE
UNIVERSITY PRESS



“Stretching” the energy landscape of oxides—Effects on electrocatalysis and diffusion

Bilge Yildiz

Elastic strain engineering offers a new route to enable high-performance catalysts, electrochemical energy conversion devices, separation membranes and memristors. By applying mechanical stress, the inherent energy landscape of reactions involved in the material can be altered. This is the so-called mechano-chemical coupling. Here we discuss how elastic strain activates reactions on metals and oxides. We also present analogies to strained polymer reactions. A rich set of investigations have been performed on strained metal surfaces over the last 15 years, and the mechanistic reasons behind strain-induced reactivity are explained by an electronic structure model. On the other hand, the potential of strain engineering of oxides for catalytic and energy applications has been largely underexplored. In oxides, mechanical stress couples to reaction and diffusion kinetics by altering the oxygen defect formation enthalpy, migration energy barrier, adsorption energy, dissociation barrier, and charge transfer barrier. A generalization of the principles for stress activated reactions from polymers to metals to oxides is offered, and the prospect of using elastic strain to tune reaction and diffusion kinetics in functional oxides is discussed.

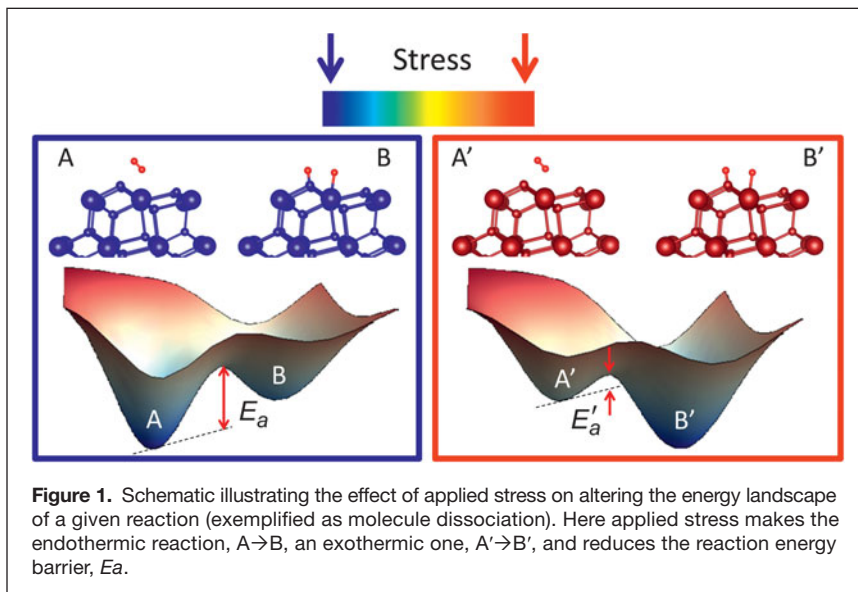
Introduction

The development of (electro)catalytic materials has traditionally relied on the design of new compositions and structures. In principle, previously unseen and desirable properties can be obtained by perturbing the structure of existing materials with elastic strain. Uncovering the fundamental mechanisms by which elastic strain alters the kinetics of (electro-)catalytic reactions can enable a new route to design highly efficient catalysts¹ and high-performance electrodes for clean energy conversion and storage devices, including fuel cells,^{2–5} electrolyzers,^{6,7} photocatalysts,⁸ and batteries.^{9,10}

Elastic strain can be induced by lattice mismatch at the interface in a thin-film composite, by local applied stress, or by chemical expansion in ionic systems. The resulting stresses can direct new chemical reactions or induce unusual stress responses in materials. An influential application of elastic strain has been the activation of chemical reactions in polymers by mechanical stress at the single molecule or single bond level.^{11–14} Despite the smaller elasticity of metals and oxides compared to polymers, recent work suggests that lattice strain can activate surface reactions also on metal and oxide catalysts, and anion transport in oxide membranes. In this review, we mainly discuss the fundamental effects of stress to accelerate reaction and transport kinetics in oxides, and

the potential of elastic strain engineering as a new route to improve the performance of oxide catalysts and electrocatalysts. The motivation of the work on strained oxides arises in part from the earlier seminal works on strained metal catalysts that are also reviewed here.

Lattice strain can affect chemical reactions in any material in the absence of structural transformations. A critical attribute is the stresses held in the bonds of an elastically strained material.^{12,14,15} Applying internal or external stresses alters the inherent energy landscape of the system. In theory, one can turn an endothermic reaction into an exothermic one and reduce the energy barriers (**Figure 1**). This is the so-called mechano-chemical coupling, and when applied to electrochemical systems, we can introduce the term mechano-electro-chemistry. As a motivating example of this coupling, we point to a recent elegant study in polymer chemistry, relating the stress response at the molecular level to chemical reactivity. Akbulatov et al.^{16,17} were able to apply forces at the spatial precision of links (bonds) between single molecules in a chain of polymeric molecules using an atomic force microscope (AFM) tip. An exponential dependence of reaction rates of cyclopropanes on the local forces were found in micrometer-long polymers and in macro-cycles. This exponential dependence demonstrates that indeed the reaction energy barriers are altered (reduced in this case) with local stresses.



For processes that involve the incorporation or migration of atoms, the available space in a strained lattice also contributes to changing the energy barriers, in addition to the effect of stress.

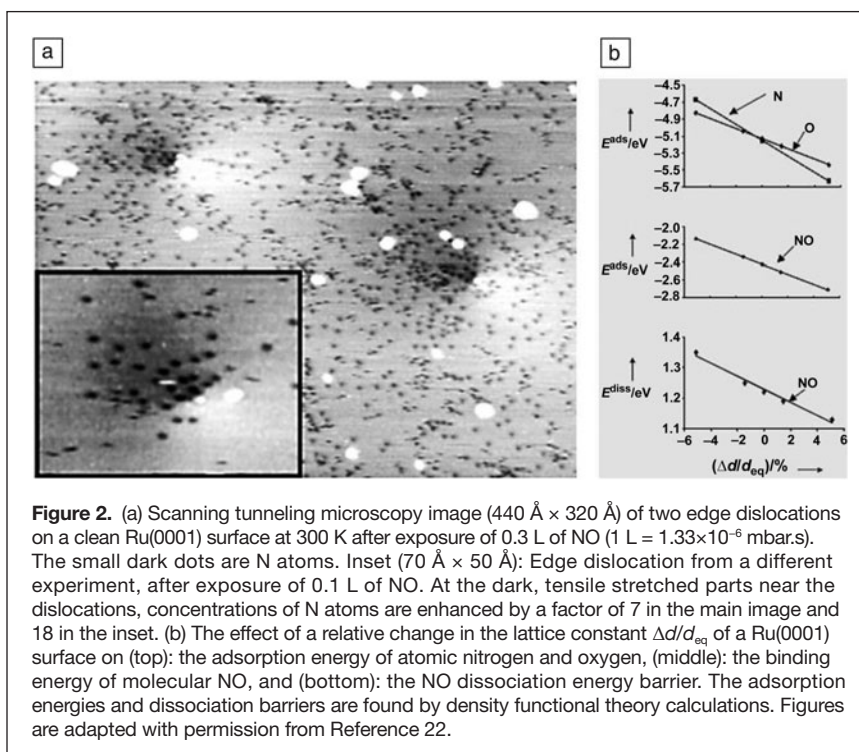
In the following, we review and discuss the effects of elastic strain on the reactivity of metal surfaces, and on the reaction and diffusion kinetics at the surface and in the bulk of ionic solids. The former is, in part, a motivator to strained oxide electrocatalysts in the latter.

Effect of strain on reactivity of metal surfaces

The body of literature in this field originates from the foundational works of Mavrikakis, Hammer, and Norskov¹⁸ and of Gsell, Jakob, and Menzel.¹⁹ Gsell and co-workers showed experimentally that lattice strain modified the chemisorption properties of the Ru(0001) metal surface considerably. Oxygen adsorption was found preferentially on the tensile strained zones upon local mechanical deformation of the surface by sub-surface Argon bubbles.¹⁹ Based on this observation, Mavrikakis and co-workers used density functional theory (DFT) to assess how elastic strain changes the ability of a surface to form bonds to adsorbed atoms or molecules by altering the reaction energies and electronic structure.¹⁸ The molecular (CO) and atomic (O) chemisorption energies as well as barriers for surface reactions (CO dissociation) were found to vary substantially on these strained lattices.¹⁸ In both cases, the chemisorption bond was found to get stronger and the dissociation barrier to decrease as the lattice constant increased. The origin of this effect was shown to arise from the shifts in the metal d bands induced by the stress.^{18,20} The

interaction between the adsorbate states and the metal d states is an important part of the reaction energy. Small changes in the environment can give rise to significant changes in the hybridization of the d states with adsorbate states.²¹ When the Ru(0001) surface was expanded in a planar way parallel to the surface, d band states moved up in energy, thereby strengthening the interaction with the adsorbates in all cases. These findings led to the generalization of this effect to several catalytically important systems. This revelation had far-reaching importance for heterogeneous catalysis, because almost all catalytic reactions are preceded by bond-activated dissociation steps that are often rate limiting, and lattice strain is present in most applications involving supported catalysts due to lattice defects or by interactions with the support material.

Wintterlin et al.²² provided the first experimental demonstration of the effect of strain field around an edge dislocation intersecting the metal surface on the local reactivity. Real catalysts are expected to have extended defects such as dislocations associated with elastic strain fields. The researchers performed scanning tunneling microscopy (STM) on Ru(0001) surfaces intersected by edge dislocations and imaged the dissociation of NO molecules. The results showed up to 18 times more enhanced reactivity to NO dissociation on the tensile strain field around the dislocation compared to that on the compressive strain field (**Figure 2a**). The calculated N, O, NO adsorption energies and the NO dissociation



energy barrier were found to decrease with increasing tensile strain on Ru(0001) (Figure 2b), explaining the experimental observations by STM in the same work.

Numerous works inspired by these early results demonstrated and utilized the effect of lattice strain in other metal catalyst systems, including gold,^{20,23} platinum,¹⁵ copper,²⁴ nickel,²⁵ and dealloyed bimetallic nanoparticles.²⁶ By surface chemistry measurements and theoretical calculations, Strasser and co-workers provided a molecular level understanding of the unprecedented electrocatalytic activity for the electroreduction of oxygen on dealloyed fuel cell catalysts.²⁶ The lattice strain in the Pt shell on a Pt/Cu bimetallic core was found to be the controlling factor in the catalytic enhancement of dealloyed Pt nanoparticles. Their work experimentally demonstrated a continuous change in the oxygen *2p* and Pt *5d* antibonding state from above to below the Fermi level as additional compressive strain was applied, thereby weakening the adsorbate bond. This represented the first direct experimental confirmation of the computational prediction of band shifts of adsorbate-projected band structure with application of strain.

The effect of strain on metal surface reactivity is equally important for oxidation and corrosion of structural materials as it is for catalytic applications. By using a specialized scanning probe tip as an *in situ* indenter, coupled with structural and electronic characterization in the STM, Herbert et al. showed that dislocations induced by highly localized and well-defined mechanical deformation on Ni(100) exhibited enhanced reactivity toward oxidation.²⁷ The residual strain resulting from plastic deformation was found to locally accelerate chemical reactions of molecular oxygen. The results were also interpreted as an upshift of the *d* band electrons near the dislocations, measured directly by tunneling spectroscopy. The successful and widespread investigation of elastic strain on metal catalysts is owing to the presence of a well-accepted electronic structure model, namely the *d* band model,²¹ as a reactivity descriptor.

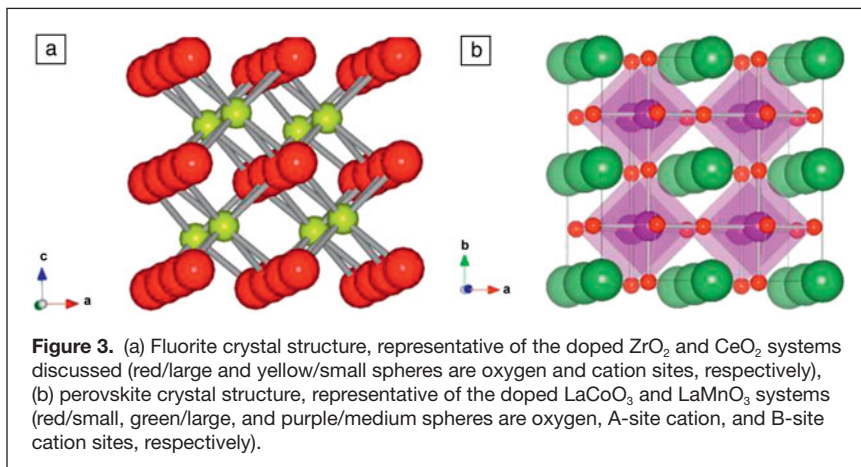
Effect of strain on ion transport and surface reactivity of oxide thin films

Discovering new oxide materials with high ionic and electronic conductivity and fast oxygen exchange kinetics on the surface is important for achieving optimal performance in a range of oxide-based electrochemical devices. To this end, an increasing number of studies have been utilizing nanoscale oxide thin films for systematic investigation of oxide interfacial properties^{28,29} and for making high-density devices for energy conversion and storage with micro solid oxide fuel cells,^{30,31} batteries,³² gas conversion/reformation catalysts,³³ sensors,³⁴ and for information storage and processing by redox-based resistive memories.^{35,36}

In nanoscale thin-film geometries, strains that originate from the lattice mismatch at interfaces can influence the properties of the material. While the coupling of strain to magnetism in multiferroic oxide heterostructures has been widely investigated (see the article by Schlom et al. in this

issue),^{37–40} the coupling of lattice strain to ion conduction and surface reaction kinetics on oxide nanostructures has not been extensively explored. This topic has attracted interest rather recently in the context of oxygen transport and electrode reactions in solid oxide fuel and electrolysis cells (SOFC, SOEC).^{2,54,55} Despite the small elastic strains, the stresses that can be maintained in lateral thin oxide films or vertical heterostructures are large, on the order of several GPa.⁴¹ This suggests the presence of a noticeable mechano-chemical coupling in strained oxides for impacting the reaction and transport energy barriers and the charge-carrier density and mobility.

The surface reactivity on strained metals that we reviewed previously was broadly investigated by measuring or modeling the impact of lattice strain on the electronic structure characterized with a simple but well-established reactivity descriptor, namely the *d* band energy center.²¹ The picture for oxide catalysts and membranes is, however, more complex. This is primarily because the metal oxides that are used are themselves chemically more complex. For example, perovskite structured compounds such as $\text{La}_{1-x}\text{Sr}_x\text{MnO}_3$ (LSM) and $\text{La}_{1-x}\text{Sr}_x\text{CoO}_3$ (LSC) serve as SOFC cathodes and separation membranes. External electromagnetic fields or mechanical strains were shown to give rise to unusual electronic and magnetic state transitions in these and other *3d* transition metal oxides.^{42,43} But the strain response of the oxygen non-stoichiometry, surface chemistry, and reactivity of these materials was not explored until recently. Perovskite oxides have two cation sublattices, dopants on each cation sublattice, and one anion sublattice, each of which can react to elastic strain. Some perovskite oxides have spin-state transitions taking place at elevated temperatures.⁴⁴ The spin state that alters internal bonding⁴⁵ is also responsive to strain via magneto-elastic coupling.⁴⁶ Furthermore, surface chemistry is not static. The composition, non-stoichiometry and structure at the surface respond to elevated temperatures by elemental segregation and phase separation,^{47,48} and to oxygen chemical potential gradients and electrochemical potentials.⁴⁹ This dynamic and not well-understood behavior on perovskite oxide surfaces has made it difficult to establish universal correlation of the electronic structure to reaction kinetics, despite various attempts.^{50–53} The complexity of the problem may look daunting, but recent findings on the possibility of tuning the reactivity and ion transport properties of complex oxides by "stretching" them (i.e., by elastic strain) are quite promising and worth investigating further. We first discuss the effects of strain on the ion conduction in fluorite oxides (Figure 3a) that serve as ion transport membranes (electrolyte) in SOFCs, SOECs, and oxygen sensors. We then extend the discussion to the effects of strain on the surface chemistry and electrocatalytic activity on more complex oxides, specifically the perovskite type oxides (Figure 3b) that serve as oxygen reduction electrocatalysts (cathode) in SOFCs,⁵⁴ oxygen evolution electrocatalysts for water splitting by electrolysis,⁵³ oxygen separation membranes in reactors for oxy-combustion,⁵⁵ and redox-based resistive memories.^{35,36}



Oxide ion conduction under lattice strain

The energy barrier for oxygen diffusion is the critical descriptor for how low a temperature the oxide electrolyte can effectively function. The most important point for us here is the potential of the lattice strain to reduce the oxygen migration energy barriers. We consider the two most widely investigated electrolyte systems for SOFCs: yttria-stabilized zirconia (YSZ) and gadolinium- or samarium-doped ceria (CGO, CSO).⁵⁴ These materials have fluorite crystal structures. They also function as oxygen sensors⁵⁶ and catalyst supports.^{57–59}

Despite these being rather widely studied “old” electrolyte materials, new possibilities to identify mechano-chemically coupled ways to accelerate oxygen diffusion in them has attracted significant interest recently. The oxygen transport in these solids takes place by thermally activated migration (or hopping) of an anion from one lattice site to the nearest anion vacancy site. The energy barriers for this mechanism (1.0–1.2 eV in YSZ, 0.9–1.16 eV in CGO)⁶⁰ are too high to enable fast diffusion at intermediate temperatures (400–600°C), where the next-generation SOFCs are envisioned in contrast to the current operating temperatures of 800°C or higher. A change in the migration barrier affects the self-diffusion coefficient exponentially via the Arrhenius relation. The migration barrier depends on the separation distance and available space between the hopping sites, and the bond strength between the oxygen and the neighboring cations. The latter is affected by the local defect interactions in the context of defect association.

The search for the “fastest strain” (the strain for which conductance is

highest) in ion-conducting oxides was sparked by the report in 2008 by Garcia-Barriocanal⁶¹ of an eight orders of magnitude increase in conductance of 1–30-nm-thick YSZ layers sandwiched between SrTiO₃ (STO) layers. The lattice mismatch at the interface of YSZ and STO is 7%, which is difficult to accommodate by elastic strain. To date, the exact nature of the conductance (ionic versus electronic) induced in the vicinity of the YSZ/STO interface remains debatable.^{62–65} However, the community responded to this result with great curiosity over the effect of lattice strain on ion conduction.^{62,66} Select works from literature in this area are summarized in **Table I**.

As can be seen in Table I, a large quantitative scatter exists in the relative improvement in ionic conductivities measured in experiments, ranging from none to 10⁸ times increase. Such large scatter in experimental results has been puzzling, and may arise because of elastic stress relaxation and the presence of dislocations. Many of the experimental studies only stated the theoretical lattice mismatch between the film and the substrate or the neighboring layers, without quantifying the exact strain state in the films. It is reasonable to expect that the inconsistencies in the experimental results arise from difficulties in controlling elastic lattice

Table I. Summary of selected works from literature on the relative increase in conductivity reported for strained thin films and multilayers. The entries in the last three rows are from computational studies, and all others are experimental.

Material	Geometry	T(K)	Relative Increase in Conductivity	Ref.
YSZ/STO	Multilayer	357–531	× 10 ⁸	61
YSZ/Y ₂ O ₃	Multilayer	623–973	× 10	67
YSZ/STO	Multilayer	357–531	None	64
YSZ on MgO	Thin film	423–773	× 10 ³	68
YSZ/STO	Multilayer	373–773	× 10 ⁵ compared to YSZ/Al ₂ O ₃ *Electronic conduction	63
Ce _{0.8} Sm _{0.2} O _{2-δ} (SDC)/YSZ	Multilayer	673–1073	× 10 compared to SDC × 10 compared to YSZ	69
Ce _{0.9} Gd _{0.1} O _{2-δ}	Thin Film	723–1123	× 10–10 ²	70
YSZ/CeO ₂	Multilayer	673–973	None	71
YSZ/Gd ₂ Zr ₂ O ₇	Multilayer	550–750	× 10 ²	72
YSZ/Y ₂ O ₃	Multilayer	793	× 2	73
Ce _{0.9} Gd _{0.1} O _{2-δ}	Thin Film	673–873	× 10–0	74
YSZ on MgO	Thin Film	673–1073	× 10 ²⁵	75
YSZ on Al ₂ O ₃	Thin Film	673–923	× 10 ^{0.5} @ 923 K × 10 ^{3.5} @ 400 K	76
YSZ	Strained bulk	400–1000	× 10 ^{1.5} @ 1000 K, ε = 0.04 × 10 ^{3.5} @ 400 K, ε = 0.04	77
CeO ₂	Strained bulk	500	× 10 ⁴ , ε = 0.04	78
ZrO ₂ /STO	Layered structure	0	Fluorite not stable for ε > 0.05	79

strain uniformly in the thin oxide films. Local relaxation of stress is expected to decrease or clear the effects of elastic strain on the energy landscape of the system. High-resolution strain mapping, achievable by advances in microscopy^{80,81} (also see the Hÿtch and Minor article in this issue) and computation,⁸² can provide one way to resolve this issue.

The results can be further complicated by the formation of dislocations upon stress relaxation, and it is also not yet clear how the dislocations alter the stability and mobility of ionic and electronic defects in their vicinity in a range of different oxides. This point is exemplified by comparing the work of Sillassen et al.⁶⁸ with that of Li et al.⁷² on YSZ. Sillassen et al. claimed that the dislocations at the YSZ/MgO interface contribute to accelerating oxide ion diffusion, in addition to the impact of elastic strain. On the other hand, Li et al. claimed that dislocation-free YSZ films interfacing with Gd₂Zr₂O₇ layers have higher ion conductivity compared to thin YSZ films on CeO₂, which introduces misfit dislocations. More work is needed to uncover the quantitative impact of dislocations in ion conduction kinetics in oxides.

Several theoretical and computational reports dug deeper into the mechanisms by which elastic strain alone can alter the oxygen migration kinetics. These works eliminate the influence of space-charge effects, misfit dislocations, or structural changes that could be present at the interfaces of YSZ with other materials in experiments. In assessing the role of elastic strain with atomistic detail, Kushima and Yildiz combined DFT calculations of migration paths and barriers with kinetic Monte Carlo calculations of oxygen diffusivity in 9% Y₂O₃ doped YSZ.⁷⁷ They identified two competing processes that act in parallel to alter the migration barrier for oxygen. First, at low strain states, the migration barrier reduces because of the increasing migration space and the weakening of the local oxygen–cation bonds via elastic stretching. With a decrease in the migration barrier, oxygen diffusivity exhibits an exponential increase up to a critical value of tensile strain, which Kushima and Yildiz called the fastest strain.⁷⁷ This increase is more significant at lower temperatures because of the exponential effect of the migration barrier with temperature on the diffusion coefficient. The fastest strain could be viewed as the optimal elastic strain state to attain the maximum acceleration of oxygen migration kinetics. Second, at strain states higher than the fastest strain, the migration energy barrier increases and diffusivity decreases. This is because the local relaxations at large strains trap the oxygen by strengthening the local oxygen–cation bonds—the stronger the binding of oxygen, the higher the migration barrier.⁸³ This indicated the transition from elastic stretching

to local plastic relaxations, or may be reminiscent of structure instability at high strains.⁷⁹ The electronic charge density distribution on the cation–oxygen (C–O) bonding plane along one representative migration path in YSZ is shown in **Figure 4a** as a function of strain. For this path, elastic stretching up to 6% strain weakens the C–O bond and reduces the migration barrier of oxygen. From 6% to 8%, the breaking of a neighboring cation–oxygen re-strengthens the C–O bond and increases the migration barrier. In 9%-YSZ, the highest effective enhancement of diffusivity was predicted to occur at 4% as the fastest strain, by 3×10^1 times at 1000 K and by 7×10^3 times at 400 K (Figure 4b). The effective migration barrier is reduced by 0.4 eV.

Using a model that takes into account the isotropic pressure induced by elastic strain in YSZ, Schichtel et al.⁸⁴ estimated a 2.5 orders of magnitude increase in the ionic conductivity of YSZ at 7% strain at 573 K. Schichtel et al.’s model, however, does not take into account the relaxations of elastic strain at these large tensile strain states. Therefore, it cannot capture the plastic or structural relaxations, which may actually mitigate the diffusivity at large strains beyond elastic stretching.

De Souza and co-workers assessed the effect of strain on oxygen-vacancy migration in CeO₂ by static lattice simulations.⁷⁸ With both isotropic and biaxial strain, significant modification of the energy barriers for oxygen-vacancy migration was found. Their results also suggest that a biaxial tensile strain

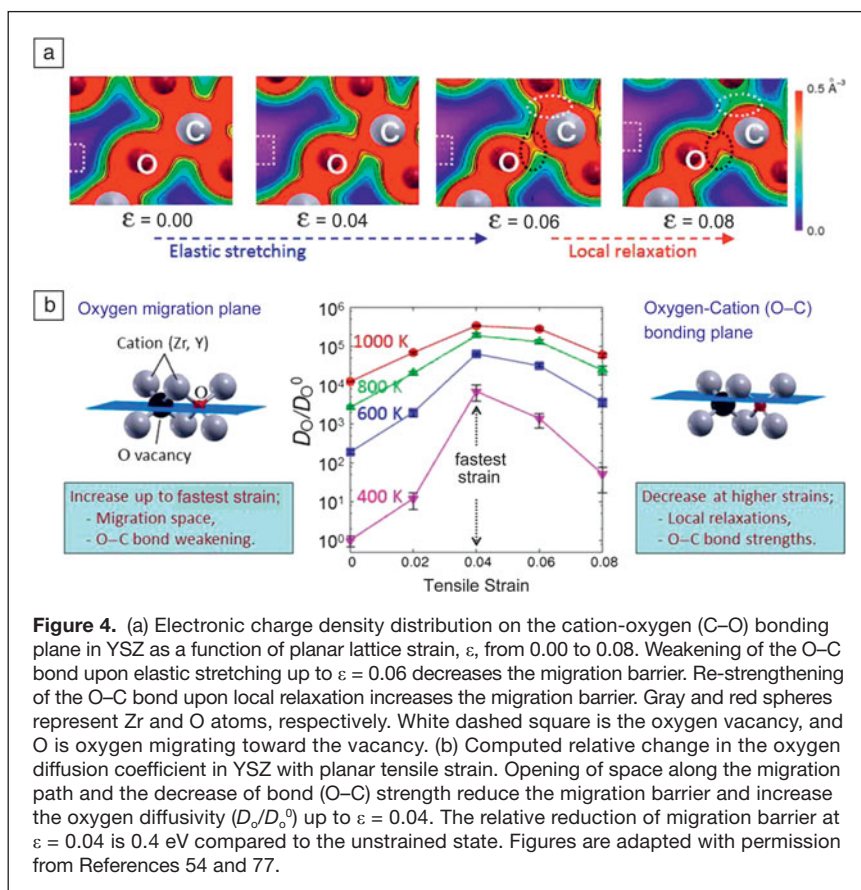


Figure 4. (a) Electronic charge density distribution on the cation–oxygen (C–O) bonding plane in YSZ as a function of planar lattice strain, ϵ , from 0.00 to 0.08. Weakening of the O–C bond upon elastic stretching up to $\epsilon = 0.06$ decreases the migration barrier. Re-strengthening of the O–C bond upon local relaxation increases the migration barrier. Gray and red spheres represent Zr and O atoms, respectively. White dashed square is the oxygen vacancy, and O is oxygen migrating toward the vacancy. (b) Computed relative change in the oxygen diffusion coefficient in YSZ with planar tensile strain. Opening of space along the migration path and the decrease of bond (O–C) strength reduce the migration barrier and increase the oxygen diffusivity (D_0/D_0^0) up to $\epsilon = 0.04$. The relative reduction of migration barrier at $\epsilon = 0.04$ is 0.4 eV compared to the unstrained state. Figures are adapted with permission from References 54 and 77.

of 4% increases the in-plane conductivity at $T = 500$ K by close to four orders of magnitude. The predicted effect of strain on oxygen conductivity is very close to that found by Kushima and Yildiz for YSZ, suggesting that the energy landscape in these fluorite oxides, in theory, responds to strain in a similar way.

It is also interesting to note that the computational predictions of the effect of strain on ion conduction in YSZ and ceria CeO_2 are quite close to the maximum of the relative improvement in conductivity found in experiments⁶⁸ on the order of 10^3 – 10^4 , except from the unprecedented results of Reference 61. Furthermore, the reduction in the effective activation energy for diffusion in YSZ was quantified experimentally only in two of the reported studies. Jiang et al.’s results indicated about a 0.2 eV reduction of the activation energy and Sillassen et al.’s experiments about 0.35 eV.⁶⁸ These are close to the reduction of effective migration barrier predicted⁷⁷ within the experimented strain ranges. Last, it is notable that none of the experimental and computational works on the effects of strain in YSZ or ceria thin films have been able to explain or replicate the conductivity values shown for the STO/YSZ/STO layered system.⁶¹ This discrepancy suggests that strain alone cannot be responsible for the magnitude of ion conduction claimed for that particular system. Nonetheless, increases in oxide ion conductivity proposed by theory and some experiments for strained YSZ films are remarkable and are of great fundamental and practical importance. The results exemplify how local weakening of bonds in the form of elastic stretching can enable more facile oxygen migration, and thus, fast diffusion kinetics in functional oxides.

Surface chemistry and electrocatalytic activity under lattice strain

The energy landscape of surface reactions can also be altered by elastic strain, as already demonstrated on metals previously. We investigated this effect on oxides as a means to enhance their reactivity to oxygen electrocatalysis. As model electrocatalyst systems, we took the perovskite family of oxides, specifically $\text{La}_{1-x}\text{Sr}_x\text{MnO}_3$ (LSM) and $\text{La}_{1-x}\text{Sr}_x\text{CoO}_3$ (LSC), that have been the most widely studied SOFC cathode materials. These compounds also serve as ion transport membranes (ITM) in oxy-combustion⁵⁵ and have been studied widely for their magnetic properties.⁴⁶ To serve as a good cathode or ITM, they must exhibit fast oxygen reduction kinetics, or fast oxygen evolution kinetics for water splitting. While the oxygen molecule adsorption, dissociation, and charge transfer reactions are common to oxygen reduction on metals⁸⁵ and on oxides,⁸⁶ a key differentiating factor is the presence of oxygen vacancies on the latter. Both the concentration and mobility of oxygen vacancies on the surface affect oxygen reduction kinetics on oxides. The more

oxygen vacancies and the faster they move at the surface, the faster the oxygen reduction kinetics.⁸⁶ They also impact the surface electronic structure (charge transfer).⁸⁷

How elastic strain impacts the oxygen vacancy formation in the bulk and oxygen adsorption and vacancy formation at the surface of LaCoO_3 (LCO) was examined by DFT calculations.⁸⁸ The effects of biaxial strain on these elementary reactions were found to manifest through two competing mechanisms that alter the strength of Co–O bonds in LCO: (1) elastic stretching of Co–O bonds, which reduces the overlap of the Co d -band and O p -band in the lattice, and (2) stress relaxations due to breaking and reforming of the Co–O bonds and due to spin state transitions. Reaction energy calculations showed each that elastic stretching facilitates each of the studied elementary processes, as long as there is an increase in the tensile stress state (**Figure 5**). This is consistent with the effect of stress on the energy landscape, as illustrated in Figure 1. The formation energy of vacancies in the bulk and on the surface of LCO decreases with increasing elastic tensile strain. A consequence of this is an increase in the concentration of oxygen vacancies as reactive sites on the surface and as diffusion-mediators in the bulk. The trend reverses when there is a stress reduction because of a strain-driven spin state transition from low- to intermediate-spin or because of plastic relaxations. Elastic stretching weakens the lattice Co–O bonds, and stress reduction strengthens the Co–O bonds and traps the lattice oxygen. Weakening of the lattice Co–O bonds at the surface allows for stronger hybridization between the d -band states of the surface Co and the $2p$ states of the adsorbing O_2 , thereby increasing the adsorption energy of the O_2 molecule. A consequence of this is the increased coverage of adsorbed oxygen.

Reaction energies, electronic structure, spin state, and stress thresholds found in Kushima et al.’s work⁸⁸ suggested the possibility of tuning reactivity by strain in LaCoO_3 and related perovskite oxides. As a follow-up to this computational work, there have been three key experimental reports, one probing

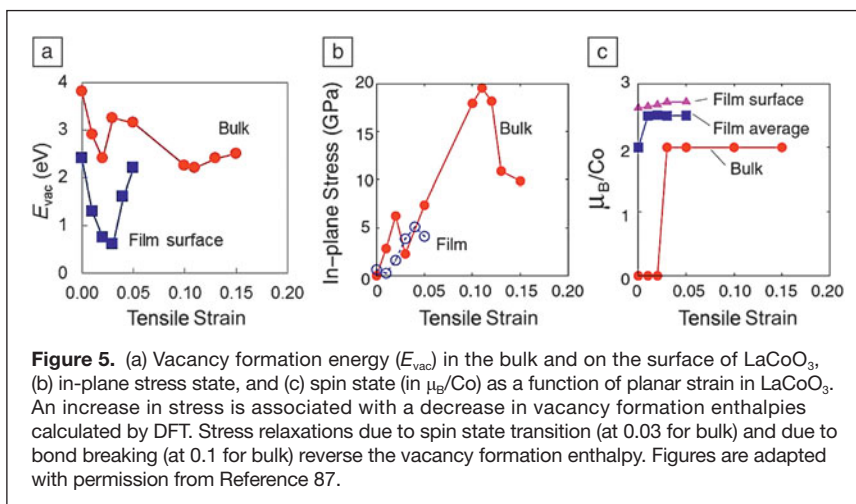


Figure 5. (a) Vacancy formation energy (E_{vac}) in the bulk and on the surface of LaCoO_3 , (b) in-plane stress state, and (c) spin state (in μ_B/Co) as a function of planar strain in LaCoO_3 . An increase in stress is associated with a decrease in vacancy formation enthalpies calculated by DFT. Stress relaxations due to spin state transition (at 0.03 for bulk) and due to bond breaking (at 0.1 for bulk) reverse the vacancy formation enthalpy. Figures are adapted with permission from Reference 87.

the ease of charge transfer and vacancy formation, and two quantifying the collective kinetics of oxygen exchange and diffusion as a function of strain. First, Cai et al.’s experiments⁸⁹ demonstrated that tensile strain induces a greater concentration of oxygen vacancies on $\text{La}_{0.8}\text{Sr}_{0.2}\text{CoO}_3$ (LSC) thin films (Figure 6c) at elevated temperatures (up to 450°C). Tensile and compressive strains were achieved by epitaxially depositing LSC thin films on single crystal SrTiO_3 (STO) and LaAlO_3 (LAO) substrates, respectively. The greater presence of oxygen vacancies on the tensile LSC film was deduced by the presence of reduced Co species in the Co 2*p* photoelectron spectra that was measured at elevated temperatures. This result is consistent with Kushima et al.’s predictions. Tensile strained LSC films (and also on LSM films in Reference 90) exhibited enhanced electron transfer on their surfaces at elevated temperatures above 300°C, as identified by *in situ* tunneling spectroscopy (Figure 6b). Enhancement in vacancy concentration and charge transfer on tensile strained LSC film surfaces can both accelerate oxygen reduction kinetics.

Kubicek et al. quantified the influence of lattice strain on the kinetics of oxygen exchange and diffusion on/across (100) epitaxial LSC thin films,⁹¹ the same films as reported by Cai et al.⁸⁹ The method was based on ¹⁸O isotope exchange and depth profiling with Time of Flight Secondary Ion Mass Spectroscopy (ToF-SIMS). Much faster surface exchange (~4 times) and diffusion (~10 times) were observed for the tensile strained films compared to the compressively strained films in the temperature range of 280 to 475°C (Figure 6d–e). The same outcome was found for different LSC compositions

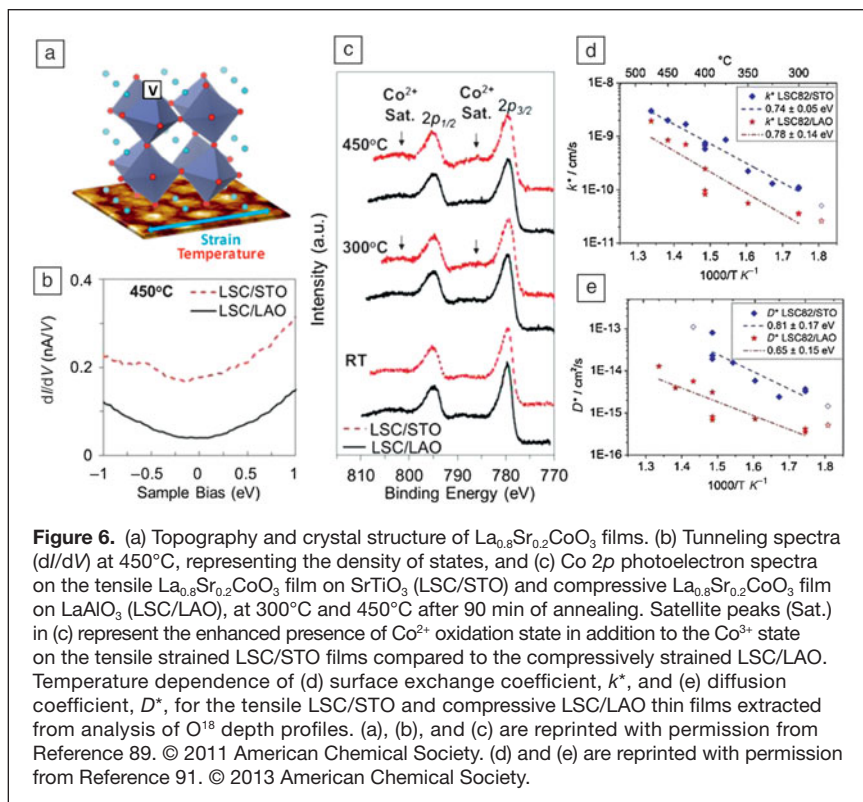
($x = 0.2$ and $x = 0.4$) and for surface-etched films. It is not possible to deduce whether the enhancement arises from a reduction in the formation enthalpy of oxygen vacancies or an increase in the vacancy mobility or a better electron transfer activity. It is likely that all of these factors are in place.

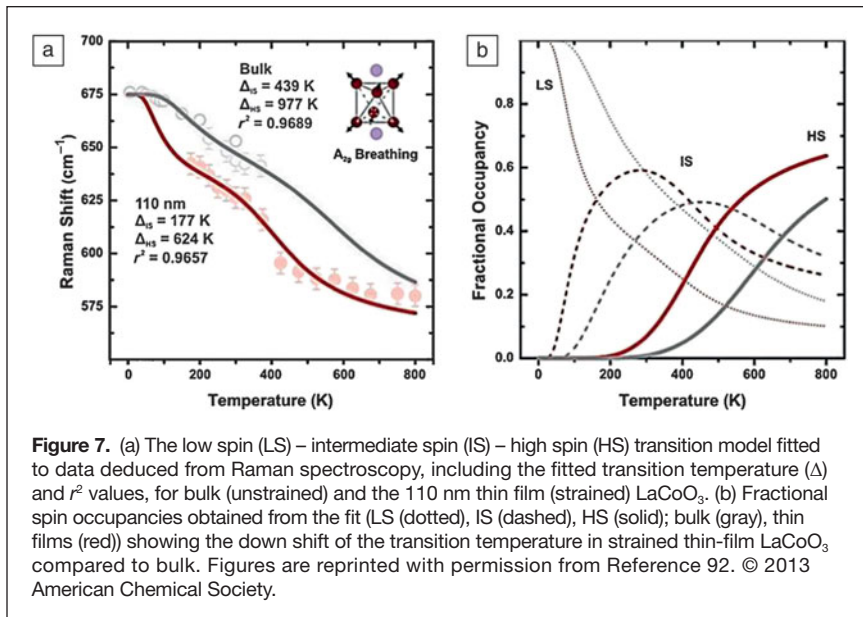
Hong et al.’s work aimed to tune the catalytic activity through strain-induced changes in the Co spin state in LaCoO_3 thin films.⁹² They probed the Co–O bond strength by Raman spectroscopy at different temperatures to determine the relative spin occupancies of LaCoO_3 . Strain in the LCO films reduced the spin transition temperature (Figure 7) and promoted the occupation of higher spin states. The spin moment increase was accompanied by the weakening of Co–O bonds. The decrease in Co–O bond strength, as suggested by Kushima et al.⁸⁸ and by Pavone et al.,⁹³ resulted in marked enhancements, up to two orders of magnitude, in the oxygen surface exchange kinetics detected by electrochemical impedance spectroscopy.

Generalization of stress effects on reactivity

Findings from theoretical and experimental efforts as discussed here point toward the promise of tuning oxygen surface exchange and diffusion kinetics by means of lattice strain in existing ionic and electronic conducting oxides as well as metals for catalysis and energy conversion applications. The fundamental mechanism of elastic strain driven reactions and transport is the impact of stress on the energy landscape of the system, and this is broadly valid among various classes of materials, including polymers, metals, and ceramics.¹² Figure 8 illustrates the general trend, schematically, for several reactions and materials reviewed in this article. One can see that the more tensile the strain (within the elastic limit), the lower the vacancy formation enthalpy, vacancy migration barrier, adsorption energy (negative), and molecule dissociation energy barrier. All of this can be explained based on the weakening of the interatomic bonds in the tensile strained lattice. The concept is similar to doping materials to stress and expand the lattice, which results in lower atomic migration energy barriers.^{74,94}

The trends shown in Figure 8 typically accelerate the surface reactions and bulk diffusion of oxygen at tensile strains. While this trend favors the device performance in fuel cells, electrolyzers, ion transport membranes, and even in memristors, the same effects can become detrimental in corrosion where the reactions and diffusion should be slow. For example, the predicted faster oxygen diffusion in tensile strained zirconia films implies accelerated oxidation kinetics through the passive film on zirconium alloys⁹⁵ and also faster corrosion kinetics at crack tips with tensile strain.⁹⁶





To extend to a few more examples, we consider ceria, a technologically important catalyst, catalyst support, and ion transport membrane material. Sayle et al.’s atomistic calculations showed that the chemical reactivity of ceria nanorods to oxidize CO to CO_2 (by extracting oxygen from the surface) increased with applied tension and reduced when compressed.⁹⁷ This is still another demonstration of strain-tunable reactivity on an oxide. The same work discussed the implications and relevance of the strain-driven reactivity to a variety of important processes and applications, including TiO_2 nanoparticles for photocatalysis, mesoporous ZnS for semiconductor band-gap engineering, MgO for catalysis, and Li-MnO₂ lithiation-induced strain for energy storage. In another interesting and recent example, Cha et al. showed experimentally that the presence of dislocations considerably enhances the photocatalytic activity of rutile TiO_2 nanostructures.⁹⁸ The underlying reason was demonstrated to be the modification of the band-gap by the elastic strain field of dislocations.

Furthermore, the fundamental mechanism here is so basic and deep that it can be generalized even to defect reactions in the bulk of a material. An extension of this understanding is to metal plasticity, which is governed by the behavior of dislocations and their interactions with point defects and defect clusters in the metal. For example, it is well known that the activation energies for the nucleation and migration (flow) of dislocations in metals depend on applied stress.^{99–101} At very high strain rates, the strain localization increases the stress and decreases the energy barriers of dislocation-defect interactions.¹⁰² These are important to account for in predicting the strength of metals over a wide range of applied strain rates and temperatures.

Conclusions and outlook

The title of this article implies that we can “stretch,” that is, elastically strain functional oxides to enhance their surface

reactivity and oxygen transport properties for electrochemical energy conversion applications. This theme was largely motivated by the outstanding effects of elastic strain demonstrated for reaction kinetics on metal surfaces and in polymers, as reviewed at the beginning of this article. The effect of stress on the energy landscape of the system is the key factor that couples to thermal activation and helps drive the reaction kinetics. On metals, effects of elastic strain in markedly enhancing surface reactivity are reflected as changes of the *d*-band electron energies. The strain-induced shifts of the *d*-band electron energy affect the strength of adsorption on a metal surface and the dissociation energy barriers.

For oxides, the situation is more intricate because of the chemical, electronic, and structural complexity. Despite the compounded nature of the problem, recent experimental results are encouraging, regardless of the quantitative variation among them. Based on theoretical predictions, the impact of elastic strain on reactivity and transport properties of oxides takes place via a coupling of mechanics to the energetics of elementary reactions. Specifically, oxygen defect formation enthalpy, oxygen migration energy barrier, adsorption energy, dissociation barrier, and charge transfer barrier are all altered by elastic strain. Typically, tensile strain was found to accelerate oxygen diffusion and oxygen surface exchange kinetics. The common key in different classes of materials is the stress (force) and the weakening of the interatomic bonds, which helps to activate the reactions. The reasons behind the quantitative variation among experimental results are thus far more difficult to resolve. Stress relaxations through structural changes, dislocation formation, and spin-state transitions can all reverse the effects of elastic strain in the material.

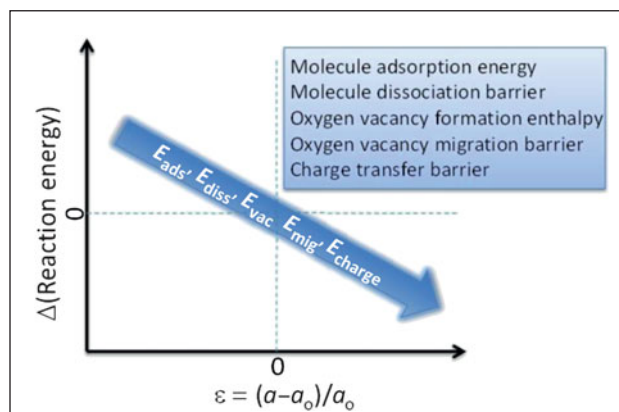


Figure 8. Schematic illustration for relative changes in reaction energies as a function of lattice strain, ϵ , in the elastic regime. The diagram qualitatively indicates the reduction of the molecule adsorption energies (E_{ads}), oxygen vacancy formation enthalpy (E_{vac}), molecule dissociation (E_{diss}), and atom migration (E_{mig}) energy barriers with increasing tensile strain.

One could broaden the implications of strain (stress) driven reactions from solid oxide fuel cells and electrolyzers to oxide-based photocatalysts, redox-based memristive switches, and oxidative corrosion, where the oxidation and reduction reactions at the surface/interface and diffusion of oxygen through an oxide phase determine the performance. Understanding how the oxygen defect chemistry is altered by strain can also help separate the indirect chemical effects of strain from its direct structural effects on the magnetic state transitions in magneto-elastic oxides.^{43,103}

In summary, it seems promising that the surface reactivity and oxygen diffusion kinetics can be tuned by means of elastic strain in existing ionic and mixed conducting oxides. New opportunities for better understanding and control of this effect in oxides have been emerging through the synthesis of nanoscale strained thin films, multilayers, and vertical heterostructures and through the first-principles-based computational predictions. Designing new methods to quantify bond strengths locally in the solid state may help significantly in these investigations. More systematic investigations to determine precisely how elastic strain and dislocations alter reactivity in different oxide crystal classes are needed, as has been the case for metals for many years. This field is fertile ground for exciting new discoveries to enable highly efficient energy conversion devices, novel catalyst systems, and high-density and fast memory devices.

Acknowledgments

B.Y. gratefully acknowledges support from the CAREER Award ("Stretching" Oxides to Low Temperature Transport and Reactivity) of the National Science Foundation, Division of Materials Research, Ceramics Program, Grant No.1055583, and the US Department of Energy - Basic Energy Sciences, Grant No. DE-SC0002633. B.Y. is also thankful to Manos Mavrikakis for his review and constructive comments on this article prior to publication. B.Y. thanks her students and post-docs, whose research results she synthesized into this article.

References

1. A.T. Bell, *Science* **299** (5613), 1688 (2003).
2. B.C.H. Steele, A. Heinzel, *Nature* **414** (6861), 345 (2001).
3. V.R. Stamenkovic, B. Fowler, B.S. Mun, G.F. Wang, P.N. Ross, C.A. Lucas, N.M. Markovic, *Science* **315** (5811), 493 (2007).
4. M.Z. Jacobson, W.G. Colella, D.M. Golden, *Science* **308** (5730), 1901 (2005).
5. J.L. Zhang, M.B. Vukmirovic, Y. Xu, M. Mavrikakis, R.R. Adzic, *Angew. Chem. Int. Ed. Engl.* **44** (14), 2132 (2005).
6. C. Costentin, S. Drouet, M. Robert, J.M. Saveant, *Science* **338** (6103), 90 (2012).
7. Y. Nakato, N. Takamori, H. Tsubomura, *Nature* **295** (5847), 312 (1982).
8. W.C. Chueh, C. Falter, M. Abbott, D. Scipio, P. Furler, S.M. Haile, A. Steinfield, *Science* **330** (6012), 1797 (2010).
9. J.M. Tarascon, M. Armand, *Nature* **414** (6861), 359 (2001).
10. B. Kang, G. Ceder, *Nature* **458** (7235), 190 (2009).
11. M.M. Caruso, D.A. Davis, Q. Shen, S.A. Odum, N.R. Sottos, S.R. White, J.S. Moore, *Chem. Rev.* **109** (11), 5755 (2009).
12. C.R. Hickenboth, J.S. Moore, S.R. White, N.R. Sottos, J. Baudry, S.R. Wilson, *Nature* **446** (7134), 423 (2007).
13. J. Liang, M. Fernandez, *ACS Nano* **3** (7), 1628 (2009).
14. D.A. Davis, A. Hamilton, J.L. Yang, L.D. Cremer, D. Van Gough, S.L. Potisek, M.T. Ong, P.V. Braun, T.J. Martinez, S.R. White, *Nature* **459** (7243), 68 (2009).
15. L. Grabow, Y. Xu, M. Mavrikakis, *Phys. Chem. Chem. Phys.* **8** (29), 3369 (2006).

16. S.L. Craig, *Nature* **487** (7406), 176 (2012).
17. S. Akbulatov, Y. Tian, R. Boulatov, *J. Am. Chem. Soc.* **134** (18), 7620 (2012).
18. M. Mavrikakis, B. Hammer, J.K. Nørskov, *Phys. Rev. Lett.* **81** (13), 2819 (1998).
19. M. Gsell, P. Jakob, D. Menzel, *Science* **280** (5364), 717 (1998).
20. M. Mavrikakis, P. Stoltze, J.K. Nørskov, *Catal. Lett.* **64** (2-4), 101 (2000).
21. B. Hammer, J.K. Nørskov, *Surf. Sci.* **343**, 211 (1995).
22. J. Wintterlin, T. Zambelli, J. Trost, J. Greeley, M. Mavrikakis, *Angew. Chem. Int. Ed. Engl.* **42** (25), 2850 (2003).
23. Y. Xu, M. Mavrikakis, *J. Phys. Chem. B* **107** (35), 9298 (2003).
24. Y. Xu, M. Mavrikakis, *Surf. Sci.* **494** (2), 131 (2001).
25. J. Greeley, W.R. Kregelberg, M. Mavrikakis, *Angew. Chem. Int. Ed. Engl.* **43** (33), 4296 (2004).
26. P. Strasser, S. Koh, T. Anniyev, J. Greeley, K. More, C.F. Yu, Z.C. Liu, S. Kaya, D. Nordlund, H. Ogasawara, *Nat. Chem.* **2** (6), 454 (2010).
27. F.W. Herbert, K.J. Van Vliet, B. Yildiz, *MRS Commun.* **2** (01), 23 (2011).
28. A. Ohmoto, H.Y. Hwang, *Nature* **427** (6973), 423 (2004).
29. N. Reyren, A.D. Caviglia, L.F. Kourkoutis, G. Hammerl, C. Richter, C.W. Schneider, T. Kopp, A.-S. Ruetschi, D. Jaccard, M. Gabay, D.A. Mueller, J.-M. Triscone, J. Mannhart, *Science* **317** (5842), 1196 (2007).
30. A. Evans, A. Bieberle-Hutter, J.L.M. Rupp, L.J. Gauckler, *J. Power Sources* **194** (1), 119 (2009).
31. R. Tolke, A. Bieberle-Hutter, A. Evans, J.L.M. Rupp, L.J. Gauckler, *J. Eur. Ceram. Soc.* **32** (12), 3229 (2012).
32. J. Suntivich, H.A. Gasteiger, N. Yabuuchi, H. Nakanishi, J.B. Goodenough, Y. Shao-Horn, *Nat. Chem.* **3** (8), 647 (2011).
33. S.B. Adler, J.A. Lane, B.C.H. Steele, *J. Electrochem. Soc.* **143**, 3554 (1996).
34. N. Barsan, D. Koziej, U. Weimar, *Sensor. Actuat. B-Chem.* **121** (1), 18 (2007).
35. R. Waser, M. Aono, *Nat. Mater.* **6** (11), 833 (2007).
36. R. Waser, R. Dittmann, G. Staikov, K. Szot, *Adv. Mater.* **21** (25-26), 2632 (2009).
37. J.X. Zhang, Q. He, M. Trassin, W. Luo, D. Yi, M.D. Rossell, P. Yu, L. You, C.H. Wang, C.Y. Kuo, *Phys. Rev. Lett.* **107** (14), 147602 (2011).
38. K.T. Ko, M.H. Jung, Q. He, J.H. Lee, C.S. Woo, K. Chu, J. Seidel, B.G. Jeon, Y.S. Oh, K.H. Kim et al., *Nat. Commun.* **2**, 567 (2011).
39. Q. He, Y.H. Chu, J.T. Heron, S.Y. Yang, W.I. Liang, C.Y. Kuo, H.J. Lin, P. Yu, C.W. Liang, R.J. Zeches et al., *Nat. Commun.* **2**, 225 (2011).
40. R. Ramesh, N.A. Spaldin, *Nat. Mater.* **6** (1), 21 (2007).
41. Y. Kuru, D. Marrocchelli, S.R. Bishop, D. Chen, B. Yildiz, H.L. Tuller, *J. Electrochem. Soc.* **159** (11), F799 (2012).
42. Y. Ding, D. Haskel, Y.C. Tseng, E. Kaneshita, M. van Veenendaal, J.F. Mitchell, S.V. Sinogeikin, V. Prakapenka, H.K. Mao, *Phys. Rev. Lett.* **102** (23), 237201 (2009).
43. A.D. Rata, A. Herklotz, K. Nenkov, L. Schultz, K. Dorr, *Phys. Rev. Lett.* **100** (7), 076401 (2008).
44. J.B. Goodenough, J.S. Zhou, *Chem. Mater.* **10** (10), 2980 (1998).
45. M. Haverkort, Z. Hu, J. Cezar, T. Burnus, H. Hartmann, M. Reuther, C. Zobel, T. Lorenz, A. Tanaka, N. Brookes, *Phys. Rev. Lett.* **97** (17), 247208 (2006).
46. D. Fuchs, E. Arac, C. Pinta, S. Schuppler, R. Schneider, H. v. Löhneysen, *Phys. Rev. B* **77** (1), 014434 (2008).
47. W. Lee, J.W. Han, Y. Chen, Z. Cai, B. Yildiz, *J. Am. Chem. Soc.* **135** (21), 7909 (2013).
48. M.L. Kubicek, T. Fromling, H. Hutter, J. Fleig, *J. Electrochem. Soc.* **158** (6), B727 (2011).
49. W.C. Chueh, S.M. Haile, *Annu. Rev. Chem. Biomol.* **3**, 313 (2012).
50. W. Jung, H.L. Tuller, *Adv. Energy Mater.* **1** (6), 1184 (2011).
51. N.A. Deskins, R. Rousseau, M. Dupuis, *J. Phys. Chem. C* **114**, 5891 (2010).
52. Y.-L. Lee, J. Kleis, J. Rossmeisl, Y. Shao-Horn, D. Morgan, *Energy Environ. Sci.* **4** (10), 3966 (2011).
53. J. Suntivich, K.J. May, H.A. Gasteiger, J.B. Goodenough, Y. Shao-Horn, *Science* **334** (6061), 1383 (2011).
54. A. Chronos, B. Yildiz, A. Tarancón, D. Parfitt, J.A. Kilner, *Energy Environ. Sci.* **4** (8), 2774 (2011).
55. M.A. Habib, M. Nemitallah, R. Ben-Mansour, *Energ. Fuel.* **27** (1), 2 (2013).
56. Y. Sugawara, K. Ogawa, H. Goto, S. Oikawa, K. Akaike, N. Komura, R. Eguchi, K. Kajii, S. Gohda, Y. Kubozono, *Sensor. Actuat. B-Chem.* **171**, 544 (2012).
57. R. Si, J. Raitano, N. Yi, L.H. Zhang, S.W. Chan, M. Flytzani-Stephanopoulos, *Catal. Today* **180** (1), 68 (2012).
58. Z. Zhou, S. Kooi, M. Flytzani-Stephanopoulos, H. Saltsburg, *Adv. Funct. Mater.* **18** (18), 2801 (2008).
59. N. Yi, R. Si, H. Saltsburg, M. Flytzani-Stephanopoulos, *Energy Environ. Sci.* **3** (6), 831 (2010).
60. V.V. Kharton, F.M.B. Marques, A. Atkinson, *Solid State Ionics* **174** (1-4), 135 (2004).
61. J. Garcia-Barriocanal, A. Rivera-Calzada, M. Varela, Z. Sefrioui, E. Iborra, C. Leon, S.J. Pennycook, J. Santamaria, *Science* **321** (5889), 676 (2008).
62. J.A. Kilner, *Nat. Mater.* **7** (11), 838 (2008).

63. A. Cavallaro, M. Burriel, J. Roqueta, A. Apostolidis, A. Bernardi, A. Tarancon, R. Srinivasan, S.N. Cook, H.L. Fraser, J.A. Kilner, *Solid State Ionics* **181** (13–14), 592 (2010).
64. X. Guo, *Science* **324** (5926), 465 (2009).
65. R.A. De Souza, A.H.H. Ramadan, *Phys. Chem. Chem. Phys.* **15** (13), 4505 (2013).
66. J.L.M. Rupp, *Solid State Ionics* **207**, 1 (2012).
67. C. Korte, A. Peters, J. Janek, D. Hesse, N. Zakharov, *Phys. Chem. Chem. Phys.* **10** (31), 4623 (2008).
68. M. Sillassen, P. Eklund, N. Pryds, E. Johnson, U. Helmersson, J. Bottiger, *Adv. Funct. Mater.* **20** (13), 2071 (2010).
69. S. Sanna, V. Esposito, A. Tebano, S. Licoccia, E. Traversa, G. Balestrino, *Small* **6** (17), 1863 (2010).
70. K.M. Kant, V. Esposito, N. Pryds, *Appl. Phys. Lett.* **100** (3), 033105 (2012).
71. D. Pergolesi, E. Fabbri, S.N. Cook, V. Roddatis, E. Traversa, J.A. Kilner, *ACS Nano* **6** (12), 10524 (2012).
72. B. Li, J.M. Zhang, T. Kaspar, V. Shutthanandan, R.C. Ewing, J. Lian, *Phys. Chem. Chem. Phys.* **15** (4), 1296 (2013).
73. H. Aydin, C. Korte, M. Rohne, J. Janek, *Phys. Chem. Chem. Phys.* **15** (6), 1944 (2013).
74. J. Rupp, E. Fabbri, D. Marrocchelli, J.-W. Han, D. Chen, E. Traversa, H.L. Tuller, B. Yildiz, *Adv. Funct. Mater.* (2013), doi: 10.1002/adfm.201302117.
75. I. Kosacki, C.M. Rouleau, P.F. Becher, J. Bentley, D.H. Lowndes, *Solid State Ionics* **176** (13–14), 1319 (2005).
76. J. Jiang, X. Hu, W. Shen, C. Ni, J.L. Hertz, *Appl. Phys. Lett.* **102** (14), 143901 (2013).
77. A. Kushima, B. Yildiz, *J. Mater. Chem.* **20** (23), 4809 (2010).
78. R.A. De Souza, A. Ramadan, S. Horner, *Energy Environ. Sci.* **5** (1), 5445 (2012).
79. W.L. Cheah, M.W. Finnis, *J. Mater. Sci.* **47** (4), 1631 (2012).
80. C.L. Johnson, E. Snoeck, M. Ezcurdia, B. Rodríguez-González, I. Pastoriza-Santos, L.M. Liz-Marzán, M.J. Hÿtch, *Nat. Mater.* **7** (2), 120 (2007).
81. A. Béch e, J.L. Rouvi ere, J.P. Barnes, D. Cooper, *Ultramicroscopy* **131**, 10 (2013).
82. A. Smolyanitsky, V.K. Tewary, *Nanotechnology* **22** (8), 085703 (2011).
83. A.U. Nilekar, J. Greeley, M. Mavrikakis, *Angew. Chem. Int. Ed. Engl.* **45** (42), 7046 (2006).
84. N. Schichtel, C. Korte, D. Hesse, J. Janeka, *Phys. Chem. Chem. Phys.* **11**, 3043 (2009).
85. Y. Xu, A.V. Ruban, M. Mavrikakis, *J. Am. Chem. Soc.* **126** (14), 4717 (2004).
86. M.M. Kuklja, E.A. Kotomin, R. Merkle, Y.A. Mastrikov, J. Maier, *Phys. Chem. Chem. Phys.* **15** (15), 5443 (2013).
87. U. Diebold, *Surf. Sci. Rep.* **48** (5–8), 53 (2003).
88. A. Kushima, S. Yip, B. Yildiz, *Phys. Rev. B* **82** (11), 115435 (2010).
89. Z. Cai, Y. Kuru, J.W. Han, Y. Chen, B. Yildiz, *J. Am. Chem. Soc.* **133** (44), 17696 (2011).
90. H. Jalili, J.W. Han, Y. Kuru, Z.H. Cai, B. Yildiz, *J. Phys. Chem. Lett.* **2** (7), 801 (2011).
91. M. Kubicek, Z.H. Cai, W. Ma, B. Yildiz, H. Hutter, J. Fleig, *ACS Nano* **7** (4), 3276 (2013).
92. W.T. Hong, M. Gadre, Y.L. Lee, M.D. Biegalski, H.M. Christen, D. Morgan, Y. Shao-Horn, *J. Phys. Chem. Lett.* **4** (15), 2493 (2013).
93. M. Pavone, A.M. Ritzmann, E.A. Carter, *Energy Environ. Sci.* **4** (12), 4933 (2011).
94. M. Mogensen, D. Lybye, N. Bonanos, P.V. Hendriksen, F.W. Poulsen, *Elec. Soc. S2001* (28), 15 (2002).
95. A.T. Motta, *Jom-Us* **63** (8), 63 (2011).
96. G.S. Was, D. Farkas, I.M. Robertson, *Curr. Opin. Solid. St. M.* **16** (3), 134 (2012).
97. T.X.T. Sayle, M. Cantoni, U.M. Bhatta, S.C. Parker, S.R. Hall, G. Mobus, M. Molinari, D. Reid, S. Seal, D.C. Sayle, *Chem. Mater.* **24** (10), 1811 (2012).
98. S.I. Cha, K.H. Hwang, Y.H. Kim, M.J. Yun, S.H. Seo, Y.J. Shin, J.H. Moon, D.Y. Lee, *Nanoscale* **5** (2), 753 (2013).
99. T. Zhu, J. Li, A. Samanta, A. Leach, K. Gall, *Phys. Rev. Lett.* **100** (2), 025502 (2008).
100. D. Rodney, L. Proville, *Phys. Rev. B* **79** (9), 094108 (2009).
101. Y. Fan, Y.N. Osetsky, S. Yip, B. Yildiz, *Phys. Rev. Lett.* **109** (13), 135503 (2012).
102. Y. Fan, Y. Osetsky, S. Yip, B. Yildiz, *Proc. Natl. Acad. Sci. U.S.A.* 2013, in print.
103. K. Dorr, O. Bilani-Zeneli, A. Herklotz, A.D. Rata, K. Boldyreva, J.W. Kim, M.C. Dekker, K. Nenkov, L. Schultz, M. Reibold, *Eur. Phys. J. B* **71** (3), 361 (2009). □

register online at WWW.SVC.ORG **SVC™ TECHCON 2014**

SOCIETY OF VACUUM COATERS
57TH ANNUAL TECHNICAL CONFERENCE

CHICAGO . MAY 3-8, 2014 HYATT REGENCY CHICAGO, ILLINOIS, USA

The **SVC TECHCON** provides the latest advances in vacuum coating and surface engineering technologies, from process and materials development to engineering solutions and industrial applications.

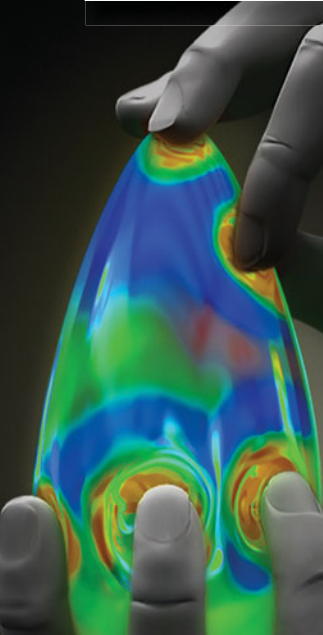
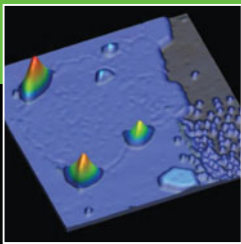
MAY 5–8 TECHNICAL PROGRAM Featuring a Symposium on
ADVANCED COATINGS FOR TRANSPORTATION

MAY 3–8 EDUCATION PROGRAM Problem-Solving Tutorial Courses

MAY 6–7 EQUIPMENT EXHIBIT Dedicated to Vacuum Coating Technologies

MAY 5–8 INTERACTIVE NETWORKING Forums and Discussion Groups

for more information: SVCINFO@SVC.ORG . 505-856-7188 . WWW.SVC.ORG



Elastically strained nanowires and atomic sheets

Dapeng Yu, Ji Feng, and James Hone

Deformation is one of the most fundamental aspects of materials. While mechanical failure is an outcome of deformation to be avoided, elastic deformation can have a pronounced and positive impact on materials properties. The effect of elastic deformation becomes even more evident at low dimensions, because at the micro/nanoscale, materials and structures can usually sustain exceptionally high elastic strains before failure. The purpose of this overview is to present a summary of recent progress on elastically strained nanowires and atomic sheets. First, we will demonstrate that nanowires can sustain large elastic strains, and their bending modulus increases exponentially as the nanowire diameter decreases. Second, the elastic strain has been found to significantly modify the electronic structure of semiconductor nano/microwires to induce a metal–insulator transition at room temperature and to efficiently transform the mechanical energy into electricity. These recent developments point to potential future applications based on the elastic strain engineering of nanoscale materials.

Introduction

Strain is a universal phenomenon pertinent to the synthesis, fabrication, and applications of all types of materials. Strain can have two distinct regimes: In the plastic regime, materials generally undergo irreversible changes, such as failure or property degradation. Elastic deformation, on the other hand, can induce reversible changes to materials properties, from electronic and chemical to optical; this is called elastic strain engineering (ESE). A particularly successful application of strain engineering is pushing the limit of miniaturization of silicon-based field-effect transistors.¹ By alternating deposition of Si and Ge layers, the interlayer lattice mismatch creates controllable strain in the silicon crystal. The precisely controlled strain breaks the crystal field symmetry and reduces the scattering of carriers by phonons, resulting in substantially increased carrier mobility, which allows for further reduction in the channel size.

“Magnified” strain effects in nanowires

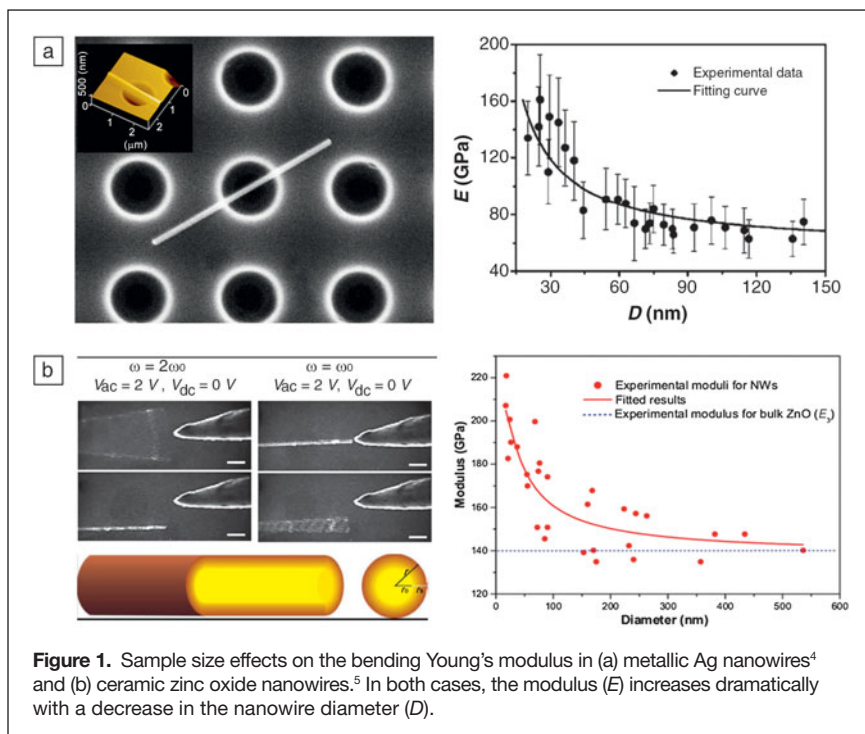
The strength of a material depends very strongly on its dimensions. Typically, smaller structures can tolerate larger deformations before yielding. For a given rod structure under a bending deformation, the smaller the radius of the rod (distance to the rod axis), the larger the strain it can sustain at the

maximum elastic loading stress.² Therefore, it is anticipated that ESE can be profitably explored in materials with reduced dimensions, such as nanowires and atomic sheets.

Rapid progress in device miniaturization has led to the quick rise of flexible, nanoscale devices for which one-dimensional nanowires and atomic sheets such as graphene are particularly promising candidate materials. These materials possess unusual electronic properties, frequently arising from giant surface effects and strong quantum confinement. Thanks to their reduced dimensions, these materials also exhibit superb mechanical properties, some of which (e.g., graphene) are among the strongest human-made materials. Moreover, unlike in strain-engineering in the conventional microelectronics industry, where uniform strain is often employed to enhance materials properties, in these low-dimensional wires and sheets, inhomogeneous strain fields can also be generated, providing unprecedented opportunities to explore paradigms of ESE. Therefore, nanowires and atomic sheets are ideal platforms to explore novel elastic strain effects and device concepts at the nanoscale.

Wong et al. were among the first to address the size effects of mechanical properties of nanotubes and SiC nanorods using atomic force microscopy (AFM).³ They found that the strengths of SiC nanorods were substantially greater

Dapeng Yu, School of Physics, Peking University; yudp@pku.edu.cn
Ji Feng, School of Physics, Peking University; jfeng11@pku.edu.cn
James Hone, Department of Electronic Engineering, Columbia University; jh2228@columbia.edu
DOI: 10.1557/mrs.2014.6

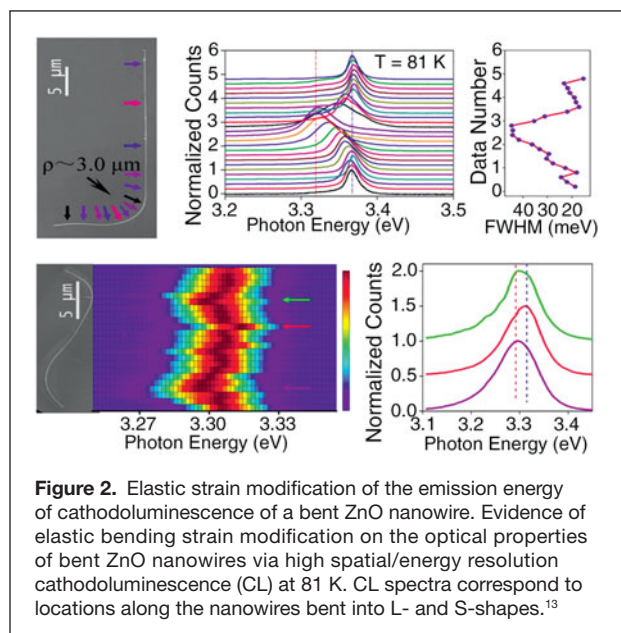


than those found previously for SiC bulk structures. The size effect of nanowires is also reflected in the variation of the Young's modulus upon bending as a function of the nanowire diameter. Yu's group⁴ systematically investigated metallic silver nanowires by precisely placing individual Ag nanowires of different diameters over microhole arrays via focused ion beam milling. A calibrated AFM tip was used to push down on the middle point of each suspended Ag nanowire. From measurement of the force applied with each push and the corresponding displacement, the bending Young's modulus could be easily deduced, as shown in **Figure 1**. It is somewhat surprising to observe that the bending Young's modulus increases from the bulk value of ~ 76 GPa to as high as ~ 160 GPa as the diameter of the nanowire decreases to ~ 20 nm. Similar observations were found for other brittle ceramic materials. For example, Zhu and co-workers⁵ studied ZnO nanowires by applying an alternating electric field at the tip of a single ZnO nanowire, causing it to undergo bending vibrations (Figure 1b). The bending Young's modulus increased exponentially with decreasing ZnO nanowire diameter, from the bulk value of ~ 140 GPa to ~ 200 GPa at a diameter of 20 nm. A core-shell model was proposed to explain the abnormal increase.

Han and Zhang carried out a systematic investigation of the mechanical properties of a series of semiconducting nanowires (Si, SiC, and glassy silicon oxide, which are all brittle in bulk form).⁶⁻⁹ The size-dependence of the energy bandgap of ZnO nanowires under elastic tensile strain is particularly interesting, observed via *in situ* cathodoluminescence measurements in a scanning electron microscope (SEM). They found that the maximal strain and the corresponding bandgap modification increased with decreasing nanowire diameter.¹⁰ For example,

the bandgap energy decreased (was red-shifted) by about 110 meV for a smaller nanowire ~ 100 nm in diameter under a large elastic tensile strain up to $\sim 7.3\%$, which is nearly double the value of ~ 59 meV for a larger nanowire of 760 nm in diameter under a tensile strain of 1.7%. A two-step linear feature involving bandgap reduction caused by strain and a corresponding critical strain was observed in ZnO nanowires with diameters < 300 nm. The same group also observed unusually large elastic strains in copper nanowires approaching the theoretic elastic limit of bulk copper.¹¹

Such large elastic strains can be used to tune other properties of nanowires, as there is a strong mechano-electrical coupling. For example, the conductance of ZnO nanowires and CdSe nanobelts (ribbon-like structures) increases very sensitively with the increase in bending strain under AFM tip manipulation.¹² Yu's group conducted a systematic investigation of strain modulation on the optical emission energy and electronic fine structures of ZnO nano/microwires under elastic bending deformation.¹³⁻¹⁶ To confirm that the bending deformation is in the elastic regime, a single ZnO nanowire was pushed and bent on a silicon substrate, before applying a drop of liquid to release the bent nanowire from the substrate and return it to its original straight form. The bending strain modifies the near-edge emission energy of ZnO nanowires, as revealed by cathodoluminescence (CL) spectroscopy at liquid nitrogen temperature (~ 81 K). **Figure 2** presents a collection of CL spectra along the axial positions of a single ZnO nanowire bent into an "L" shape. These were obtained from 13 axial



positions corresponding to different radii of bending curvature (and different bending strains).¹³ Clearly, the energy of the near-edge emission is altered by the changing bending strain, resulting in an overall red-shift with increasing strain. A ZnO nanowire bent into an “S” shape displays similar red-shifting at the two bent positions (maximum strains).¹³ Obvious peak broadening is also observed.

Considering the electron beam scattering volume at the working accelerating voltage and the exciton diffusion length, wires of larger diameters would allow better resolution of the strain modification route for the optical properties of ZnO. As shown in **Figure 3**, a hexagonal-shaped ZnO microwire, with a diameter $\sim 3 \mu\text{m}$ and length of several hundreds of μm , was used for systematic analysis.¹⁴ Nine positions marked with “I” to “IX” were selected for a CL line scan analysis along the radial direction. Because at each position the wire has a different bending radius of curvature, it undergoes different elastic bending strains. Across the cross-section at each line scan position, there exists a linear strain ranging from tensile to compressive. Clearly, the two free ends marked “I” and “IX” are strain-free. To present the change rate of the local strain along the axial direction, a novel parameter called the strain gradient β is proposed, which is defined as the inverse of the radius ρ of the bending curvature: $\beta = 1/\rho$. With a scan step $\sim 100 \text{ nm}$, more than 30 CL spectra were collected along the cross-section at each line-scan position. The complete sets of the CL spectra collected at the nine positions are presented in Figure 3, and the corresponding strain gradients are marked as well. The two dominant exciton peaks shift linearly with the strain gradient.¹⁴

CL spectroscopy in the SEM not only guarantees very high spatial resolution compared to laser excitation but also has high energy resolution at low temperature, allowing for the collection of very clean spectra that make the subsequent analysis much more straightforward. Therefore, a systematic CL spectroscopy analysis was conducted at liquid helium temperature ($\sim 5.4 \text{ K}$), as shown in Figure 3.¹⁵ A representative series of CL spectra are presented that were obtained from a line scan along the cross-sectional direction of another bent ZnO microwire. Surprisingly, modification of the bending strain is asymmetric, that is, at the tensile side, a mono red-shift with an increase in the tensile strain can be seen. However, on the compressive side, blue-shifting, broadening, and peak splitting occur with increasing

compressive strain. Such a strain gradient effect is unique and representative for nanowire structures under non-uniform bending deformation, as the strain gradient causes a built-in field that can manipulate the transport of the carriers, leading to possible new concept devices.

Elastic strain also has significant effects on other functional properties of the nanowires.^{16–20} Yang et al. investigated

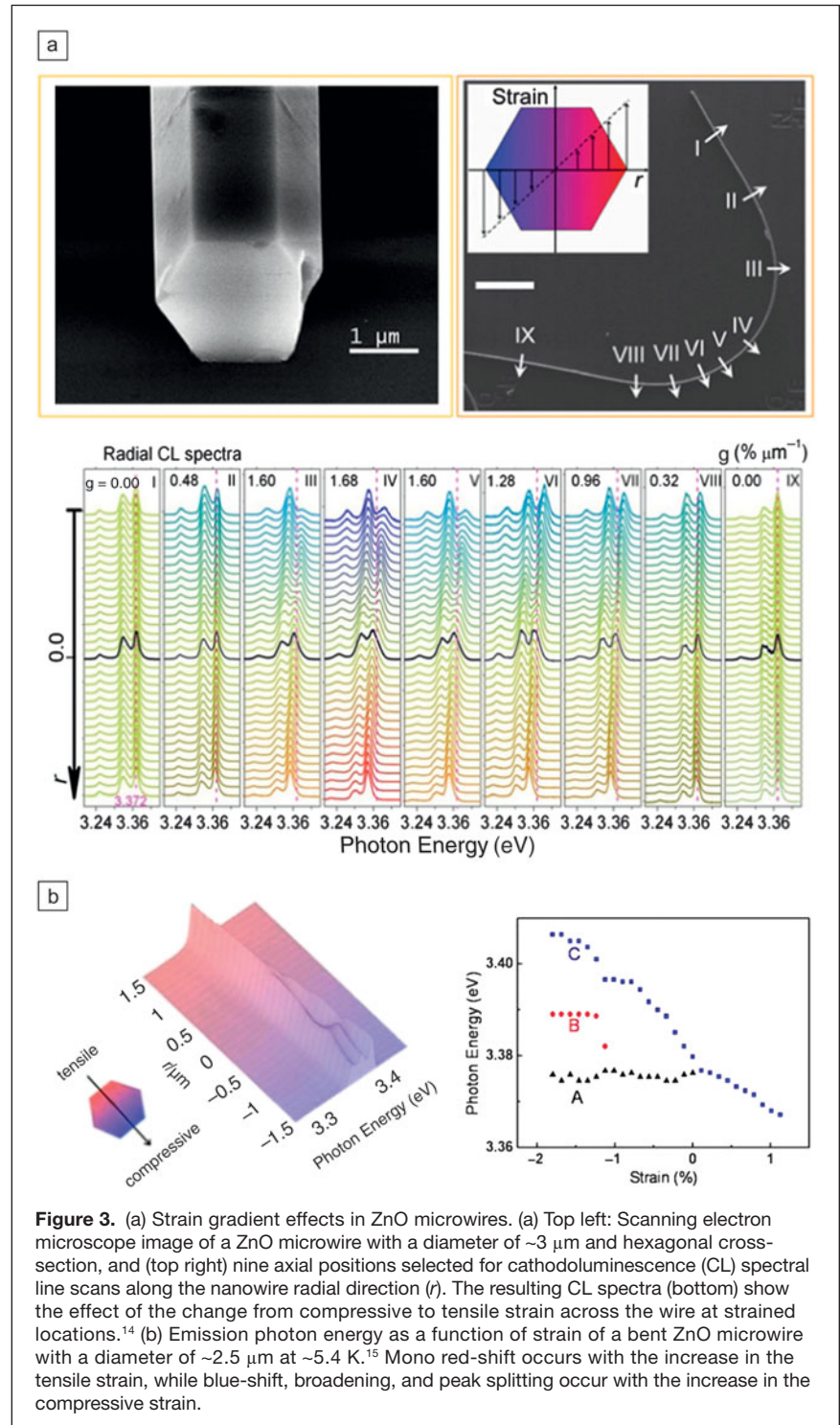


Figure 3. (a) Strain gradient effects in ZnO microwires. (a) Top left: Scanning electron microscope image of a ZnO microwire with a diameter of $\sim 3 \mu\text{m}$ and hexagonal cross-section, and (top right) nine axial positions selected for cathodoluminescence (CL) spectral line scans along the nanowire radial direction (r). The resulting CL spectra (bottom) show the effect of the change from compressive to tensile strain across the wire at strained locations.¹⁴ (b) Emission photon energy as a function of strain of a bent ZnO microwire with a diameter of $\sim 2.5 \mu\text{m}$ at $\sim 5.4 \text{ K}$.¹⁵ Mono red-shift occurs with the increase in the tensile strain, while blue-shift, broadening, and peak splitting occur with the increase in the compressive strain.

the piezoresistance of a single *p*-silicon nanowire under uniaxial tensile/compressive strain and observed a so-called giant piezoresistance phenomenon.¹⁶ Liu et al. theoretically constructed an elastically strained silicon nanoribbon, which consists of a normal and a strained unit cell, called a single-element electronic heterojunction superlattice.¹⁸ In such a strained configuration, it is predicted that, due to the strain effect and quantum confinement, it is possible to manipulate the motion of carriers via elastic strain.

Wu et al. demonstrated another excellent example of elastic strain manipulation of nanowire properties.²⁰ Via simple tip manipulation of the bending deformation of a single-crystal vanadium dioxide nanowire, they were able to control the metal–insulator transition at room temperature, which normally happens at an elevated temperature in its bulk counterpart, as shown in **Figure 4**.

Wang's group at the Georgia Institute of Technology has used the elastic bending deformation of ZnO micro/nanowires to create new kinds of nanogenerators^{21–26} and flexible strain sensors.^{27,28} **Figure 5** summarizes the main physical principle as to how elastic bending strain converts mechanical energy into electricity using piezoelectric ZnO nanowires. The initial nanogenerators are based on a tungsten AFM tip bending vertically arrayed ZnO nanowires, and the output arises from the unique coupling of piezoelectric and semiconducting properties. It is found that a metal (tungsten tip)–semiconductor (ZnO nanowires) Schottky barrier plays a crucial role and governs the whole power generating process. Specifically, no output current is collected when the tungsten tip first touches the nanowire and pushes the nanowire, and power output occurs only when the tip touches the compressive side of the bent nanowire. So far, flexible high-output nanogenerators based on ZnO nanowire arrays have already been demonstrated that can charge light-emitting diodes²⁵ and could potentially be used in wireless microelectronic devices.²⁷ The excellent mechanical and strain-enhanced physical properties have made semiconductor nanowires competitive and promising candidates for use in flexible solar cells²⁹ and supercapacitors.³⁰

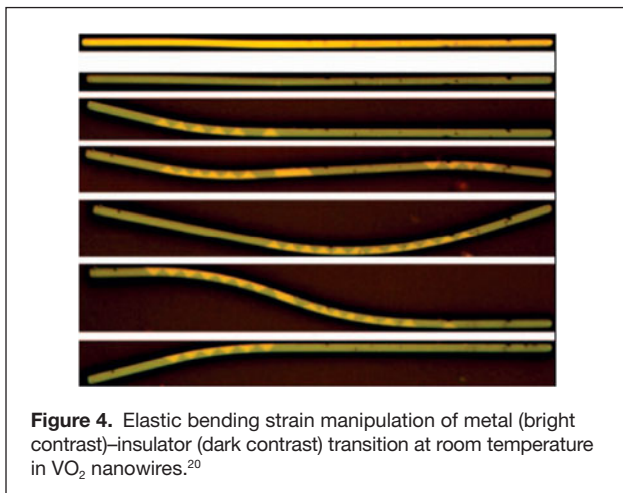


Figure 4. Elastic bending strain manipulation of metal (bright contrast)–insulator (dark contrast) transition at room temperature in VO₂ nanowires.²⁰

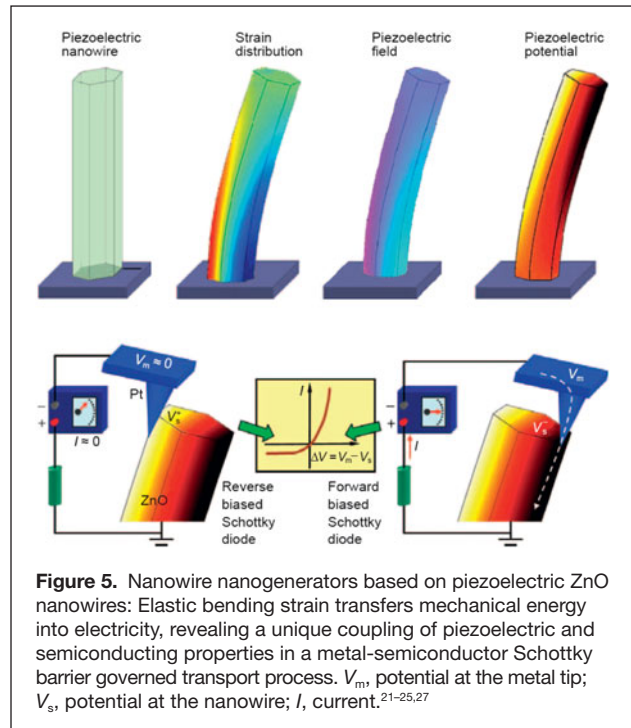
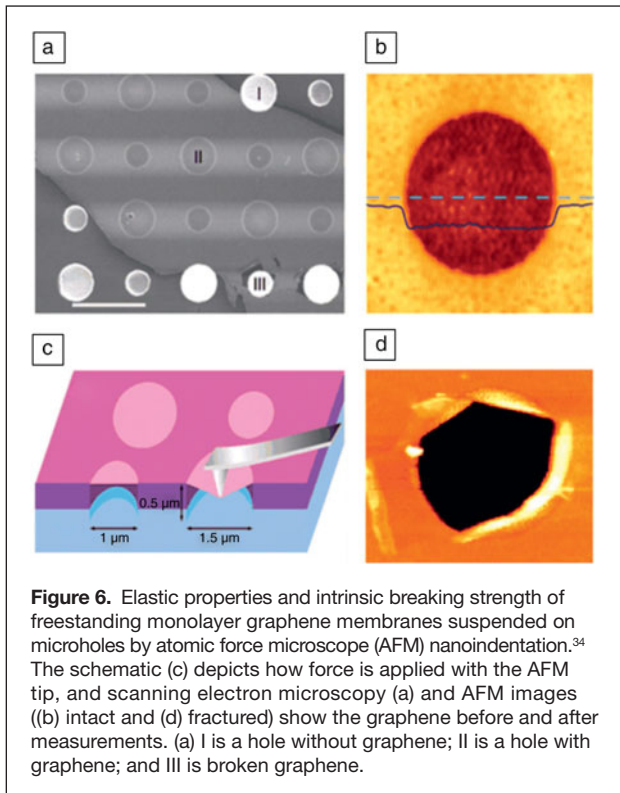


Figure 5. Nanowire nanogenerators based on piezoelectric ZnO nanowires: Elastic bending strain transfers mechanical energy into electricity, revealing a unique coupling of piezoelectric and semiconducting properties in a metal–semiconductor Schottky barrier governed transport process. V_m , potential at the metal tip; V_s , potential at the nanowire; I , current.^{21–25,27}

Graphene, the strongest material

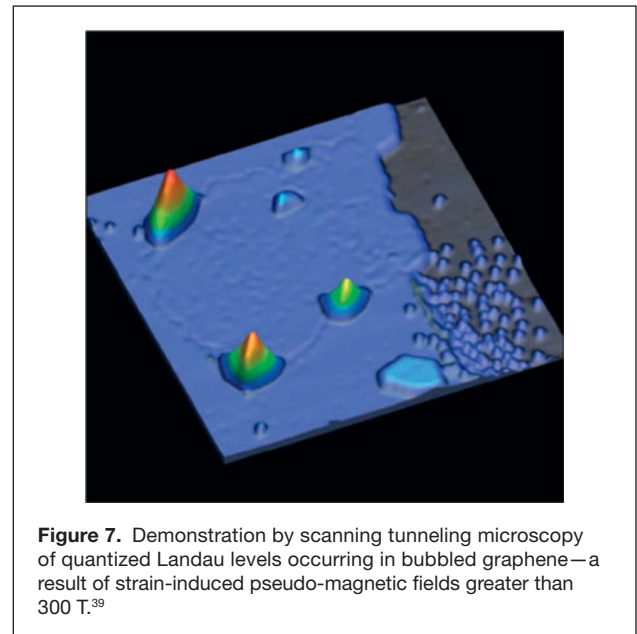
Graphene is a two-dimensional atomic carbon sheet that displays remarkable and distinctive electronic and mechanical properties^{31–33} (see the December 2012 issue of *MRS Bulletin*). Its unique electronic properties, which arise from a linear Dirac-like band dispersion near the Fermi level, have led to novel physics and have stimulated intensive investigations into high mobility all-carbon electronics. Because graphene consists of a two-dimensional sheet of covalently bonded carbon atoms, its intrinsic tensile strength is predicted to exceed that of any other material. This enormous strength is the motivation for the current use of carbon-fiber reinforcements, whose strength still falls well short of the intrinsic value of the fibers, in advanced composites. Replacement or supplementation with graphene may permit even higher performance composite materials.

Lee et al. experimentally verified the ultrahigh strength of graphene.³⁴ As shown in **Figure 6**, the elastic properties and intrinsic breaking strength of freestanding monolayer graphene membranes were studied by nano-indentation using AFM. Analysis of the shape of the force–displacement curves yields a Young's modulus of ~ 1 TPa, equivalent to the basal-plane stiffness of graphite—as expected due to the weak interlayer interaction. To deduce the breaking strength from the measured breaking force, finite element analysis simulated the experiment, employing a nonlinear constitutive model of the stress–strain behavior. The simplest such model yields an intrinsic strength of 130 GPa. Subsequent analysis employing a more detailed nonlinear anisotropic model yielded a more accurate value of 100 GPa from the same data.³⁵ This ultrahigh strength demonstrates that graphene is the strongest material



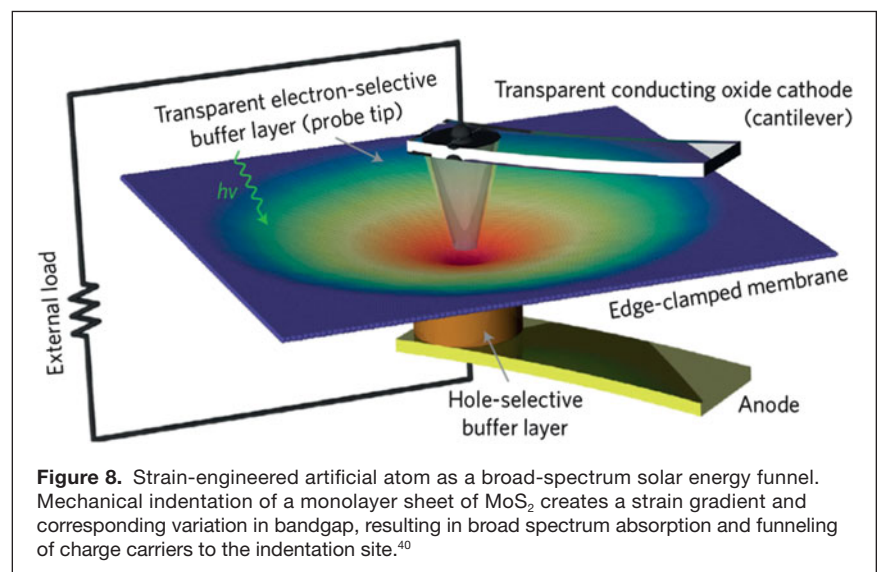
ever measured, and shows that atomically perfect nanoscale materials can be mechanically tested to deformations well beyond the linear regime. In more recent work, Lee et al. have demonstrated that this ultrahigh strength is maintained even in the presence of grain boundaries, opening up the possibility of large-area applications.³⁶

The ultrahigh mechanical strength makes it possible to impart very large elastic strains, which can significantly engineer the electronic states of graphene.^{37–39} In particular, strain causes shifts in the location of the Dirac points in the electronic band structure in the same way as an applied magnetic field. A particularly dramatic example of this effect was demonstrated by Levy and co-workers on highly strained nanobubbles in graphene grown on a Pt(111) substrate, as shown in **Figure 7**. Via detailed measurements and simulation of the scanning tunneling spectra, they found that the bending strain of the bubbled graphene caused enormous pseudo-magnetic fields greater than 300 Tesla, resulting in quantized Landau levels.³⁹ These results^{34,39} suggest that strain engineering at nanoscale energy levels can be a viable means to control the electronic structure of graphene even at room temperature. The experimental demonstration of the enormous pseudo-magnetic fields also provides a new basis to study the charge carriers in previously inaccessible extremely high magnetic field



regimes in condensed matter and to achieve deliberate mechanical control over electronic structure in graphene.

Feng et al.^{40,41} presented a recent example demonstrating strain engineering of an atomic sheet. They considered the possibility of tuning the optical absorption and charge carrier dynamics in an atomically thin semiconducting membrane. The central idea proposed is to utilize the spatial variation of the bandgap induced by the elastic strain field to direct the flow of charge carriers and create a spatial concentration of excitons or charge carriers. Using this idea, a photovoltaic device that is made from a strain-engineered MoS₂ monolayer was proposed. As shown in **Figure 8**, the atomic sheet is subject to a central load configuration under a mechanical indenter, whereupon an inhomogeneous strain field is focused toward the center of the membrane. The strain field thus



produced then modulates the exciton spectrum of the semiconductor to create an effective built-in field, concentrating the charge carriers toward the center of the funnel-shaped device. Feng et al. proposed that a strain-engineered funnel device will capture and concentrate a broad range of the solar spectrum as schematically shown in Figure 8. Very recently, using photoluminescence imaging, a strain-induced reduction of the direct bandgap and funneling of photo-generated excitons toward regions of higher strain was experimentally observed in MoS₂ monolayers.⁴² In another experiment, Nam et al. induced a strain gradient along Ge nanowires to induce charge carrier concentration similar to conventional semiconductor heterostructure. This effect was probed by spatially resolved photoluminescence measurements.⁴³

Summary and outlook

Semiconductor nanowires and graphene are representative 1D and 2D nanostructures, respectively, which can tolerate much higher elastic deformation compared to their bulk counterparts. Just as classical chemical doping allows for the fabrication of a wide range of optoelectronic devices, such as photovoltaic cells, semiconductor lasers, light-emitting diodes, and field-effect transistors, elastic strain offers another degree of freedom to continuously and reversibly tune the lattice parameter in nanowires and atomic sheets, and to modulate the electronic states and even carrier dynamics. We would like to point out that although there has been exciting progress already made in the elastic strain engineering of nanowires and atomic sheets, many challenges remain in this field. Innovative ideas, novel means of characterization, and more powerful and effective methods of theoretical calculations and simulations are needed before the dream of new concept strain-modulated nanodevices is realized and changes our daily lives.

Acknowledgments

This work is supported by NSFC (11174009) and the National 973 Programs of China (2013CB921900, 2012CB619402).

References

1. M. Jeong, B. Doris, J. Kedzierski, K. Rim, M. Yang, *Science* **306**, 2057 (2004).
2. P. Hiralal, H.E. Unalan, G.A.J. Amaratunga, *Nanotechnology* **23**, 194002 (2012).
3. E.W. Wong, P.E. Sheehan, C.M. Lieber, *Science* **277**, 1971 (1997).
4. G.Y. Jing, H.L. Duan, X.M. Sun, Z.S. Zhang, J. Xu, Y.D. Li, J.X. Wang, D.P. Yu, *Phys. Rev. B* **73**, 235409 (2006).

5. C.Q. Chen, Y. Shi, Y.S. Zhang, J. Zhu, Y.J. Yan, *Phys. Rev. Lett.* **96**, 075505 (2006).
6. X.D. Han, Y.F. Zhang, K. Zheng, X.N. Zhang, Z. Zhang, Y.J. Hao, X.Y. Guo, J. Yuan, Z.L. Wang, *Nano Lett.* **7**, 452 (2007).
7. X. Han, S. Zheng, Y. Zhang, K. Zheng, X. Liu, G. Chen, Y. Hao, X. Guo, *Nano Lett.* **8**, 2258 (2008).
8. K. Zheng, X. Han, L. Wang, Y. Yue, Y. Zhang, Y. Qin, X. Zhang, Z. Zhang, *Nano Lett.* **9**, 2471 (2009).
9. K. Zheng, C. Wang, Y.-Q. Cheng, Y. Yue, X. Han, Z. Zhang, Z. Shan, S.X. Mao, M. Ye, Y. Yin, E. Ma, *Nat. Commun.* **1**, 24 (2010).
10. B. Wei, K. Zheng, Y. Ji, Y. Zhang, Z. Zhang, X. Han, *Nano Lett.* **12**, 4595 (2012).
11. Y. Yue, P. Liu, Z. Zhang, X. Han, E. Ma, *Nano Lett.* **11**, 3151 (2011).
12. X.B. Han, G.Y. Jing, X.Z. Zhang, R. Ma, X. Song, J. Xu, Z. Liao, N. Wang, D. Yu, *Nano Res.* **2**, 553 (2009).
13. X.B. Han, L.Z. Kou, X.L. Lang, J.B. Xia, N. Wang, R. Qin, J. Lu, J. Xu, Z.M. Liao, X.Z. Zhang, X.D. Shan, X.F. Song, J.Y. Gao, W.L. Guo, D.P. Yu, *Adv. Mater.* **21**, 4937 (2009).
14. X. Han, L. Kou, Z. Zhang, Z. Zhang, X. Zhu, J. Xu, Z. Liao, W. Guo, D. Yu, *Adv. Mater.* **24**, 4707 (2012).
15. Z.M. Liao, H.C. Wu, Q. Fu, X. Fu, X. Zhu, J. Xu, I.V. Shvets, Z. Zhang, W. Guo, Y. Leprince-Wang, Q. Zhao, X. Wu, D.P. Yu, *Sci. Rep.* **2**, 452 (2012).
16. R.H. He, P.D. Yang, *Nat. Nanotechnol.* **1**, 42 (2006).
17. J.S. Milne, A.C.H. Rowe, S. Arscott, *Phys. Rev. Lett.* **105**, 226802 (2010).
18. Z. Liu, J. Wu, W.H. Duan, M.G. Lagally, F. Liu, *Phys. Rev. Lett.* **105**, 016802 (2010).
19. A.M. Smith, A.M. Mohs, S. Nie, *Nat. Nanotechnol.* **4**, 56 (2008).
20. J. Cao, E. Ertekin, V. Srinivasan, W. Fan, S. Huang, H. Zheng, J.W.L. Yim, D.R. Khanal, D.F. Ogletree, J. Wu, *Nat. Nanotechnol.* **13**, 132 (2009).
21. Z.L. Wang, J.H. Song, *Science* **312**, 242 (2006).
22. Z.L. Wang, *Nano Res.* **1**, 1 (2008).
23. X.D. Wang, J.H. Song, J. Liu, Z.L. Wang, *Science* **316**, 102 (2007).
24. Y. Qin, X. Wang, Z.L. Wang, *Nature* **451**, 908 (2008).
25. G. Zhu, R.S. Yang, S.H. Wang, Z.L. Wang, *Nano Lett.* **10**, 3151 (2010).
26. S. Xu, B.J. Hansen, Z.L. Wang, *Nat. Commun.* **1**, 93 (2010).
27. J. Zhou, Y.D. Gu, P. Fei, W.J. Mai, Y.F. Gao, R.S. Yang, G. Bao, Z.L. Wang, *Nano Lett.* **8**, 3035 (2008).
28. Q. Yang, W.H. Wang, S. Xu, Z.L. Wang, *Nano Lett.* **11**, 4012 (2011).
29. W. Wang, Q. Zhao, H. Li, H. Wu, D. Zou, D. Yu, *Adv. Funct. Mater.* **22**, 2775 (2012).
30. H. Li, Q. Zhao, W. Wang, H. Dong, D.S. Xu, G.J. Zou, H.L. Duan, D.P. Yu, *Nano Lett.* **13**, 1271 (2013).
31. K.S. Novoselov, A.K. Geim, S.V. Morozov, D. Jiang, Y. Zhang, S.V. Dubonos, I.V. Grigorieva, A.A. Firsov, *Science* **306**, 666 (2004).
32. K.S. Novoselov, A.K. Geim, S.V. Morozov, D. Jiang, M.I. Katsnelson, I.V. Grigorieva, S.V. Dubonos, A.A. Firsov, *Nature* **438**, 197 (2005).
33. Y.B. Zhang, Y.W. Tan, H.L. Stormer, P. Kim, *Nature* **438**, 201 (2005).
34. C. Lee, X. Wei, J.W. Kysar, J. Hone, *Science* **321**, 385 (2008).
35. X. Wei, B. Fragneaud, C.A. Marianetti, J.W. Kysar, *Phys. Rev. B* **80**, 205407 (2009).
36. G.-H. Lee, R.C. Cooper, S.J. An, S. Lee, A. van der Zande, N. Petrone, A.G. Hammerberg, C. Lee, B. Crawford, W. Oliver, J.W. Kysar, J. Hone, *Science* **340**, 1073 (2013).
37. V. Pereira, A. Castro Neto, *Phys. Rev. Lett.* **103**, 046801 (2009).
38. M. Huang, H. Yan, T.F. Heinz, J. Hone, *Nano Lett.* **10**, 4074 (2010).
39. N. Levy, S.A. Burke, K.L. Meaker, M. Panlasigui, A. Zettl, F. Guinea, A.H. Castro Neto, M.F. Crommie, *Science* **329**, 544 (2010).
40. J. Feng, X. Qian, C.W. Huang, J. Li, *Nat. Photonics* **6**, 866 (2012).
41. A. Van der Zande, J. Hone, *Nat. Photonics* **6**, 804 (2012).
42. A. Castellanos-Gomez, R. Roldán, E. Cappelluti, M. Buscema, F. Guinea, H.S. J. van der Zant, G.A. Steele, *Nano Lett.* **13** (11), 5361 (2013).
43. D. Nam, D.S. Sukhdeo, J.-H. Kang, J. Petykiewicz, J.H. Lee, W. Shik Jung, J. Vučković, M.L. Brongersma, K.C. Saraswat, *Nano Lett.* **13** (7), 3118 (2013). □

MRS MEMBERSHIP
JOIN OR RENEW FOR 2014!
www.mrs.org/join

MRS MATERIALS RESEARCH SOCIETY
 Advancing materials. Improving the quality of life.